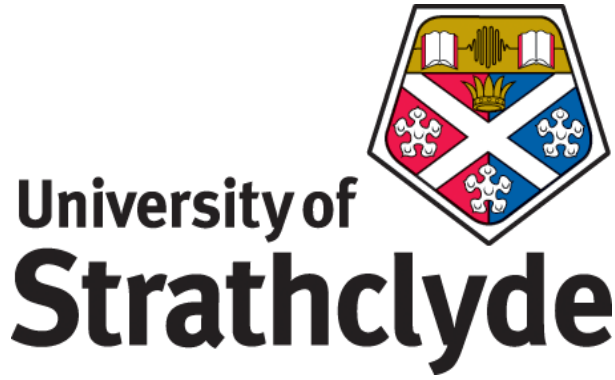

A Study of Stimulated Brillouin Scattering in Laser Produced Plasmas

Kathryn Ann Wilson M.Sci. (Hons)

SUPA Department of Physics

The University of Strathclyde

Thesis Submitted for the Degree of Ph.D.
September 2013

This thesis is the result of the author's original research. It has been composed by the author and has not been previously submitted for examination which has led to the award of a degree.

Abstract

The production of high power, short duration laser pulses is of interest to a wide variety of applications ranging from high-energy-density physics to laser-driven nuclear fusion. The exploitation of laser-plasma instabilities, in particular stimulated Brillouin scattering (SBS), for the creation of such pulses is found to have great potential.

Analysis from numerical, analytical and experimental studies are presented within this thesis which were constructed to develop a platform of knowledge to enable the understanding and development of stimulated Brillouin scattering as a possible means of laser amplification to ultra-high intensities. From these studies a number of scaling laws were developed governing the optimal parameter space for the laser pump beam, probe beam and the plasma amplifier in addition to the ability to control the final amplified pulse characteristics.

Optimum regions of parameter space occurring at a density of $0.3n_c$ with pump and seed laser intensities of $1x10^{16}Wcm^{-2}$ and $1x10^{15}Wcm^{-2}$, respectively, were found to produce efficient laser amplification of 57%. The scalability to wider regions of parameter space was also confirmed for laser intensities down to $1x10^{13}Wcm^{-2}$. The presence of Brillouin scattering was noted for all underdense plasmas studied with Brillouin amplification being effective for densities greater than the quarter critical density level due to mode competition with Raman scattering. Collisional processes were also investigated and it was found that the introduction of collisions results in an increase in the efficiency of laser amplification via stimulated Brillouin scattering by 10% and a significant increase in the contrast of the resultant seed laser beam. Corroboration between the numerical, analytical and experimental studies undertaken indicates a high level of reliability in the results presented throughout this thesis.

Acknowledgements

Completion of this thesis marks the close of an important chapter in my life and it would not have been possible without the assistance of a number of individuals who were instrumental to the success of this research project.

First and foremost I would like to thank my primary PhD supervisor Professor Robert Bingham for his support and the numerous opportunities he provided me with over the course of my research career. His guidance and passion for his research field willed me to be the best scientist I could be.

A special thank you goes to Raoul Trines of the Rutherford Appleton Laboratory for his secondary supervision and support, for which I am forever indebted. His expertise, friendly ear and "death by white board" teachings I will never forget.

I would also like to thank Frederico Fiuza of the Lawrence Livermore National Laboratory for his endless patience when teaching me how to use OSIRIS and for his invaluable technical support over the course of my studies.

Finally, I would like to thank all the staff and students in the Atoms, Beams and Plasmas group at the University of Strathclyde for their support throughout the duration of my studies. In particular I wish to thank Kathleen, Martin and Ross, with whom I shared an office with over the years, for their laughter, encouragement and assistance throughout my PhD.

Contents

Chapter 3: Numerical Techniques: OSIRIS Particle-in-Cell Code

Chapter 4: Damping effects on amplification of laser beams by SBS

Chapter 5: Optimisation of SBS in parameter space

Chapter 6: SBS with a single laser frequency

Chapter 7: Conclusions and future work

Nomenclature

A	wave amplitude
a_0	dimensionless, scaled, wave amplitude
B	magnetic field
γ	relativistic factor (Lorentz-Fitzgerald factor)
c	speed of light, $3x10^8 ms^{-1}$
c_s	ion acoustic speed
$\underline{D}$	electric flux density
δn	density perturbation
$\underline{E}$	electric field
e	electronic charge
ϵ	cold plasma dielectric tensor
ε_0	permittivity of free space, $8.854x10^{-12}$ F/m
E_0	laser field strength
E_1	field strength of electromagnetic daughter wave
$\underline{F}$	Lorentz force
F_p	Ponderomotive force
f_{cs}	collisional frequency
g	plasma parameter
$\underline{H}$	magnetic field strength
θ	pitch angle
θ_{res}	resonant angle

I	current
I_0	peak intensity of laser beam
$\underline{J}$	total current density
k	wavenumber
k_B	Boltzman constant, $1.38 \times 10^{-23} JK^{-1}$
λ	wavelength
λ_D	Debye length
λ_{mfp}	mean free path
μ_0	permeability of free space
m_e	electronic mass
m_i	ion mass
n_c	critical density of plasma
n_e	electron number density
n_i	ion number density
n_n	number density of stationary targets
ρ	total charge density, momentum
σ	conductivity tensor
σ_{sc}	total scattering cross section
r	radius
t	time
τ	laser pulse length
τ_c	collisional time
T_e	electron temperature
T_i	ion temperature

$\langle U_s \rangle$	mean speed of mobile species
$\langle u \rangle$	mean speed of colliding particles
V_e	electron thermal speed
v	velocity
v_A	Alfven speed
v_g	group velocity
v_{os}	electron quiver velocity
v_{ph}	phase velocity
v_{th}	thermal velocity
ν	linear damping rate
ω	angular frequency
ω_i	Landau damping decrement
ω_{pe}	angular frequency of plasma electrons
ω_{pi}	angular frequency of plasma ions
Ω_e	electron cyclotron resonance
Ω_i	ion cyclotron resonance
Z	charge state

Chapter 1
Introduction

1.1 Classical laser amplification techniques

Since the development of the laser in 1960 [Maiman 1960] the advancement of high intensity laser systems has become increasingly important as a tool for studying modern physics. Contemporary high power laser systems typically make use of solid state laser technology to reach powers at the petawatt level, however such systems have significant drawbacks. The peak power of the laser pulses attainable through such techniques is severely limited to intensities below the threshold for non-linear effects in order to avoid breakdown of the optical components. Therefore, in order to achieve high intensities, large energies from sizeable amplifiers are required where the size of the components is dictated by the energy desired. This leads to the requirement for very large and very expensive optical components.

A breakthrough in generating intense laser pulses came in 1985 with the application of chirped pulse amplification (CPA) to laser systems [Strickland and Mourou 1985]. This technique, first demonstrated in the 1940's for Radar applications, is based on the fact that a short pulse has a broad colour spectrum. This method involves taking a short, low intensity pulse and passing it through a material with dispersive properties such that the various colours in its spectra are separated in time, leading to an increase in the duration of the pulse. The resultant pulse has a lower peak power, due to the conservation of energy, and therefore detrimental effects in the gain medium are avoided. Once the long pulse has passed through the amplifier a dispersive compressor is used, typically a grating pair, to remove the chirp and

temporally compress the pulse to a duration similar to that of the input pulse but with a significantly increased peak power. CPA-based optical systems have been shown to generate sub-picosecond petawatt laser pulses [Key et al. 1998] [Mourou, Barty and Perry 1998] with up to 500J per pulse. A schematic diagram of the pulse evolution for the CPA process is seen in figure 1.1.1 [Paschotta 2008].

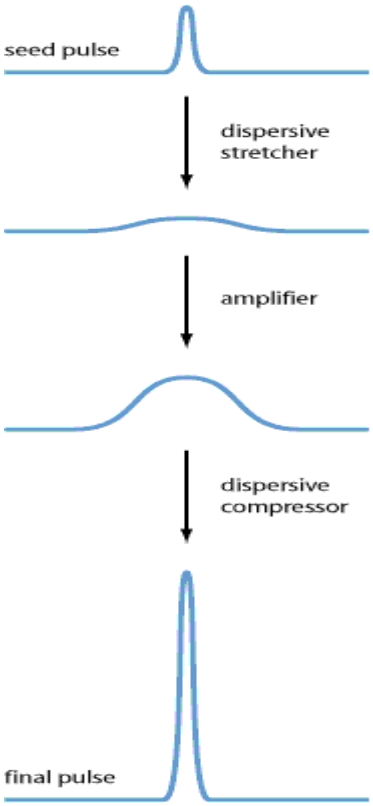

Figure 1.1.1 - Evolution of the temporal pulse shape in a chirped-pulse amplifier

Although damage to the gain medium is avoided in this amplification scheme, the beam diameter on the compressor grating still has to be large. This means for the most powerful devices a beam diameter of the order of 1m is required. In order to utilise CPA to obtain higher intensities the use of laser beams with even larger diameter is required. The use of such solid state amplifiers, such as neodymium glass, and gratings limits the intensity to 10^{12}Wcm^{-2}, therefore innovative solutions

are required to continue the evolution of laser technology at the intensity frontier and further investigate laser interactions with matter.

1.2 Laser amplification in plasma

By opting for plasma as the interaction medium, millimetre-diameter plasmas could potentially replace current large scale equipment required to generate high intensity beams at a reduced cost and complexity for future laser systems.

Laser propagation in plasma is possible if the electron density, n_e, lies below the critical density of a plasma, $n_c = \omega\varepsilon_0 m_e/e^2$, where m_e is the electron rest mass, ω is the carrier frequency of the laser pulse, e is the electronic mass and ε_0 is the permittivity of free space. If the plasma has $n_e > n_c$ then the plasma is said to be overdense and when $n_e < n_c$ the plasma is known as underdense. For a laser wavelength of $1\mu m$ the critical density is $1.1x10^{21}cm^{-3}$. For the research undertaken as part of this thesis a $1\mu m$ laser is used with a typical plasma density of $0.3n_c$.

During laser-matter interactions, various physical regimes of operation are experienced depending on the intensity of the laser light. Differentiation between these regimes can be characterised by the electron quiver velocity, $v_{os} = |eE_0/m_e\omega|$, which is the oscillatory motion of the electron in the laser field, where E_0 is the laser field strength [Kruer 2003]. For low light intensities up to $10^8 Wcm^{-2}$ the electrons oscillate at the laser frequency, $\omega = 2\pi c/\lambda = ck$, where c is the speed of light and ω, λ and k denote the laser angular frequency, wavelength and wavenumber, respectively. For medium light intensities, up to approximately $10^{15} Wcm^{-2}$, the electrons are stripped from the atoms and oscillate in a plane along the laser polarisation direction at a frequency corresponding to the laser frequency. Finally, for ultra-high intensities corresponding to $10^{18} Wcm^{-2}$ or higher the electrons are strongly driven by the laser field and form a relativistic plasma. The electrons in this case oscillate at velocities close to the speed of light resulting in a relativistic mass correction for the particles.

In this thesis all laser intensities considered will be less than $10^{18} Wcm^{-2}$, which is below the onset of relativistic effects, therefore a non-relativistic approach will be adopted throughout.

1.3 Review of plasma based laser amplification

Previous studies of laser amplification in plasma have consisted of the application of stimulated Raman scattering in order to produce high power laser pulses. This technique utilises the Raman parametric instability to achieve ultrahigh laser intensities by the interaction of a long pump-laser beam with a counter-propagating short probe pulse via a longitudinal plasma wave. This results in a large percentage of the energy in the long pulse beam to be transferred to the short beam. Due to the fact that the short pulse has a much shorter duration than the long pulse the resulting intensity of the short beam can be many times that of the original long pulse beam. The processes involved in Raman amplification and the generalised feedback loop of a parametric instability can be seen in figure 1.3.1.

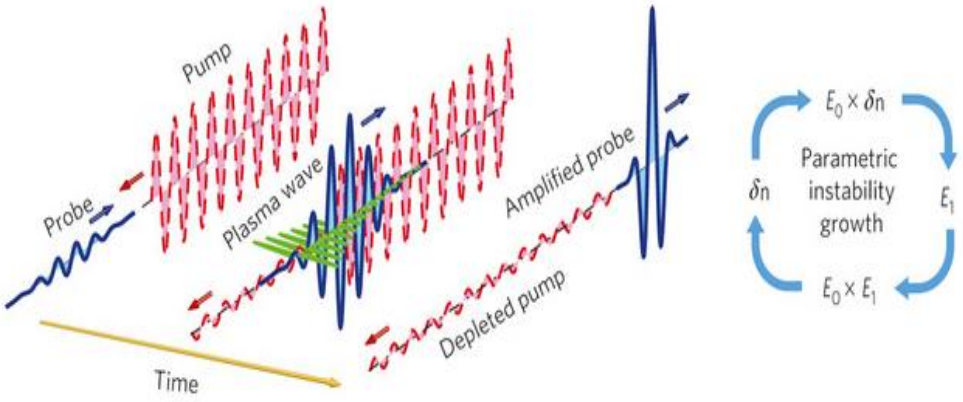

Figure 1.3.1 – Schematic illustration of processes occurring during Raman amplification where the pump, probe and plasma wave are indicated in red, blue and green, respectively [Trines et al. 2011a]

It can be seen that for a parametric instability an electromagnetic wave, E_0, couples to a density perturbation, δn the plasma wave, and generates an electromagnetic daughter wave E_1. This daughter wave in turn couples to the wave E_0 to enhance the density perturbation. The closed loop means the process is cyclic and cumulative and leads to unstable growth of both E_1 and δn.

The studies conducted of Raman scattering have previously focussed on reaching the intensity frontier which requires the production of ultrashort pulses in the femtosecond regime [Shvets et al. 1998] [Malkin, Shvets and Fisch 1999] [Ping, Cheng and Suckewer 2004] [Malkin and Fisch 2005] [Ren et al. 2007] [Kirkwood et al. 2007] [Ping et al. 2009] [Trines et al. 2011a]. More recently was the numerical and theoretical confirmation and assessment of the scalability of Raman scattering for the production of picosecond, kilojoule and petawatt laser pulses from nanosecond pulses. In this study by Trines et al. [Trines et al. 2011b] high conversion efficiencies, of up to 60%, were observed, demonstrating the suitability of this technique as a means for reaching the intensity frontier.

Although Raman amplification has been found to have great potential, energy transfer between laser beams via this instability is possible only for plasma densities less than $0.25n_c$. This means that the applicability of this technique is limited to applications where the use of such low density plasma is suitable. The energy transfer in this case is also limited since a fraction of the energy goes into the plasma wave; this is particularly important for densities close to $0.25n_c$. It is therefore pertinent to examine the use of alternative parametric instabilities as a means of energy transfer from one laser beam to another in plasma densities above which Raman amplification can be utilised.

1.4 Laser amplification via stimulated Brillouin scattering

An alternative instability which can be employed as a means of laser beam amplification in plasma is stimulated Brillouin scattering. Laser amplification via Brillouin scattering occurs when a high frequency laser pump wave is scattered by a

low frequency ion acoustic wave as opposed to a plasma wave, as is the case with Raman scattering. This process is illustrated in figure 1.4.1 and as this instability is also a parametric instability its excitation and growth is similar to that previously seen in figure 1.3.1 for Raman scattering.

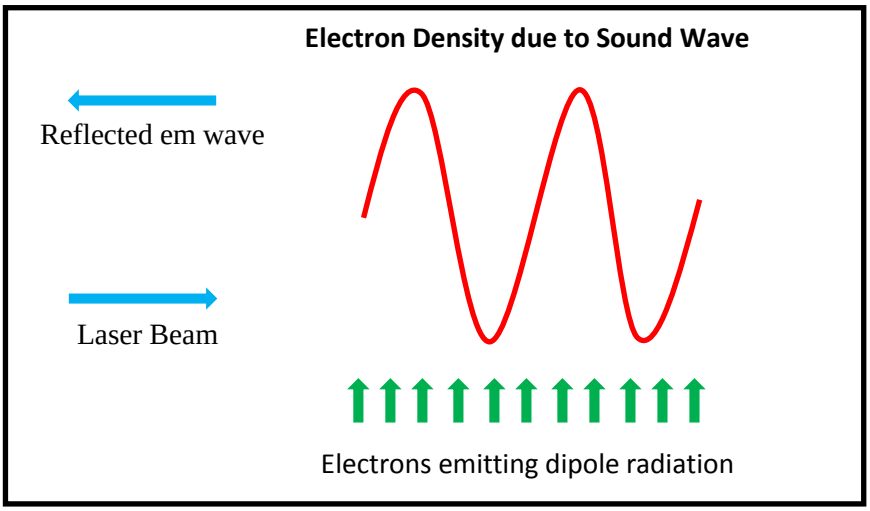

Figure 1.4.1 – Schematic representation of the Brillouin instability

The Brillouin instability, although very similar to the Raman instability, is most effectively exploited for plasma densities above $0.25n_c$, to prevent competition between modes [Kruer 2003] [Villeneuve, Baldis and Bernard 1987]. This is due to the fact that for Raman scattering the minimum frequency shift is equal to the plasma frequency, meaning the maximum density at which Raman amplification techniques can be employed is one quarter critical density; whereas for Brillouin scattering the minimum frequency shift is equal to zero allowing this mechanism to operate at all densities up to the critical density. This enables Brillouin scattering to be potentially exploited for applications where a higher plasma density is required, allowing laser amplification techniques to be employed at densities out of the range of stimulated Raman scattering. In addition to this more energy can be coupled into the scattered wave for Brillouin scattering than for Raman scattering, as less energy is coupled into the ion acoustic wave in Brillouin scattering than the Langmuir wave associated

with Raman scattering, so there exists significant potential for such a process to be harnessed to create high-energy beams.

1.5 Potential applications of plasma based laser amplification

The generation of very short ultraintense laser pulses is crucial for a number of scientific and technical applications and there are many applications for powerful laser pulses containing kilojoules of energy within a duration of 1-10 picoseconds. These include many branches of high-energy-density physics and laser-driven nuclear fusion. An example of this is in the demonstration of fast-ignition (FI) inertial confinement fusion (ICF) which requires the delivery of at least 100kJ of laser energy to the fusion target within 10-20ps to ignite the compressed fuel [Atzeni et al. 2008] [Honrubia and Meyer-ter-Vehn 2009] [Kemp, Sentoku and Tabak 2009] [Tabak et al. 1994]. Figure 1.5.1 details the orientation of the lasers with respect to the fuel pellet for FI and illustrates the role of the high power ignition beam.

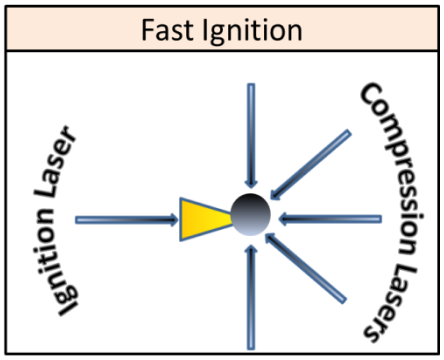

Figure 1.5.1 – Schematic diagram of the Fast Ignition ICF process

As can be seen above, the concept of fast ignition of ICF targets is the separation of the processes of thermonuclear fuel compression and heating. This separation can be performed using two temporally synchronised pulses of laser energy. The first laser driver, consisting of a series of long-pulse, high energy lasers slowly compresses the ICF target up to a density of ~300g/cm^3 and the second laser driver is used to drive a

stream of energetic electrons into the core of the compressed fuel, channeled via a gold conical structure, causing rapid heating of a small mass of pre-compressed fuel up to the thermonuclear temperature. This secondary heating process then ignites the fusion burn which propagates in the main part of the cold fuel. A schematic representation of the energy distribution of a FI capsule is shown in figure 1.5.2 where it can be seen that the potential success of this technique is dependent on the timely delivery of an ultra-high power, short-duration pulse to a small area on one side of the fuel capsule for fusion ignition to occur. As the creation of sufficiently high fuel densities has already been demonstrated the technological challenge for achieving laser fusion via Fast Ignition is therefore the creation of the high intensity, short duration ignition pulse [Key 2007]. Estimates suggest the need for pulses of picosecond duration and kilojoule energy for which Brillouin scattering could provide a useful tool.

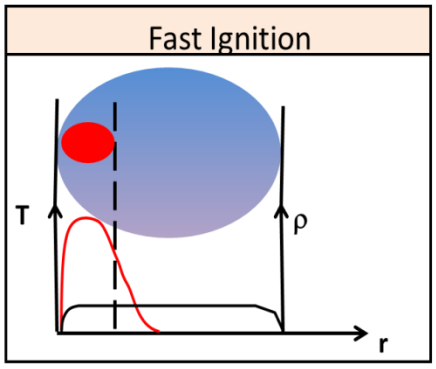

Figure 1.5.2 - Density and temperature profile of a Fast Ignition target.

Other physics research applications requiring very short duration, high energy laser pulses include monochromatic K_α x-ray [Park et al. 2006], proton beam [Borghesi et al. 2002] and Compton radiography of dense plasmas [Tommasini et al. 2008], among many others.

In each of these applications the requirement for an ultra-short high-energy pulse is particularly important; however there exists a number of additional applications where it is not a reduction in pulse length and amplification of one pulse (seed) at the cost of complete depletion of an initial pulse (pump) that is required. In some cases a tuneable energy transfer process is desired where energy can be exchanged between

pulses where the duration of each beam remains approximately constant and neither pulse is entirely depleted. One such scenario in which this is the case is in direct and indirect drive inertial confinement fusion. In these techniques induced power transfer, frequently referred to as crossed-beam energy transfer (CBET) in indirect drive ICF, occurring at the laser entrance hole (LEH) at either end of the hohlraum, takes place between adjacent laser beams and can be used as a means of controlling the symmetry of fuel capsule implosion. This particular technique is applicable for use on facilities such as the National Ignition Facility (NIF) [Lindl et al. 2004] [Glenzer et al. 2007] or the Laser Megajoule (LMJ) [Hohlstein et al. 2004] [Fleurot, Cavailler and Bourgade 2005]. Figure 1.5.3 details the configuration for indirect drive inertial confinement fusion and the positions at which energy transfer between the various laser beams can be achieved.

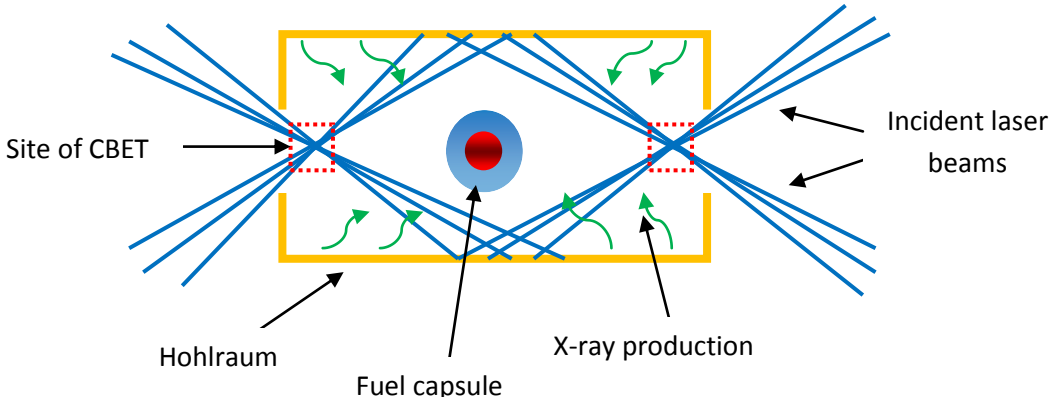

Figure 1.5.3 – Schematic diagram of the sites of CBET, shown by the red dashed regions, in indirect drive ICF

The energy profile of a capsule utilised for this technique is shown in figure 1.5.4 where it can be seen that the volume of highly compressed fuel occurs at the centre of the pellet, therefore requiring symmetrical irradiation over the entire capsule surface in order to prevent the fuel capsule breaking apart without the fusion process taking place. Thus, further highlighting the need for control over the energy balance between the irradiating lasers. In addition to the applicability of CBET to indirect drive fusion schemes, the incident laser beams in the direct drive scenario can also

interact in the expanding plasma resulting in a modification in the energy distribution to the fuel capsule in the absence of the hohlraum.

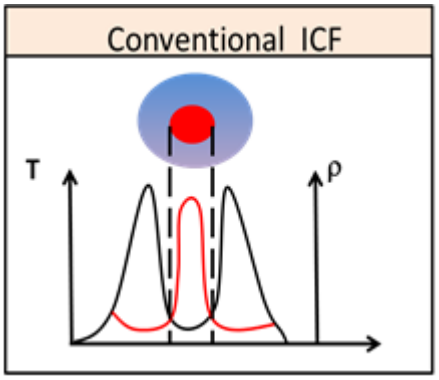

Figure 1.5.4 - Density and temperature profile of a conventional ICF target indicating the central positioning of the region of compressed mass within the fuel pellet.

1.6 Review of Brillouin scattering research

Initial work in this area began with the study of the resonant interaction between two intersecting laser beams in plasma by Kroll et al. [Kroll, Ron and Rostoker 1964] where an estimation of the scattering produced was determined and the feasibility for modern laser techniques was confirmed. This was later experimentally verified, using dye lasers, by Stansfield et.al. [Stansfield, Nodwell and Meyer 1971], where the enhancement of a scattered signal was observed due to the optical mixing of two beams when the dye lasers were tuned to the resonance of the plasma. Following this, one dimensional analytic theory of both the linear and non-linear theory of Brillouin scattering was developed [Forslund, Kindel and Lindman 1975]. This work was important in describing the linear development and non-linear saturation of the instability and the conditions necessary for achieving Brillouin back-scattering. The experimental possibility of using plasma as the non-linear medium of a parametric amplifier based on SBS was later examined by Milroy et al. [Milroy, Capjack and James 1977] [Milroy, Capjack and James 1979]. This work was applied to generate

ion acoustic waves through the Brillouin mechanism [Villeneuve, Baldis and Bernard 1987].

More recently was the investigation of energy transfer between crossing laser beams where one and two dimensional hybrid code simulations were used to model Brillouin backscatter of a pump wave into a counter-propagating seed wave with a specific frequency and input intensity [Kruer et al. 1995]. This work first showed theoretically that ion acoustic waves will be driven in the NIF where multiple laser beams intersect in a region of flowing plasma at the laser entrance hole of ignition hohlraums. This was later experimentally verified by Kirkwood et al. [Kirkwood et al. 1996] where energy transfer between two laser beams with frequency mismatch equal to the ion acoustic frequency was observed. Following this many related numerical or theoretical [Eliseev, Rozmus and Tikhonchuk 1996] [McKinstrie et al.1996] [Cohen et al. 1998] [Williams et al. 2004] [Michel et al. 2009] [Michel et al. 2010] and experimental [Wharton et al. 1998] [Kirkwood et al. 2002] [Labaune et al. 2000] [Lancia et al. 2010] studies followed.

The use of stimulated Brillouin scattering as means of compression and amplification of laser beams in plasma has also been investigated in a study conducted by A. Andreev et al. [Andreev et al. 2006]. This numerical and theoretical study focussed on the production of high intensity, short duration laser beams and the mechanisms leading to saturation of SBS in plasmas. Following this work there have been few publications concerning the optimisation of this amplification technique and the effect that physical processes such as collisions have on the overall efficiency of SBS.

1.7 Contents of this thesis

The motivation for this thesis is driven by the fact that the large majority of work already conducted in this field has focussed on the physical mechanism for achieving Brillouin scattering and subsequent observation of this process. Little attention, however, has been paid to the optimisation of this process to achieve seed pulse

amplification to ultra-high powers. In addition to this, the processes potentially affecting the efficiency of SBS in plasma such as collisions, wavebreaking and the susceptibility of this mechanism to variations in the plasma and laser parameters all require investigation in order to determine whether such a plasma based amplifier could be effectively realised.

Primarily, a numerical approach will be adopted throughout as this allows a large number of realistic and experimentally relevant laser pulse characteristics to be studied as opposed to the idealised laser-plasma configurations required to study this instability analytically; however self-similar theory and experimental data will be used to provide benchmarks for the simulation results obtained.

The structure of this thesis is as follows:

Chapter 2: This chapter presents a theoretical basis for the description of laser-plasma interactions with a bias towards parametric instability analysis.

Chapter 3: This chapter provides background information detailing the intrinsic operation of a particle-in-cell code. In particular the various features of OSIRIS, the numerical code used to conduct the simulations presented herein, will be discussed.

Chapter 4: This chapter delivers the primary simulations of stimulated Brillouin scattering in plasmas. Various features of this parametric instability, such as ion-acoustic wave generation, non-linear saturation and the efficiency of the energy transfer between beams, are investigated. The effect of including collisional processes into the calculations is also examined and comparisons drawn to SBS results presented in previously published literature.

Chapter 5: This chapter presents a theoretical model providing analysis of the scaling laws in parameter space for the optimisation of laser amplification in plasma via stimulated Brillouin scattering. The analytical theory derived here is used as a benchmark for the simulation results presented in this chapter which are used to demonstrate the effectiveness of SBS for a wide range of laser-plasma parameters.

Chapter 6: This chapter reports on the viability of achieving SBS in plasma with a single laser frequency via experimental data and corresponding numerical

simulations. The contrast between the experimental dataset and the simulation data serves as an additional benchmark for the PiC simulations documented throughout this thesis.

Chapter 7: This chapter summarises the main findings from chapters 4, 5 and 6 and indicates potential avenues for the continuation of this research project.

References

Andreev, A., Riconda, C., Tikhonchuk, V. T. and Weber, S. *Short light pulse amplification and compression by stimulated Brillouin scattering in plasmas in the strong coupling regime***.** Physics of Plasmas 13, 053110 (2006)

Atzeni S., Schiavi, A., Honrubia, J. J., Ribeyre, X., Schurtz, G., Nicolaï, Ph., Olazabal-Loumé, M., Bellei, C., Evans, R. G., and Davies, J. R. *Fast ignitor target studies for the HiPER project*. Physics of Plasmas 15, 056311 (2008)

Borghesi, M., Campbell, D. H., Schiavi, A., Haines, M. G., Willi, O., MacKinnon, A. J., Patel, P., Gizzi, L. A., Galimberti, M., Clarke, R. J., Pegoraro, F., Ruhl, H. and Bulanov, S. Electric field detection in laser-plasma interaction experiments via the proton imaging technique. Physics of Plasmas 9, 2214 (2002)

Cohen, B. I., Lasinski, B. F., Langdon, A. B., Williams, E. A., Wharton, K. B., Kirkwood, R. K. and Estabrook, K. G. *Resonant stimulated Brillouin interaction of opposed laser beams in a drifting plasma.* Physics of Plasmas 5, 3408 (1998)

Eliseev, V.V., Rozmus, W. and Tikhonchuk, V. T. *Interaction of crossed laser beams with plasmas*. Physics of Plasmas 3, 2215 (1996)

Fleurot, N., Cavailler, C. and Bourgade, J. L. *The Laser Mégajoule (LMJ) Project dedicated to inertial confinement fusion: Development and construction status.* Fusion Engineering and Design 74, 147 (2005)

Forslund, D. W., Kindel, J. M. and Lindman, E. L. *Theory of stimulated scattering processes in laser-irradiated plasmas.* Physics of Fluids 18, 1002 (1975)

Glenzer, S. H., Froula, D. H., Divol, L., Dorr, M., Berger, R. L., Dixit, S., Hammel, B. A., Haynam, C., Hittinger, J. A., Holder, J. P., Jones, O. S., Kalantar, D. H., Landen, O. L., Langdon, A. B., Langer, S., MacGowan, B. J., Mackinnon, A. J., Meezan, N., Moses, E. I., Niemann, C., Still, C. H., Suter, L. J., Wallace, R. J., Williams, E. A. and Young, B. K. F. *Experiments and multiscale simulations of laser propagation through ignition-scale plasmas.* Nature Physics 3, 716 (2007)

Hohlstein, P. A., Babonneau, D., Bowen, C., Chaland, F., Cherfils, C., Dattolo, E., Depierreux, S., Galmiche, D., Gauthier, P., Giorla, J., Jadaud, J. P., Masse, L., Monteil, M., Poggi, C. F., Riazuelo, G., Seytor, P. and Wagon, F. *Target physics for the megajoule laser (LMJ).* Nuclear Fusion 44, S177 (2004)

Honrubia, J. and Meyer-ter-Vehn, J. *Fast ignition of fusion targets by laser-driven electrons.* Plasma Physics and Controlled Fusion 51 014008 (2009)

Kemp, A.J., Sentoku, Y. and Tabak, M. *Hot-electron energy coupling in ultraintense laser-matter interaction.* Physical Review E 79, 066406 (2009)

Key, M. H. *Status of and prospects for the fast ignition inertial fusion concept.* Physics of Plasmas 14, 055502 (2007)

Key, M. H., Cable, M. D., Cowan, T. E., Estabrook, K. G., Hammel, B. A., Hatchett, S. P., Henry, E. A., Hinkel, D. E., Kilkenny, J. D., Koch, J. A., Kruer, W. L., Langdon, A. B.,Lasinski, B. F., Lee, R. W., MacGowan, B. J., MacKinnon, A., Moody, J. D., Moran, M. J., Offenberger, A. A., Pennington, D. M., Perry, M. D., Phillips, T. J., Sangster, T. C., Singh, M. S., Stoyer, M. A., Tabak, M., Tietbohl, G. L., Tsukamoto, M., Wharton, K. and Wilks, S. C. *Hot electron production and heating by hot electrons in fast ignitor research.* Physics of Plasmas 5, 1966 (1998)

Kirkwood, R. K., Afeyan, B. B., Kruer, W. L., MacGowan, B. J., Moody, J. D., Montgomery, D. S., Pennington, D. M., Weiland, T. L. and Wilks, S. C. *Observation of Energy Transfer between Frequency-Mismatched Laser Beams in a Large-Scale Plasma.* Physical Review Letters Vol. 76, No. 12 (1996)

Kirkwood, R. K., Moody, J. D., Langdon, A. B., Cohen, B. I., Williams, E. A., Dorr, M. R., Hittinger, J. A., Berger, R., Young, P. E., Suter, L. J., Divol, L., Glenzer, S. H. and Landen, O. L. *Observation of Saturation of Energy Transfer between Copropagating Beams in a Flowing Plasma*. Physical Review Letters 89, 215003 (2002)

Kirkwood, R. K., Dewald, E., Niemann, C., Meezan, N., Wilks, S. C., Price, D. W., Landen, O. L., Wurtele, J., Charman, A. E., Lindberg, R., Fisch, N. J., Malkin, V. M. and Valeo, E. O. Amplification of an ultrashort pulse laser by stimulated Raman scattering of a 1 ns pulse in a low density plasma. Physics of Plasmas 14, 113109 (2007)

Kroll, N. M., Ron, A. and Rostoker, N. *Optical Mixing as a Plasma Density Probe*. Physical Review Letters, 13, 83 (1964)

Kruer, W. L., Wilks, S. C., Afeyan, B. B. and Kirkwood, R. K. *Energy transfer between crossing laser beams.* Physics of Plasmas 3, 382 (1995)

Kruer, W. L. *The Physics of Laser Plasma Interactions* (Westview Press, Oxford (2003)

Labaune, C., Baldis, H. A., Schifano, E., Bauer, B. S., Maximov, A., Ourdev, I., Rozmus, W. and Pesme, D. *Enhanced Forward Scattering in the Case of Two Crossed Laser Beams Interacting with a Plasma*. Physical Review Letters 85, 1658 (2000)

Lancia, L., Marquès, J. R., Nakatsutsumi, M., Riconda, C., Weber, S., Hüller, S., Mančić, A., Antici, P., Tikhonchuk, V. T., Héron, A., Audebert, P. and Fuchs, J. *Experimental Evidence of Short Light Pulse Amplification Using Strong-Coupling Stimulated Brillouin Scattering in the Pump Depletion Regime*. Physical Review Letters 104, 025001 (2010)

Lindl, J. D., Amendt, P., Berger, R. L., Glendinning, S. G., Glenzer, S. H., Haan, S. W., Kauffman, R. L., Landen, O. L. and Suter, L. J. *The physics basis for ignition using indirect-drive targets on the National Ignition Facility*. Physics of Plasmas 11, 339 (2004)

Maiman, T.H. *Stimulated Optical Radiation in Ruby*. Nature 187, 493 (1960)

Malkin, V. M., Shvets, G. and Fisch, N. J. *Fast Compression of Laser Beams to Highly Overcritical Powers.* Physical Review Letters 82, 4448 (1999)

Malkin, V. M. and Fisch, N. J. *Manipulating ultraintense laser pulses in plasmas.* Physics of Plasmas 12, 044 507 (2005)

McKinstrie, C. J., Li, J. S., Giacone, R. E. and. Vu, H. X. *Two-dimensional analysis of the power transfer between crossed laser beams.* Physics of Plasmas 3, 2686 (1996)

Michel, P., Divol, L., Williams, E. A., Weber, S., Thomas, C. A., Callahan, D. A., Haan, S. W., Salmonson, J. D., Dixit, S., Hinkel, D. E., Edwards, M. J., MacGowan, B. J., Lindl, J. D., Glenzer, S. H. and Suter, L. J. *Tuning the Implosion Symmetry of ICF Targets via Controlled Crossed-Beam Energy Transfer*. Physical Review Letters 102, 025004 (2009)

Michel, P., Glenzer, S. H., Divol, L., Bradley, D. K., Callahan, D., Dixit, S., Glenn, S., Hinkel, D., Kirkwood, R. K., Kline, J. L., Kruer, W. L., Kyrala, G. A., Le Pape, S., Meezan, N. B., Town, R., Widmann, K., Williams, E. A., MacGowan, B. J.,

Lindl, J. and Suter, L. J. *Symmetry tuning via controlled crossed-beam energy transfer on the National Ignition* Facility. Physics of Plasmas 17, 056305 (2010)

Milroy, R. D., Capjack, C. E. and James, C. R. *Plasma laser pulse amplifier using induced Raman or Brillouin processes.* Physics of Fluids 22, 1922 (1979)

Milroy, R. D., Capjack, C. E. and James, C. R. *A plasma-laser amplifier in the 11-16μm wavelength range.* Plasma Physics 19, 989 (1977)

Mourou, G. A., Barty, C. P. J. and Perry, M. D. *Ultrahigh-intensity lasers: Physics of the extreme on a tabletop*. Physics Today, vol. 51, no. 1, pp. 22–28 (1998)

Park, H. S., Chambers, D. M., Chung, H. K., Clarke, R. J., Eagleton, R., Giraldez, E., Goldsack, T., Heathcote, R., Izumi, N., Key, M. H., King, J. A., Koch, J. A., Landen, O. L., Nikroo, A., Patel, P. K., Price, D. F., Remington, B. A., Robey, H. F., Snavely, R. A., Steinman, D. A., Stephens, R. B., Stoeckl, C., Storm, M., Tabak, M., Theobald, W., Town, R. P. J., Wickersham, J. E. and Zhang, B. B. *High-energy Kα radiography using high-intensity, short-pulse lasers.* Physics of Plasmas 13, 056309 (2006)

Paschotta, R. *Encyclopedia of Laser Physics and Technology*. John Wiley & Sons (2008)

Ping. Y., Cheng, W. and Suckewer, S. *Amplification of ultrashort laser pulses by a resonant Raman scheme in a gas-jet plasma.* Physical Review Letters 92, 175007 (2004)

Ping, Y., Kirkwood, R. K., Wang, T.-L., Clark, D. S., Wilks, S. C., Meezan, N.,Berger, R. L., Wurtele, J., Fisch, N. J., Malkin, V. M., Valeo, E. J., Martins, S. F., and Joshi, C. *Development of a nanosecond-laser-pumped Raman amplifier for short laser pulses in plasma.* Physics of Plasmas 16, 123113 (2009)

Ren, J., Cheng, W., Li, S. and Suckewer, S. *A new method for generating ultraintense and ultrashort laser pulses*. Nature Physics 3, 732 (2007)

Shvets, G., Fisch, N. J., Pukhov, A. and Meyer-ter-Vehn, J. *Superradiant Amplification of an Ultrashort Laser Pulse in a Plasma by a Counterpropagating Pump.* Physical Review Letters 81, 4448 (1998)

Stansfield, B. L., Nodwell, R. and Meyer, J. *Enhanced Scattering of Laser Light by Optical Mixing in a Plasma.* Physical Review Letters 26 ,1219 (1971)

Strickland, D. and Mourou, G. *Compression of amplified chirped optical pulses*. Optics Communications 55, 447 (1985)

Tabak, M., Hammer, J., Glinsky, M. E., Kruer, W. L., Wilks, S. C., Woodworth, J., Campbell, E. M., Perry, M. D. and Mason, R. J. *Ignition and high gain with ultrapowerful lasers*. Physics of Plasmas 1, 1626 (1994)

Tommasini, R., Macphee, A., Hey, D., Ma, T., Chen, C., Izumi, N., Unites, W., Mackinnon, A., Hatchett, S. P., Remington, B.A., Park, H.S., Springer, P., Koch, J.A., Landen, O.L., Seely, J., Holland, G., Hudson, L. *Development of backlighting sources for a Compton radiography diagnostic of inertial confinement fusion targets.* Review of Scientific Instruments 79, 10E901 (2008)

Trines, R. M. G. M., Fiúza, F., Bingham, R., Fonseca, R. A., Silva, L. O., Cairns, R. A. and Norreys, P. A. *Simulations of efficient Raman amplification into the multipetawatt regime.* Nature Physics 7, 87 (2011a)

Trines, R. M. G. M., Fiúza, F., Bingham, R., Fonseca, R. A., Silva, L. O., Cairns, R. A. and Norreys, P. A. *Production of Picosecond, Kilojoule, and Petawatt Laser Pulses via Raman Amplification of Nanosecond Pulses*. Physical Review Letters 107, 105002 (2011b)

Villeneuve, D. M., Baldis, H. A. and Bernard, J. E. *Suppression of Stimulated Raman Scattering by the Seeding of Stimulated Brillouin Scattering in a Laser-Produced Plasma*. Physical Review Letters Vol.59, No.14 (1987)

Williams, E. A., Cohen, B. I., Divol, L., Dorr, M. R., Hittinger, J. A., Hinkel, D. E., Langdon, A. B., Kirkwood, R. K., Froula, D. H. and Glenzer, S. H. *Effects of ion trapping on crossed-laser-beam stimulated Brillouin scattering.* Physics of Plasmas 11, 231 (2004)

Wharton, K. B., Kirkwood, R. K., Glenzer, S. H., Estabrook, K. G., Afeyan, B. B., Cohen, B. I., Moody, J. D. and Joshi, C. *Observation of Energy Transfer between Identical-Frequency Laser Beams in a Flowing Plasma.* Physical Review Letters 81, 2248 (1998)

The role of the author

The complex nature of the intense laser-plasma interactions studied throughout this body of work, via experimental, analytical and computational methods, necessitates the involvement of a range of different people. This section details the role of the author in the results presented throughout this thesis.

The results from the particle in cell simulations presented in chapter 4, detailing the role of damping effects on amplification of laser beams by Stimulated Brillouin Scattering, were the product of the author's individual study. This includes, but is not limited to, the numerical setup and parameter regimes chosen to the post simulation analysis and interpretation of the results. This data was used in the "Effect of collisions on amplification of laser beams by Brillouin scattering in plasmas" publication in Physics of Plasmas*.

The results detailed in chapter 5, for the optimisation of Stimulated Brillouin Scattering in parameter space, were the outcome from a collaborative effort by the author and R.M.G.M Trines of the Rutherford Appleton Laboratory. The author's role in this work comprised the selection and setup of the parameter sets studied, analysis of the simulation output and conducting benchmarking exercises between the numerical simulations and the analytical theory. The analytical theory itself was developed by R.M.G.M Trines.

The experimental and numerical results presented in chapter 6, which demonstrate Stimulated Brillouin Scattering with a single laser frequency, were also the product of a collaborative effort. The author conducted the simulations in accordance with the parameter regimes studied in the experimental campaign, analysed the simulation output presented and provided significant assistance in analysing the experimental data collected by E. Guilliame et. al.. The results of this collaboration were used in the "Demonstration of laser pulse amplification by stimulated Brillouin scattering", submitted to High Power Laser Science and Engineering *.

* A copy of this paper can be found in the Appendix.

Chapter 2
Theory of laser-plasma interactions

This chapter presents a theoretical framework describing the physical processes fundamental to understanding laser interactions with underdense plasma. Equations underpinning the kinetic description of a plasma, electromagnetic wave propagation and descriptions of specific beam-plasma and laser-plasma instabilities, under investigation as part of this body of research, will be presented.

2.1 Basic plasma concepts

Plasma can be described as a quasi-neutral gas of charged and neutral particles that exhibits collective behaviour, containing enough free charged particles such that its dynamics are dominated by long range electromagnetic interactions as opposed to interatomic or intermolecular forces, among a large number of particles [Thompson 1962]. The combination of low electron inertia and strong electrostatic field, which arises from even the slightest charge imbalance, results in a rapid flow of electrons to re-establish neutrality [Boyd and Sanderson 2003].

An important parameter used to provide a description of the behaviour of plasma is the Debye length, λ_D, which corresponds to the exponential length for charge screening within an electron plasma with stationary ions. This quantity is given by:

$$\lambda_D = \left(\frac{\varepsilon_0 k_B T_e}{n_e e^2}\right)^{1/2} \tag{2.1.1}$$

where ε_0 is the is the permittivity of free space, k_B is the Boltzmann constant, T_e is the electron temperature, n_e is the electron number density and e is the electronic charge. The Debye length also gives a measure of the penetration depth of external electrostatic fields, beyond which the plasma remains effectively neutral.

An essential requirement for (2.1.1) is that a large number of electrons be present within the Debye sphere i.e. $n_e{\lambda_D}^3 \gg 1$. The inverse of this number is proportional to the ratio of potential energy to kinetic energy in the plasma and is termed the plasma parameter, g:

$$g = \frac{e^2}{\varepsilon_0 k_B T_e \lambda_D} = \frac{1}{n_e{\lambda_D}^3} \ll 1 \qquad (2.1.2)$$

In order for an ionized gas to be described as a plasma two specific conditions must be satisfied, such that:

i) The assembly of charged particles must be large enough that it is many Debye lengths in size.
ii) The collection of particles must be of such a density that there are many particles present in the Debye sphere.

Such plasmas are weakly correlated with long range interactions, through collective effects, being dominant. In the opposite limit, where $g \geq 1$, the plasma is dominated by strong correlation.

2.2 Plasma characteristics

When a charge imbalance exists within plasma, the strong electrostatic fields which drive the electrons to re-establish neutrality cause oscillations around the position of equilibrium at a specific characteristic frequency. This is the plasma frequency, ω_{pe}:

$$\omega_{pe} = \frac{(k_B T_e / m_e)^{1/2}}{\lambda_D} = \left(\frac{n_e e^2}{m_e \varepsilon_0}\right)^{1/2} \quad (2.2.1)$$

Where m_e is the electronic mass.

Applied fields with frequencies less than the plasma frequency are prevented from penetrating the plasma by the more rapid electron response, causing neutralisation of the field. The corresponding frequency for ions is the ion plasma frequency, ω_{pi}, and is given by:

$$\omega_{pi} = \left(\frac{n_i (Ze)^2}{m_i \varepsilon_0}\right)^{1/2} \quad (2.2.2)$$

Where n_i is the ion number density, Z is the charge state and m_i is the ion mass.

In plasmas where collisional effects are taken into account, the collisional frequency, f_{cs}, is the average rate at which inter-particle collisions take place, for simplicity it is assumed here to be between a mobile species (labelled with subscript 's') and a stationary one. The general formula is given by:

$$\nu_{cs} = n_n \sigma_{sc,s} \langle U_s \rangle \quad (2.2.3)$$

Where n_n is the number density of stationary targets, $\sigma_{sc,s}$ is the scattering cross-section and $\langle U_s \rangle$ is the mean speed of the mobile species.

The collisional time, τ_c, is the reciprocal of the collisional frequency:

$$\tau_c = \frac{1}{n_n \sigma_{sc} \langle u \rangle} \quad (2.2.4)$$

Where $\langle u \rangle$ is the mean speed of the colliding particles.

The total scattering cross section, σ_{sc}, is represented by:

$$\sigma_{sc} = 2\pi \int_0^{\pi} I(v, \theta)\, d\theta \quad (2.2.5)$$

Where $I(v, \theta)$ is the differential scattering cross section, v is the relative speed of the scattered particle compared with the target and θ is the angle through which the particle is scattered by the collision.

The average distance a particle moves before successive collisions or interactions is the mean free path, λ_{mfp}:

$$\lambda_{mfp} = (n_n \sigma_{sc})^{-1} \tag{2.2.6}$$

Typically, the smaller the value of λ_{mfp} the more collisions a single particle will experience while traversing a given plasma volume, leading to more significant modifications to the particle velocity and/or energy.

2.3 Plasma kinetic description

For all of the simulation results presented in this thesis the plasma kinetic model that is incorporated into the OSIRIS particle-in-cell code is used. The formulation of a complete mathematical model of a plasma consists of three main constituents. These include [Clemmow and Dougherty 1969]:

1) The motion of all particles must be determined for some assumed electric and magnetic field configuration.

2) The current and charge densities must be computed from the particle trajectories.

3) The electric and magnetic fields must be self-consistently determined from the currents and charges, taking into account both internal and external sources.

Kinetic theory provides the most complete plasma description by combining both microscopic and macroscopic descriptions and illuminating the information relating to the distribution of velocities of the particles within a fluid element which is lost by the fluid model.

This approach describes the plasma via the evolution of distribution functions in six dimensions. The distribution function:

$$f_s(\boldsymbol{r}, \boldsymbol{v}, t) \tag{2.3.1}$$

is the density of particles in $(\boldsymbol{r}, \boldsymbol{v})$ space at time, t. Where the subscript 's' denotes the particular particle species i.e. ions/electrons.

At the fundamental level the distribution function can be defined in terms of the individual particle positions and velocities by:

$$f_K(\boldsymbol{r},\boldsymbol{v},t) = \sum_{i=1}^{N} \delta[\boldsymbol{r} - \boldsymbol{r_i}(t)]\,\delta[\boldsymbol{v} - \boldsymbol{v_i}(t)] \tag{2.3.2}$$

Equation (2.3.2) is referred to as the Klimontovich distribution function and the sum is over all particles of a single particular species. Upon integration a collisional kinetic equation describing the evolution of the distribution function, known as the Vlasov equation, is obtained:

$$\frac{\partial \boldsymbol{f}}{\partial t} + \boldsymbol{v} \cdot \frac{\partial \boldsymbol{f}}{\partial \boldsymbol{r}} + \frac{q\boldsymbol{E}}{m} \cdot \frac{\partial \boldsymbol{f}}{\partial \boldsymbol{v}} = 0 \tag{2.3.3}$$

Where F in this case is defined as the Lorentz force:

$$\boldsymbol{F} = \frac{d\boldsymbol{p}}{dt} = -e(\boldsymbol{E} + v \times \boldsymbol{B}) \tag{2.3.4}$$

In the absence of collisions $\boldsymbol{f}$ is constant along any trajectory in $(\boldsymbol{r},\boldsymbol{v})$ space, however by taking the collisions into consideration (2.3.3) becomes:

$$\frac{\partial \boldsymbol{f}}{\partial t} + \boldsymbol{v} \cdot \frac{\partial \boldsymbol{f}}{\partial \boldsymbol{r}} + \frac{\boldsymbol{F}}{m} \cdot \frac{\partial \boldsymbol{f}}{\partial \boldsymbol{v}} = \left(\frac{\partial \boldsymbol{f}}{\partial t}\right)_c \tag{2.3.5}$$

Where $\left(\frac{\partial \boldsymbol{f}}{\partial t}\right)_c$ represents the change in $\boldsymbol{f}$ with time due to collisional effects.

The kinetic model is effective in providing a description of a plasma where individual particles cannot be ignored. This description is of importance in cases such as the study of instabilities where the particle motions depend on a mathematically complex distribution function.

2.4 Basic wave concepts

The basic properties of electromagnetic radiation can be revealed by studying their propagation in free space, outside the region of changing charge and current distributions [Lorrain, Corson and Lorrain 1988] [Dobbs 1985] [Cook 1975]. Expressions for the electric, $\boldsymbol{E}$, and magnetic field, $\boldsymbol{B}$, propagation are given by:

$$\nabla^2 \boldsymbol{E} - \frac{1}{c^2}\frac{\partial^2 \boldsymbol{E}}{\partial t^2} = 0 \tag{2.4.1}$$

$$\nabla^2 \boldsymbol{B} - \frac{1}{c^2}\frac{\partial^2 \boldsymbol{B}}{\partial t^2} = 0 \tag{2.4.2}$$

Where c is the propagation speed of the electromagnetic radiation:

$$\mathrm{c} = \frac{1}{\sqrt{\varepsilon_0 \mu_0}} \tag{2.4.3}$$

For the plane wave solutions, where the wave disturbance is constant over all points of a plane normal to the direction of propagation of the wave:

$$\mathbf{E}(\mathbf{r}, \mathrm{t}) = \boldsymbol{E_0} \exp[i(\boldsymbol{k} \cdot \boldsymbol{r} - \omega t)] \tag{2.4.4}$$

$$\mathbf{B}(\mathbf{r}, \mathrm{t}) = \boldsymbol{B_0} \exp[i(\boldsymbol{k} \cdot \boldsymbol{r} - \omega t)] \tag{2.4.5}$$

the vacuum divergence equations require that $\boldsymbol{k} \cdot \boldsymbol{E_0} = 0 = \boldsymbol{k} \cdot \boldsymbol{B_0}$ so that $(\boldsymbol{E}, \boldsymbol{B}, \boldsymbol{k})$ form a triad of orthogonal vectors, where k is the wavevector of the wave.
The electric field in a plane wave is expressed, in general, by a superposition of two linearly independent solutions of the wave equation. Choosing the z-axis along the wave vector k gives:

$$(\mathrm{z}, \mathrm{t}) = \left[E_{x0}\boldsymbol{x} + E_{y0}\, e^{i\delta}\boldsymbol{y}\right] \exp[i(\boldsymbol{k}z - \omega t + \alpha)] \tag{2.4.6}$$

where E_{x0} and E_{y0} are real, E_x and E_y are complex amplitudes:

$$\mathrm{E}_X = E_{x0} \exp(i\alpha) \tag{2.4.7}$$

$$\mathrm{E}_y = E_{y0} \exp(i\beta) \tag{2.4.8}$$

and $\delta = \beta - \alpha$ [Allen and Phelps 1977].

By setting $\delta = \pm \pi/2$ it can be shown that at each point in space the electric field vector rotates in a plane normal to $\hat{z}$ and as time evolves its tip describes an ellipse. Therefore, typically, a plane wave is elliptically polarised. For the case where E_{x0} or

E_{y0}= 0 the electric field is linearly polarised while if E_{x0} = E_{y0} then the field is said to be circularly polarised.

In practice, even with such a monochromatic source as a laser, there will be a spread in frequency and wavenumber. Typically, as $\omega = \omega(k)$, a waveform will change as it propagates through the media, exhibiting dispersion. The velocity of propagation of the wave packet, termed the group velocity, v_g, is:

$$v_g = \frac{d\omega}{dk} = c\left(1 - \frac{\omega_{pe}^2}{\omega^2}\right)^{1/2} \tag{2.4.9}$$

and the velocity at which the phase of any one frequency component of the wave travels, characterised by the phase velocity, v_{ph}, is:

$$v_{ph} = \frac{\omega}{k} \tag{2.4.10}$$

The form of a typical dispersion curve for an electromagnetic wave is seen in Figure 2.4.1.

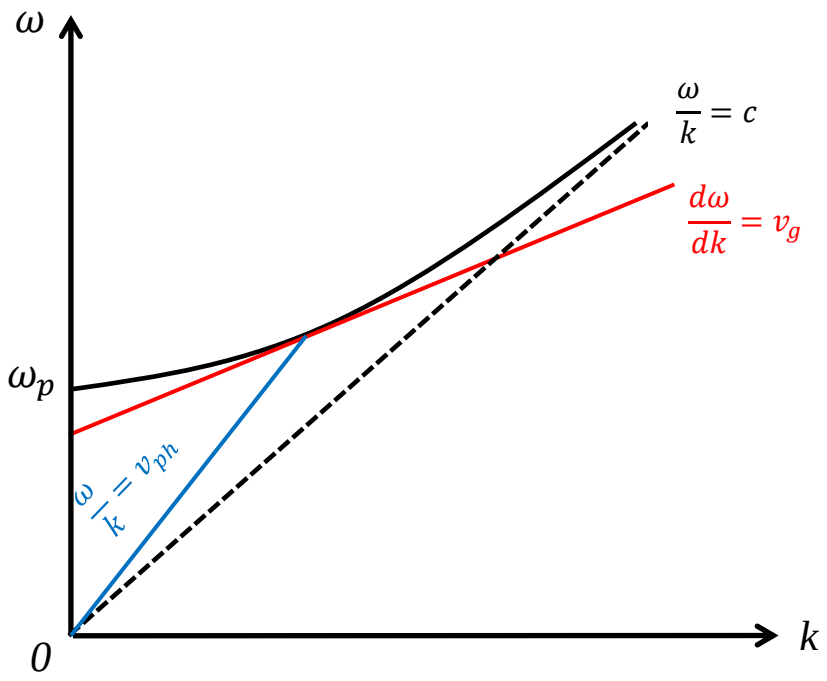

Figure 2.4.1 – Characteristic EM wave dispersion curve

2.5 Wave propagation in unbounded homogenous plasma

Wave phenomena in collisionless plasma is very well described by cold plasma theory [Boyd and Sanderson 2004] [Grant and Phillips 1990] [Tonks and Langmuir 1929], where the thermal speeds of the particles are much smaller than the phase speeds of the waves.

In this section the following assumptions are made regarding the plasma:

■ The plasma is regarded as a cold electron fluid, including the effects of Debye shielding.

■ The plasma is fully ionized.

■ The plasma is globally charge neutral.

■ The ions are immobile and have a background density n_0.

The cold plasma equations consist of the ion and electron equations of continuity and motion in the electromagnetic (EM) fields. These EM fields are governed by Maxwell's equations:

$$\boldsymbol{\nabla} \cdot \boldsymbol{E} = \frac{\rho}{\varepsilon_0} \tag{2.5.1}$$

$$\boldsymbol{\nabla} \cdot \boldsymbol{B} = 0 \tag{2.5.2}$$

$$\boldsymbol{\nabla} \times \boldsymbol{E} = -\frac{\partial \boldsymbol{B}}{\partial t} \tag{2.5.3}$$

$$\boldsymbol{\nabla} \times \boldsymbol{B} = \mu_0 \left(\boldsymbol{J} + \varepsilon_0 \frac{\partial \boldsymbol{E}}{\partial t} \right) \tag{2.5.4}$$

where (2.5.1) and (2.5.2) give Gauss' law for the electric and magnetic fields, respectively, (2.5.3) is Faradays' law and (2.5.4) is the modified version of Amperes' law, ρ is the total charge density, ε_0 is the permittivity of free space, μ_0 is the permeability of free space and $\boldsymbol{J}$ is the total current density [Pozar 2005]. The following relations hold between the electric and magnetic field intensities and flux densities:

$$\mathbf{B} = \mu_0 \boldsymbol{H} \tag{2.5.5}$$

$$\mathbf{D} = \varepsilon_0 \boldsymbol{E} \tag{2.5.6}$$

where $\boldsymbol{H}$ is the magnetic field strength and $\boldsymbol{D}$ is the electric flux density.
The linearized version of the cold plasma equations are [Boyd 2003]:

$$\frac{\partial n_1}{\partial t} + \boldsymbol{\nabla} \cdot (n_0 \boldsymbol{v_1}) = 0 \tag{2.5.7}$$

$$\frac{\partial \boldsymbol{v_1}}{\partial t} = \frac{e}{m} (\boldsymbol{E}_1 + \boldsymbol{v_1} \times \boldsymbol{B_0}) \tag{2.5.8}$$

$$\boldsymbol{\nabla} \times \boldsymbol{E_1} = -\frac{\partial \boldsymbol{B_1}}{\partial t} \tag{2.5.9}$$

$$\boldsymbol{\nabla} \times \boldsymbol{B_1} - \frac{1}{c^2} \frac{\partial \boldsymbol{E_1}}{\partial t} = \mu_0 \boldsymbol{j} = \mu_0 \sum e n_0 \boldsymbol{v_1} \tag{2.5.10}$$

$$\boldsymbol{\nabla} \cdot \boldsymbol{E_1} = \frac{q}{\varepsilon_0} = \frac{1}{\varepsilon_0} \sum e n_1 \tag{2.5.11}$$

$$\boldsymbol{\nabla} \cdot \boldsymbol{B_1} = 0 \tag{2.5.12}$$

Where the sums in (2.5.10) and (2.5.11) are over species and:

$$\left.\begin{aligned} n &= n_0 + n_1 \\ \boldsymbol{u} &= \boldsymbol{u_1} \\ \boldsymbol{E} &= \boldsymbol{E_1} \\ \boldsymbol{B} &= \boldsymbol{B_0} + \boldsymbol{B_1} \end{aligned}\right\} \tag{2.5.13}$$

with n_0 and B_0 constant in time and space and the subscript 1 denoting a first order perturbation of the initial field quantities labelled with a subscript 0. In this analysis we consider the fluid to be stationary. The identities in (2.5.11) and (2.5.12) are essentially initial conditions, therefore if they are satisfied at t = 0 then they are satisfied for all t > 0.

By assuming all variables vary like $\exp[i(\boldsymbol{k} \cdot \boldsymbol{r} - \omega t)]$ [Clemmow and Dougherty 1969], the wave equation for the electric field can be expressed as:

$$(\mathbf{n} \times \mathbf{n} \times \boldsymbol{E_1}) = -\boldsymbol{E_1} - \frac{i}{\varepsilon_0 \omega} \boldsymbol{\sigma} \cdot \boldsymbol{E_1} = -\epsilon \cdot \boldsymbol{E_1} \tag{2.5.14}$$

where $\boldsymbol{n} = c\boldsymbol{k}/\omega$ is a dimensionless wave propagation vector, $\boldsymbol{\sigma}$ is the conductivity tensor and ϵ is the cold plasma dielectric tensor which is written in matrix format and takes the form:

$$\varepsilon = \begin{bmatrix} S & -iD & 0 \\ iD & S & 0 \\ 0 & 0 & P \end{bmatrix} \tag{2.5.15}$$

with components:

$$\left.\begin{aligned} S = \frac{1}{2}(R+L) &= 1 - \frac{\omega_p^2\,(\omega^2 + \Omega_i\Omega_e)}{(\omega^2 - \Omega_i^2)(\omega^2 - \Omega_e^2)} \\ D = \frac{1}{2}(R-L) &= \frac{\omega_p^2\omega(\Omega_i + \Omega_e)}{(\omega^2 - \Omega_i^2)(\omega^2 - \Omega_e^2)} \\ R &= 1 - \frac{\omega_p^2}{(\omega + \Omega_i)(\omega + \Omega_e)} \\ L &= 1 - \frac{\omega_p^2}{(\omega - \Omega_i)(\omega - \Omega_e)} \\ P &= 1 - \frac{\omega_p^2}{\omega^2} \end{aligned}\right\} \qquad (2.5.16)$$

where $\boldsymbol{B_0}$ is assumed to be in the z-direction and $\omega_p^2 = \omega_{pi}^2 + \omega_{pe}^2$ is the square of the plasma frequency.

As equation (2.5.14) requires a non-trivial solution this allows the dispersion relation containing all of the information about linear wave propagation in cold plasma to be obtained. By choosing the axis such that the wave propagation direction $\boldsymbol{n} = (n\sin\theta\,, 0, \mathrm{n}\cos\theta)$, (2.5.13) may be written:

$$(\mathbf{n}\cdot\mathbf{E})\mathbf{n} - n^2\boldsymbol{E} + \epsilon\cdot\boldsymbol{E} = 0 \qquad (2.5.17)$$

and hence:

$$\begin{bmatrix} S - n^2\cos\theta & -iD & n^2\cos\theta\sin\theta \\ iD & S - n^2 & 0 \\ n^2\cos\theta\sin\theta & 0 & P - n^2\sin^2\theta \end{bmatrix} \begin{bmatrix} E_x \\ E_y \\ E_z \end{bmatrix} = 0 \qquad (2.5.18)$$

Thus the general dispersion relation for cold plasma waves, obtained by taking the determinant of the coefficients, is:

$$\mathrm{An}^4 - \mathrm{Bn}^2 + C = 0 \qquad (2.5.19)$$

where:

$$\left.\begin{aligned} \mathrm{A} &= \mathrm{S}\sin^2\theta + P\cos^2\theta \\ B &= RL\sin^2\theta + PS\,(1 + \cos^2\theta) \\ C &= PRL \end{aligned}\right\} \qquad (2.5.20)$$

The solutions of (2.5.18) for n^2 require to have real roots only. This is due to the fact that the cold, non-streaming plasma equations contain no sources of free energy to drive instabilities and no dissipation terms to produce decaying waves. This means that the values of n are either purely real corresponding to wave propagation or pure imaginary corresponding to evanescence. The transition at which wave propagation transforms to evanescence occurs when n^2 passes through zero or infinity.

The first case corresponding to $n^2 = 0$ occurs when $C = 0$ invoking the condition that P, R or L must equal zero. These correspond to cut-off frequencies and define values above or below which the wave ceases to propagate at any angle (i.e. $v_p \rightarrow \infty$), for given equilibrium conditions. The cut-off frequencies are represented by:

$$\left.\begin{aligned} &\mathrm{P} = 0: \quad \omega = \omega_p \\ &R = 0: \quad \omega = \left[\omega_p^2 + \frac{(\Omega_i - \Omega_i)^2}{4}\right]^{1/2} - (\Omega_i + \Omega_e)/2 \equiv \omega_R \\ &L = 0: \quad \omega = \left[\omega_p^2 + \frac{(\Omega_i - \Omega_i)^2}{4}\right]^{1/2} + (\Omega_i + \Omega_e)/2 \equiv \omega_L \end{aligned}\right\} \tag{2.5.21}$$

The second case corresponding to $n^2 \rightarrow \infty$ occurs when $A = 0$. This case corresponds to a resonance, where $v_p \rightarrow 0$. This does not necessarily mean that a wave is unable to propagate but defines for a given set of parameters a resonant angle, θ_{res}, above or below which the wave does not propagate, defined by:

$$\tan^2\theta_{res} = -\frac{P}{S} \tag{2.5.22}$$

A wave that experiences a resonance will propagate either for:

$$\text{Case (a)}: \ 0 \leq \theta < \theta_{res} \text{ but not } \theta_{res} < \theta \leq \pi/2 \tag{2.5.23}$$

$$\text{Case (b)}: \ \theta_{res} < 0 \leq \pi/2 \text{ but not } 0 \leq \theta \leq \theta_{res} \tag{2.5.24}$$

We can therefore see that in case (a) when $\theta_{res} \rightarrow 0$, or in case (b) when $\theta_{res} \rightarrow \pi/2$ that the wave is unable to propagate. These are the principle resonances and like the cut-offs they define frequencies above or below which a particular wave does not propagate. From (2.5.21) the principle resonances occur at:

$$\theta_{res} = 0 : \quad \mathrm{P} = 0 \text{ or } \mathrm{S} = \frac{1}{2}(R + L) \to \infty \tag{2.5.25}$$

$$\theta_{res} = \frac{\pi}{2} : \quad \mathrm{S} = 0 \tag{2.5.26}$$

For case (a) it has already been shown that $P = 0$ is a cut-off where n^2 = 1 and case (b) provides two resonances such that either:

$$R \to \infty \text{ as } \omega \to -\Omega_e = |\Omega_e| \tag{2.5.27}$$

which is the electron cyclotron resonance, or:

$$L \to \infty \text{ as } \omega \to \Omega_i \tag{2.5.28}$$

which is the ion cyclotron resonance.

The cyclotron resonances occurring at $\theta = 0$ involve only a single species; however the resonances occurring at $\pi/2 = 0$ involve both the ions and electron species and are therefore known as the hybrid resonances:

$$\omega_{UH}^2 \simeq \left(\omega_p^2 + \Omega_i^2 + \Omega_e^2\right) \simeq \omega_{pe}^2 + \Omega_e^2 \tag{2.5.29}$$

$$\omega_{LH}^2 \simeq -\frac{\Omega_i\Omega_e\left(\omega_p^2 - \Omega_i\Omega_e\right)}{\omega_p^2 + \Omega_i^2 + \Omega_e^2} \simeq \begin{cases} |\Omega_i\Omega_e| & \left(\omega_p^2 \gg \Omega_e^2\right) \\ \omega_{pi}^2 + \Omega_i^2 & (\omega_p^2 \ll \Omega_e^2 \end{cases} \tag{2.5.30}$$

where the subscripts UH and LH denote upper hybrid and lower hybrid waves respectively.

Following from this analysis three distinct instances of wave propagation can be examined [Stringer 1963]. These include:

■ Field free plasma ($\boldsymbol{B_0} = \boldsymbol{0}$)

■ Parallel propagating waves ($\boldsymbol{k}//\boldsymbol{B_0}$)

■ Perpendicular propagating waves ($\boldsymbol{k} \perp \boldsymbol{B_0}$)

As there are no externally imposed magnetic fields imposed throughout the work contained within this thesis, analysis here will be restricted to the first case listed above which is wave propagation in field free plasma.

Field free plasma

For the case of a field free plasma, where $\boldsymbol{B_0} = 0$, there is no preferred propagation direction. Again taking z to be the direction of propagation, i.e. $\theta = 0$ and so $S = P$ and $D = 0$, (2.5.17) takes the form:

$$\begin{bmatrix} 1 - \frac{\omega_{pe}^2}{\omega^2} - n^2 & 0 & 0 \\ 0 & 1 - \frac{\omega_{pe}^2}{\omega^2} - n^2 & 0 \\ 0 & 0 & 1 - \frac{\omega_{pe}^2}{\omega^2} \end{bmatrix} \begin{bmatrix} E_x \\ E_y \\ E_z \end{bmatrix} = 0 \qquad (2.5.31)$$

In this case there are two solutions relating to two types of wave. Either $\boldsymbol{E} = (0, 0, E_z)$ for which the dispersion relation is:

$$\omega^2 = \omega_{pe}^2 \qquad (2.5.32)$$

or $E_z = 0$ and therefore:

$$\omega^2 = \omega_{pe}^2 + k^2 c^2 \qquad (2.5.33)$$

By including finite temperature effects, the dispersion relation becomes:

$$\omega^2 = \omega_{pe}^2 + 3 v_e^2 k^2 \qquad (2.5.34)$$

The first solution corresponds to a plasma resonance and is generally referred to as the Bohm and Gross formula [Bohm 1949]. Due to the fact that within the cold plasma limit the group velocity of the longitudinal wave is equal to zero this wave is unable to propagate. From (2.5.9) it can be seen that it is an electrostatic wave as $\boldsymbol{B_1} = 0$. The second solution relates to a transverse wave propagating in a direction perpendicular to the electric field.

As the plasma frequency is the natural frequency with which the plasma responds to any electric field imposed on it there exists a cut-off frequency a field must exceed in order for a wave to propagate within the plasma. This is due to the fact that the plasma particles are able to respond quickly enough to neutralise a wave with a frequency less than ω_{pe} such that the wave is damped very quickly over a distance of around k^{-1}, corresponding to the first of the cut-offs, $P = 0$ in (2.5.20). This type of

wave is called an evanescent wave. A wave must therefore have properties such that $\omega \geq \omega_{pe}$, which defines a maximum density for which a light wave can penetrate a plasma. This density is the critical density, n_c:

$$n_c = \frac{\varepsilon_0 m_e}{e^2}\omega^2 \tag{2.5.35}$$

where ω is the frequency of the electromagnetic radiation.

2.6 Wave – particle interactions

Due to the fact that most wave-particle interactions generally only involve the particles with thermal velocities close to the phase velocity of the wave, they cannot be readily described by means of the fluid model detailed in the previous section. Therefore we will revert back to the kinetic model to describe a number of important wave-particle interactions.

An important consequence of the Vlasov equation emanating from plasma kinetic theory is the phenomenon of Landau damping. This is a resonant effect due to particles moving with velocity close to the phase velocity of the waves and causing an exponential decrease in amplitude as a function of time. Landau damping [Landau 1946] can be explained by noting that for $\partial f/\partial u < 0$ there are more particles travelling slightly slower than the wave than there are faster, therefore if the slower particles are accelerated by the wave then the wave loses energy and is damped [Dawson 1961]. Since u is the component of the electron velocity in the direction of propagation of the wave, particles with $u \approx {}^{\omega}/_{k}$ stay roughly in phase with the wave and more efficiently exchange energy with it. In addition to this for particles with $u < {}^{\omega}/_{k}$, upon acceleration, their interaction with the wave is made more resonant and therefore stronger than if they had been decelerated. This means that for particles moving slightly slower than the wave, acceleration is a stronger effect than deceleration; so on average particles gain energy from the wave. In the case where slightly more particles are travelling faster than the wave, the opposite is true and this leads to inverse Landau damping.

A mathematical description of Landau damping is obtained via the treatment by [Landau 1946] [Jackson 1960] who solved the linearized Vlasov equation for $F = -eE$ where the electric field is created when a homogeneous plasma in equilibrium, with distribution function $f_0(\boldsymbol{v})$, is slightly perturbed. In this approach the initial disturbance, $f_1 = (\boldsymbol{r}, \boldsymbol{v}, t)$, is assumed to be in the electron distribution only, so that the ions remain as a steady, homogeneous neutralising background. The distribution function for this process is given by:

$$f(\boldsymbol{r}, \boldsymbol{v}, t) = f_0(\boldsymbol{v}) + f_1(\boldsymbol{r}, \boldsymbol{v}, t) \tag{2.6.1}$$

and (2.6.2) is the linearized Vlasov equation:

$$\frac{\partial f_1}{\partial t} + \mathbf{v} \cdot \frac{\partial f_1}{\partial \boldsymbol{r}} - \frac{e\boldsymbol{E}}{m} \cdot \frac{\partial f_0}{\partial \boldsymbol{v}} = 0 \tag{2.6.2}$$

This methodology results in an equation describing the Landau damping decrement, ω_i:

$$\omega_i = -\left(\frac{\pi}{8}\right)^{1/2} \frac{\omega_{pe}}{(k\lambda_D)^3} \exp\left[\frac{1}{2(k\lambda_D)^2} - \frac{3}{2}\right] \tag{2.6.3}$$

which shows the wave is damped, even in the absence of collisions. Equation (2.6.3) is valid for $k\lambda_D \ll 1$. As $k\lambda_D \to 1$, $|\gamma| \to \omega_{pe}$, that is, the damping time approaches the period of the oscillations, the condition is invoked that the Debye shielding distance is the minimum wavelength for which longitudinal, $\boldsymbol{k} \,//\, \boldsymbol{E}$, oscillations can occur. This is due to the fact that at $k\lambda_D = 1$ the phase speed of the wave is equal to the mean thermal speed of the electrons which are easily able to neutralize the space charge, thus preventing the wave from propagating.

The effect of Landau damping is seen in figures 2.6.1a and 2.6.1b:

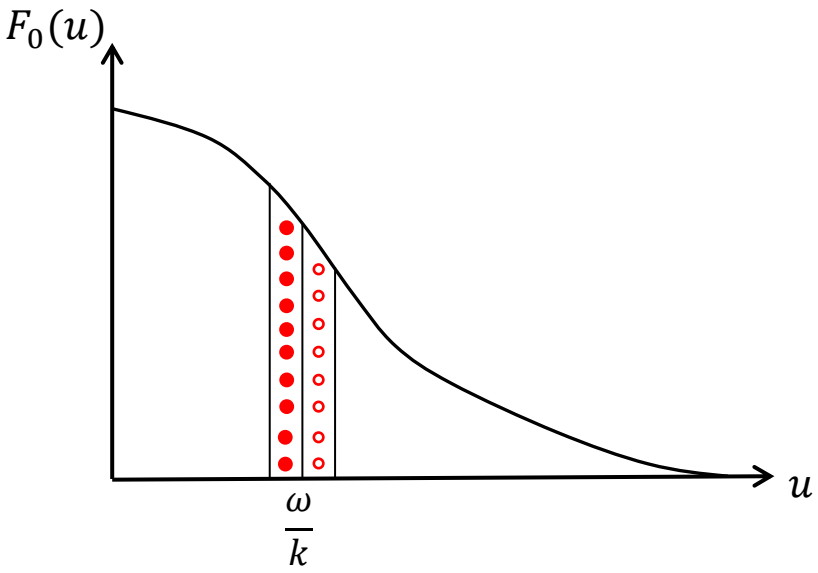

Figure 2.6.1a – Interaction of strongly resonant electrons with wave.

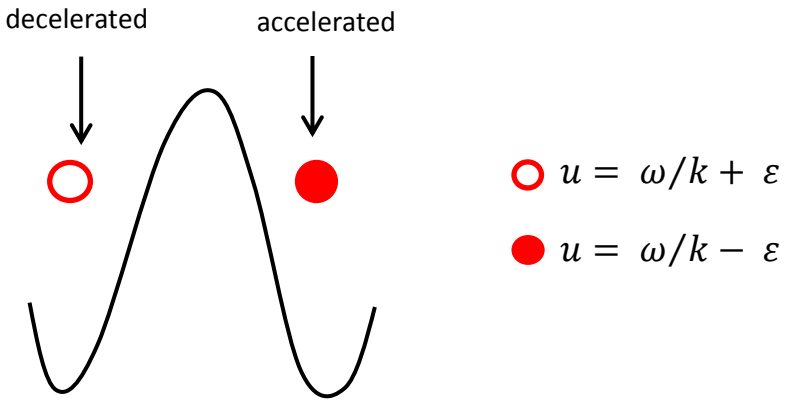

Figure 2.6.1b – Energy transfer profile of strongly resonant electrons with wave.

It can be seen that a negative slope of the distribution function at the resonant speed means that slower particles outnumber the faster particles so that the wave loses more energy and is damped.

Another key wave-particle effect is particle trapping [Chen 1984]. This effect is due to the fact that waves have finite amplitudes, which causes particles with insufficient

energy to surmount the wave peaks to simply oscillate back and forth in the troughs of the waves. An analysis of this begins by considering a single wave with an amplitude that grows/decays very slowly compared with the rate at which it oscillates. Then in a frame of reference moving at the wave phase velocity, $^{\omega}/_{k}$, the particles see a wave profile which is constant and is a function of x only.

The equation of motion of an electron is:

$$\mathrm{m}\ddot{x} = -e\,E(x) = e\,\frac{d\phi(x)}{dx} \tag{2.6.4}$$

where $\phi(x)$ is the electrostatic potential. On integration of (2.6.4) the energy equation is obtained:

$$\frac{1}{2}\mathrm{m}\dot{x}^2 - e\,\phi(x) = E_0 \tag{2.6.5}$$

where E_0 is a constant and is equal to the total energy of the electron. It is observed that if $E_0 > -e\phi(x)$ for all x the kinetic energy is also positive for all x, therefore the electron is untrapped. However, all resonant electrons with values of E_0 below the wave peaks are trapped between the points in the troughs where $E_0 = -e\phi(x)$, this can be seen in figure 2.6.2a and 2.6.2b [Boyd and Sanderson 2003].

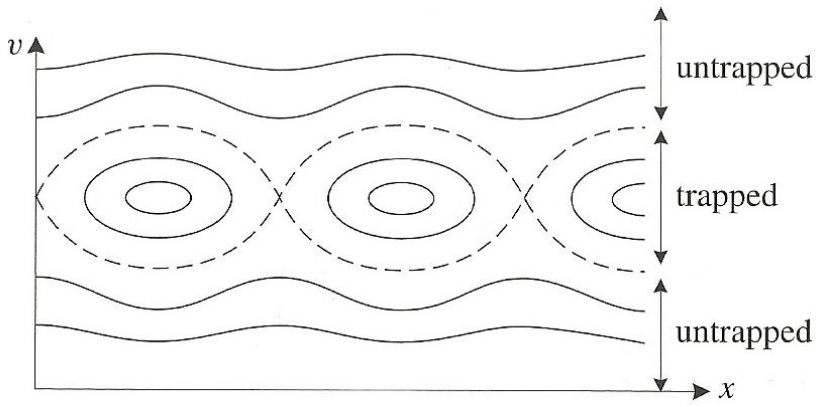

Figure 2.6.2a – Phase space trajectories of trapped particles by finite amplitude waves.

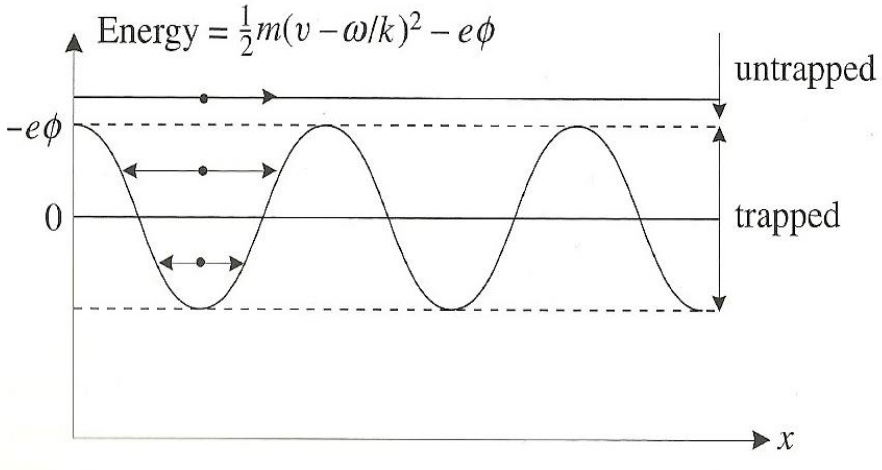

Figure 2.6.2b - Energy diagram for particles trapped by finite amplitude waves.

An important factor contributing to the trapping of particles is plasma wave breaking. It has been shown by linear theory that a small amplitude wave is damped only by particles with a velocity quite near its phase velocity. However, in the case of large amplitude electron plasma waves, the oscillation velocity of an electron in the field can be large enough to bring even an initially cold, main body particle into resonance with the field. At the wave-breaking amplitude, large numbers of formerly non-resonant particles become strongly "trapped". This serves to suddenly damp the wave energy as these slow particles are accelerated by falling into the potential troughs of the wave.

The wave breaking field amplitude $E_{cwb,}$ in the 1-D non-relativistic cold plasma limit, is given by [Dawson 1959]:

$$E_{cwb} = \frac{cm_e\omega_{pe}}{e} \tag{2.6.6}$$

2.7 Wave – wave interactions

One example of a wave-wave interaction is induced scattering in which the resonant particles interact with the beat wave of two plasma waves. The resonance condition for particle trapping where only one wave is involved is:

$$\omega = \boldsymbol{k}.\boldsymbol{v} \tag{2.7.1}$$

To obtain the resonance condition for the case of induced scattering when the scattering occurs between two plasma waves the relevant ω and k for the beat wave are substituted into (2.7.1) to give:

$$\omega_1 - \omega_2 = (\boldsymbol{k_1} - \boldsymbol{k_2}).\underline{v} \tag{2.7.2}$$

where $(\omega_1, \boldsymbol{k_1})$ and $(\omega_2, \boldsymbol{k_2})$ denote the first and second plasma waves, respectively. This process is regarded as induced scattering as the second wave arises due to non-linear interaction with the resonant particles if the first wave is driven with a finite amplitude.

If one wave is propagating through plasma and another natural mode spontaneously arises, resonant linear coupling may give rise to a beat wave. The resonance conditions for this process are:

$$\omega_0 = \omega_1 + \omega_2 \tag{2.7.3}$$

$$\boldsymbol{k_0} = \boldsymbol{k_1} + \boldsymbol{k_2} \tag{2.7.4}$$

If C is the coupling coefficient for the three oscillators, the equations of motion are:

$$\left.\begin{aligned} \ddot{x}_0 + \omega_0^2 x_0 &= -C x_1 x_2 \\ \ddot{x}_1 + \omega_1^2 x_1 &= -C x_0 x_2 \\ \ddot{x}_2 + \omega_2^2 x_2 &= -C x_0 x_1 \end{aligned}\right\} \tag{2.7.5}$$

In the linear approximation the solutions are:

$$x_j = \frac{1}{2}\left(A_j e^{i\omega_j t} + A_j^* e^{-i\omega_j t}\right) \qquad (j = 0, 1, 2) \tag{2.7.6}$$

and if the coupling is weak the non-linear solutions take the form:

$$x_j = \frac{1}{2}\left(A_j(t) e^{i\omega_j t} + A_j^*(t) e^{-i\omega_j t}\right) \tag{2.7.7}$$

Upon substitution of (2.7.7) into (2.7.5):

$$\left(A_0 + 2i\omega_0\dot{A}_0\right) + \left(\dot{A}_0^* - 2i\omega_0 A_0^*\right) e^{-2i\omega_0 t} \tag{2.7.8}$$
$$= -\frac{C}{2}\left(A_1 e^{i\omega_1 t} + A_1^* e^{-i\omega_1 t}\right)\left(A_2 e^{i\omega_2 t} + A_2^* e^{-i\omega_2 t}\right)e^{-i\omega_0 t}$$

which is valid for the first member of (2.7.5). When averaging is performed over the fast time scale, phase mixing gets rid of the second term on the left-hand side and all terms on the right-hand side disappear with exception of the one whose exponent vanishes due to the resonance condition in (2.7.3). This results in the following equations for the first, second and third members of (2.7.5), respectively:

$$\left.\begin{aligned} \dot{A}_0 &= \frac{iC}{4\omega_0} A_1 A_2 \\ \dot{A}_1 &= \frac{iC}{4\omega_1} A_0 A_2^* \\ \dot{A}_2 &= \frac{iC}{4\omega_2} A_0 A_1^* \end{aligned}\right\} \tag{2.7.9}$$

By re-defining the amplitudes such that:

$$a_j = A_j\ \omega_j^{1/2} \tag{2.7.10}$$

We obtain the following set of equations:

$$\left.\begin{aligned} \dot{a}_0 &= iKa_1 a_2 \\ \dot{a}_1 &= iKa_1 a_2^* \\ \dot{a}_2 &= iKa_0 a_1^* \end{aligned}\right\} \tag{2.7.11}$$

where $K = C/4(\omega_0\omega_1\omega_2)^{1/2}$ is the common coupling coefficient [Boyd and Sanderson 2003].

As the waves interact they can exchange energy between themselves, the rates at which this energy is transferred is described by the Manley-Rowe relations [Diamond, Itoh and Itoh 2010], obtained from (2.7.11):

$$-\frac{1}{\omega_0}\frac{d|A_0|^2}{dt} = \frac{1}{\omega_1}\frac{d|A_1|^2}{dt} = \frac{1}{\omega_2}\frac{d|A_2|^2}{dt} \tag{2.7.12}$$

where A denotes the amplitude of each of the waves and the subscripts 0, 1 and 2 relate to the propagating wave, a spontaneously arising natural mode and the beat wave, respectively. An example of where such a process may occur is in the case of laser-driven instabilities such as Raman or Brillouin scattering, arising when a high intensity laser beam passes through a plasma. This interaction creates a physical configuration which is far from thermodynamic equilibrium conditions causing the plasma to respond collectively and unstably, leading to corruption of the coherence of the laser beam and transfer of laser energy to other collective modes of oscillation.

An important consequence of wave-wave coupling and a key factor in the onset of many such instabilities, in particular the interaction of an electromagnetic wave with electron plasma waves, is the ponderomotive force, F_p. This force, resulting from a gradient in field pressure, acts to generate ion density fluctuations which couple the waves together. These fluctuations are a result of the excited plasma wave beating with the light wave to generate variations in the laser field intensity, pushing electrons away from regions of high field intensity to regions of lower field intensity. The force experienced by the electrons is proportional to the gradient of the radiation intensity:

$$\mathrm{F}_p = -\frac{e^2}{4m_e\omega^2}\nabla\langle E^2\rangle \tag{2.7.13}$$

2.8 Modulational instabilities

The ponderomotive force can give rise to a number of instabilities resulting from the migrating electrons. As the electrons move away from areas of high field intensity they drag the plasma ions with them resulting in areas of decreased plasma density. This density depletion is matched by a corresponding amplitude increase where the ponderomotive force causes plasma to be deflected away from this region of increased wave intensity, leading to an augmentation in the density depletion. Thus, causing an initially spatially uniform laser envelope to break up into modulated structures with smaller natural lengths. If modulation of the wave profile continues such that the energy is confined to localised cavitons, typically of a few Debye lengths in size, this leads to wave collapse [Zakharov 1972]. When the modulation of

the wave envelope is in the direction of wave propagation it is referred to as the modulational instability. This modulation of a longitudinal wave is seen in Figure 2.8.1 and can occur for densities less close to critical density.

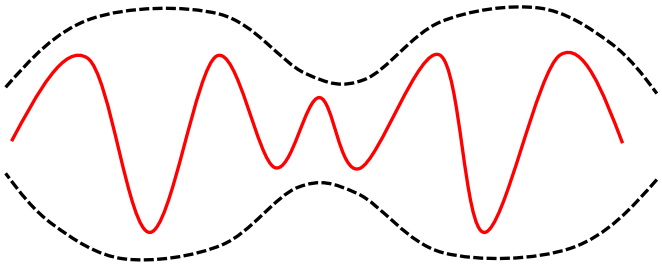

Figure 2.8.1 – Illustration of the modulation of a longitudinal wave due to the ponderomotive force. The wave envelope is seen to be self-modulated along the direction of propagation forming a localised region of lower wave energy.

This effect also applies to transverse waves and can cause a wave to break up into a number of wavelets in a direction transverse to its propagation and is known as the filamentation instability [Chen 1984]. The filamentation instability occurs for low densities all the way up to the critical density but in this case produces an intensity modulation across the laser beam. As the modulations grow the beam breaks into a series of beamlets that become more pronounced as the beam propagates through the plasma towards the critical density. These filaments are as a result of variations in the intensity across the beam where regions of higher intensity push the plasma aside, again due to the ponderomotive force. As a result of this the density is reduced locally and the refractive index of the plasma increases for the regions of higher intensity which bends the wavefronts in such a way that focussing effects are produced that serve to increase the intensity further. Laser beam and electron beam filamentation are important effects in plasma physics as they can be triggered by non-uniformities in the beam. A schematic diagram of this process is seen in figure 2.8.2.

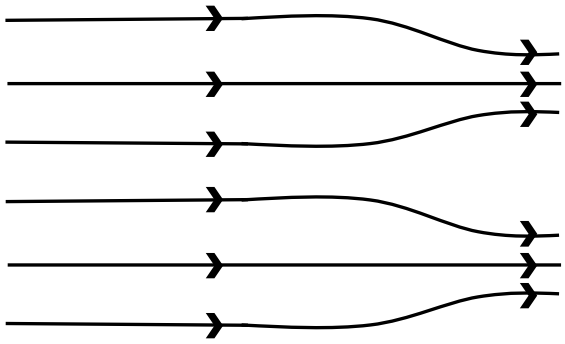

Figure 2.8.2 – Illustration of filamentation of a transverse wave due to the local enhancement of the ponderomotive pressure within the beam. The initially uniform light wave is broken up into a series of small scale filaments orthogonal to its propagation direction.

2.9 Parametric instabilities

A parametric instability occurs as a result of an unstable interaction when a strong electromagnetic pump wave interacts with underdense plasma. Longitudinal plasma waves are driven with frequencies different to the laser carrier frequency and as a result a non-linear interaction between the pump and the density perturbations in the plasma takes place which causes the excitation of electromagnetic sidebands in the EM spectrum. When the interaction is such that the excitation of the electromagnetic sidebands excite or enhance a plasma wave, while the presence of the plasma wave, in turn, enhances the growth of the sidebands then the interaction becomes unstable resulting in one or more parametric instabilities [Rosenbluth 1972] [Drake et al. 1974] [Forslund, Kindel and Lindman 1975].

These instabilities occur due to the fact that large amplitude, transverse, electromagnetic waves, commonly referred to as pump waves, driven through plasma are capable of transferring their energy to two other waves via resonant three-wave coupling. In order for the instability to grow there exists a condition such that the combination of the energy in the pump wave and the strength of the non-linear

coupling is sufficiently large to overcome the damping of the decay waves. This is the threshold condition and is given by:

$$K^2|a_0|^2 > \nu_1\nu_2 \tag{2.9.1}$$

where $K = C/4(\omega_0\omega_1\omega_2)^{1/2}$ and is the coupling coefficient, ν is the linear damping rate, the subscripts 0, 1 and 2 refer to the pump wave and the decay waves, respectively and $a_j = A_j\omega_j{}^{1/2}$ where the subscript j corresponds to waves 0, 1 or 2. The conditions stated previously in (2.7.3) and (2.7.4) represent a case where there is perfect matching, however in practice there is commonly a small frequency mismatch such that:

$$\omega_0 - \omega_1 - \omega_2 = \Delta\omega \tag{2.9.2}$$

where $|\Delta\omega|$ is much smaller than the magnitude of each of the other wave frequencies.

Equation (2.9.1) can then be extended to determine the increase in pump energy required to overcome the frequency mismatch:

$$K^2|a_0|^2 = \nu_1\nu_2 + \frac{\nu_1\nu_2(\Delta\omega)^2}{(\nu_1+\nu_2)^2} \tag{2.9.3}$$

A mismatch in the wavenumber as opposed to the frequency has a similar effect by reducing the growth rate and increasing the instability threshold [Liu, Rosenbluth and White 1974].

In laser produced plasmas the plasma is typically highly inhomogeneous so the waves will exhibit dispersion, hence changing the relationship between ω and k as the waves propagate through the plasma. The resonance conditions for the interaction will therefore only be satisfied in restricted areas of the interaction, hence limiting the region where the instability can occur.

In unmagnetised plasmas, where $T_e \gg T_i$, three wave coupling can occur between various combinations of the electromagnetic pump wave $(\omega_0, \boldsymbol{k}_0)$, the longitudinal electrostatic Langmuir wave $(\omega_L, \boldsymbol{k}_L)$ and the longitudinal, ion acoustic wave $(\omega_S, \boldsymbol{k}_S)$. The dispersion equations for these waves are given by (2.9.4), (2.9.5) and (2.9.6), respectively:

$$\omega_0^2 = \omega_T^2 = \omega_{pe}^2 + \boldsymbol{k}_T^2 c^2 \quad (2.9.4)$$

$$\omega_L^2 = \omega_{pe}^2 + \boldsymbol{k}_L^2 v_e^2 \quad (2.9.5)$$

$$\omega_s^2 = \boldsymbol{k}_s^2 c_s^2 \quad (2.9.6)$$

where $c_s = \sqrt{ZT_e/m_i}$ is the ion acoustic speed and $v_e = \sqrt{3kT/m_e}$ is the electron thermal speed. The dispersion relations for these waves are plotted in figure 2.9.1.

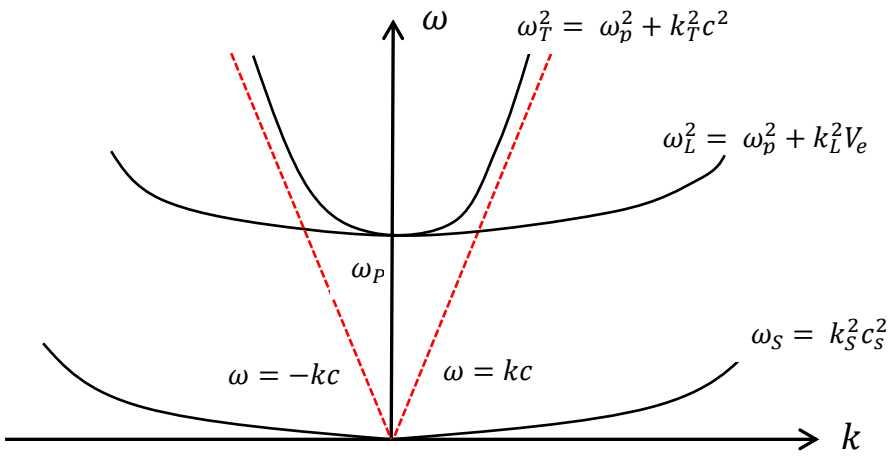

Figure 2.9.1 – Dispersion plot for the transverse electromagnetic, Langmuir and ion acoustic waves sketched with reference to the speed of light, plotted in red. The cut-off frequency for the low frequency scattered wave is seen to be 0 and the cut-off frequency for the transverse and scattered waves is seen to be equal to the plasma frequency.

The saturation of these parametric instabilities can be as a result of one or more of the following processes:

■ wavenumber mismatch resulting from plasma inhomogeneity.

■ decay of the daughter waves leading to a cascade of modes.

■ particle trapping as the electrostatic decay waves achieve large amplitude.

■ depletion of the pump wave to below the threshold intensity.

Two examples of parametric instabilities are stimulated Brillouin scattering and stimulated Raman scattering which are both three wave scattering instabilities. The type of parametric instability is classified according to the relation between the phase velocity of the plasma wave and the electron and ion thermal velocities, $v_{th,e}$ and $v_{th,i}$. When the incident pump scatters off a Langmuir wave ($v_{ph} \gg v_{th,e}$, so the electrons are adiabatic and the ions immobile) the instability is called stimulated Raman Scattering and if the pump scatters off an ion-acoustic wave ($v_{th,i} \ll v_{ph} \ll v_{th,e}$, so the electrons are isothermal and the ions adiabatic) it is called stimulated Brillouin scattering. The scattering exhibited from these modes comes in a variety of different forms depending on the propagation direction of the scattered wave. In the following analysis we restrict our discussion to transverse waves propagating backwards with respect to the pump wave, giving rise to the names Brillouin/Raman backward scattering.

2.9.1 Stimulated Brillouin back scattering

At a classical level stimulated Brillouin scattering is best understood by the combination of two processes:

i) The laser beam reflecting off of the density variation, which is part of an ion-acoustic wave and,

ii) the reflected electromagnetic wave beating with the laser beam to drive up the ion-acoustic wave.

Physically this process can be described as the scattering of a high frequency transverse wave by a low frequency ion-acoustic wave into a different transverse wave and its influence is easily described by considering the effect of a large amplitude laser beam on a plasma. Firstly, the electrons in the plasma oscillate in the electromagnetic fields and each electron re-radiates electromagnetic dipole radiation. (In the case of a plasma with perfect uniformity, the electrons oscillate with a phase

such that their re-radiation adds up in phase only in the direction of the laser beam). This causes the phase velocity of the laser beam to be slightly greater than the speed of light. However, if the case where the plasma supports a sound wave propagating parallel to the laser beam is considered, the variation in the density of the re-radiating dipoles results in the re-emitted dipole radiation not cancelling out in other directions, thus, causing an electromagnetic wave to be produced and propagate in the reverse direction. The counter-propagating electromagnetic wave then beats with the laser beam and sets up a standing wave, moving slowly at the speed of sound. Plasma is pushed towards the nodes in the standing wave via the ponderomotive force and if the phase of the force is appropriate the amplitude of the ion-acoustic wave, with which the process started, is increased. This mechanism is cyclic and cumulative in nature; the laser beam interacts with the ion-acoustic wave to generate the reverse electromagnetic wave, which then interacts with the laser beam causing the ion-acoustic wave to grow leading to an increase in the amplitude of the reverse electromagnetic wave. As a result of this cycle exponential growth in the amplitude of both the ion-acoustic and reverse electromagnetic waves occurs [Dendy 1993].

An analysis of stimulated Brillouin scattering follows directly from linear theory where the electrons are described as a warm fluid. The resonance conditions stated in (2.7.3) and (2.7.4), where $(\omega_1, \boldsymbol{k}_1)$ denote the scattered wave values and $(\omega_2, \boldsymbol{k}_2)$ represent the ion acoustic wave properties, also apply to this instability. In order to obtain the coupled equations describing the Brillouin instability, the response of an initially uniform plasma driven by a large amplitude light wave is considered. As the density fluctuation for the Brillouin instability is the low frequency fluctuation associated with the ion acoustic wave, both electron and ion motion must be included in this description. This is attributed to the fact that the thermal speed of the ions is comparable to that of the ion acoustic wave. The coupled equations describing SBS in homogenous plasma are therefore [Forslund, Kindel and Lindman 1975]:

$$\left[\frac{d^2}{dt^2} - c^2\nabla^2 + \omega_0^2\right]\boldsymbol{v_1} = -\frac{e^2}{m\epsilon_0} n_e \boldsymbol{v_0} \qquad (2.9.1.1)$$

$$\left[\frac{d^2}{dt^2} - c_s^2\nabla^2 + \omega_0^2\right] n_i = n_0\nabla^2(\boldsymbol{v_0} \cdot \boldsymbol{v_1}) \qquad (2.9.1.2)$$

From the coupled wave equations the dispersion relation describing SBS is obtained:

$$(\omega_2^2 - k_2^2 c_s^2)(\omega_2^2 - 2\omega_2\omega_0 + 2k_0 \cdot k_2 c^2 - {k_2}^2 c^2) = \frac{k_2^2 v_{os}^2}{4}\omega_{pi}^2 \qquad (2.9.1.3)$$

Following directly from this the Brillouin scattering growth rate, in the weakly coupled regime, is given by:

$$\gamma_B = \frac{1}{8}\frac{v_{osc}^2}{v_e^2}\frac{\omega_{pe}^2}{\omega_0}\frac{k_0 c_s}{(\gamma_s + \gamma_T)} \qquad (2.9.1.4)$$

As the Brillouin decay waves may undergo collisional damping in addition to Landau damping, a threshold for the onset of the instability when the wave is collisionally damped is invoked. This instability threshold takes the form:

$$\left(\frac{v_{osc}}{v_e}\right)^2 \geq 4\frac{\nu_{ei}}{\omega_0}\frac{\gamma_i}{k_0 c_s} \qquad (2.9.1.5)$$

such that (2.9.3) must be satisfied for the instability to be excited and subsequently grow in the weakly coupled regime, where γ_s is the landau damping decrement, γ_T is the transverse wave damping term, ν_{ei} is the electron-ion collision frequency and v_e is the electron thermal velocity.

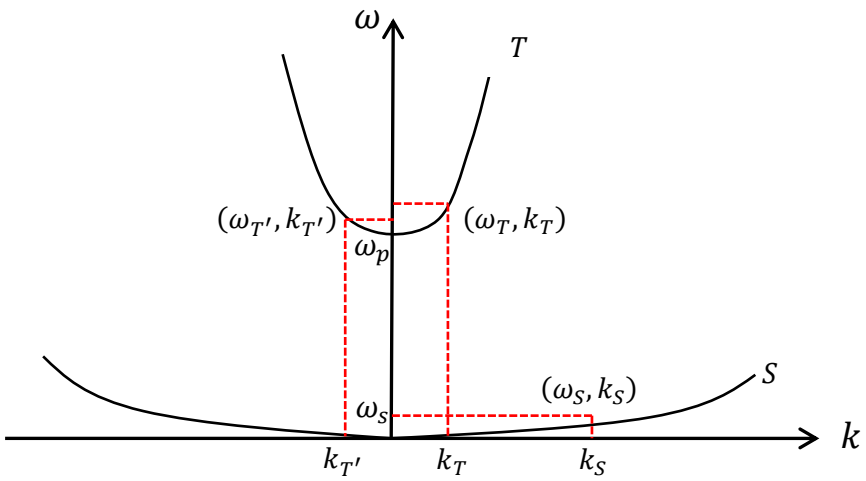

Figure 2.9.1.1 – Frequencies and wavenumbers for stimulated Brillouin scattering illustrating the three wave decay process consisting of two transverse waves and an ion acoustic wave. The red dotted lines indicate the small frequency shift between the two transverse waves as a result of energy being transferred to the ion acoustic wave during the scattering process.

Figure 2.9.1.1 details the dispersion characteristics for Brillouin scattering, such that $T \rightarrow T' + S$, where it can be seen that the minimum frequency shift is equal to zero. This allows the scattering process to operate at densities up to the critical density. As the frequency of the ion acoustic wave is much less than the pump laser frequency this allows nearly all the pump energy to be transferred to the scattered light wave.

2.9.2 Stimulated Raman back scattering

The Raman scattering process in many ways is very similar to that of Brillouin scattering in so far as it is a 1-D parametric instability. However, the most significant difference between these modes is that the scattering of the high frequency transverse wave in Raman scattering is via a Langmuir wave and not an ion acoustic wave as is the case for Brillouin scattering.

An analysis of stimulated Raman scattering is performed in a similar way to SBS where the resonance conditions stated in (2.7.3) and (2.7.4) also apply, but in this case (ω_2, k_2) represent the Langmuir wave properties. Stimulated Raman scattering (SRS) in a plasma can also be described by conducting a first-order perturbation analysis of the electron fluid equations (2.5.7) – (2.5.12) where in this case the ion motion can be neglected as they are assumed to be immobile. This is due to the fact that the heavy, slow moving ions cannot keep up with the fast moving Langmuir wave. This approach leads to a pair of coupled equations describing SRS in homogenous plasma consisting of (2.9.1.1) and a modified version of (2.9.1.2):

$$\left[\frac{d^2}{dt^2} - 3v_e^2\nabla^2 + \omega_0^2\right] n_e = n_0\nabla^2\left(\underline{v}_0 \cdot \underline{v}_1\right) \tag{2.9.2.1}$$

where $\partial \underline{v}_1/\partial t = -eE_s/m$, the subscripts 0 and 1 denote the pump wave and the scattered wave components, respectively.

Fourier analysis of (2.9.1.1) and (2.9.2.1) yields the dispersion relation for Raman scattering:

$$(\omega_2^2 - \omega_0^2 - 3k^2v_e^2)(\omega_1^2 - \omega_0^2 - k_1^2c^2) = k^2v_0^2\omega_0^2 \tag{2.9.2.2}$$

The Raman growth rate is given by [Trines 2011]:

$$\gamma_B = \frac{1}{4}\frac{\omega_0\omega_{pe}}{(\gamma_T + \gamma_L)}\frac{v_{osc}^2}{c^2} \tag{2.9.2.3}$$

Here, $a_0 = 8.55x10^{-10}\sqrt{I_0\lambda^2(Wcm^{-2}\mu m^2)}$ denotes the dimensionless, scaled field amplitude and I_0 is the peak intensity of the laser beam (pump or probe) under consideration. In the case where the phase matching conditions are not exactly satisfied the growth rate of the instability is slower.

When collisional damping of the decay waves is accounted for this introduces a threshold for the onset of the instability which is given by [Kruer 2003]:

$$\left(\frac{v_{osc}}{c}\right)^2 > \left(\frac{\omega_{pe}}{\omega_0}\right)^2\frac{\nu_{ei}^2}{\omega_0\omega_{pe}} \tag{2.9.2.4}$$

As the minimum frequency shift which can occur for Raman scattering is equal to the plasma frequency, it is clear that the instability requires that $\omega_0 \gtrsim 2\omega_{pe}$ i.e.

$n \lesssim n_{cr}/4$, where n is the plasma density. This means that the maximum density where Raman amplification techniques can be utilised is one quarter critical density. In addition to this, less energy can be transferred into the scattered wave via Raman scattering than for Brillouin scattering as less energy is coupled into the ion acoustic wave in SBS than the Langmuir wave associated with SRS. The dispersion for stimulated Raman scattering can be seen from figure 2.9.2.1 where the scattering observed is of the form $T \rightarrow T' + S$.

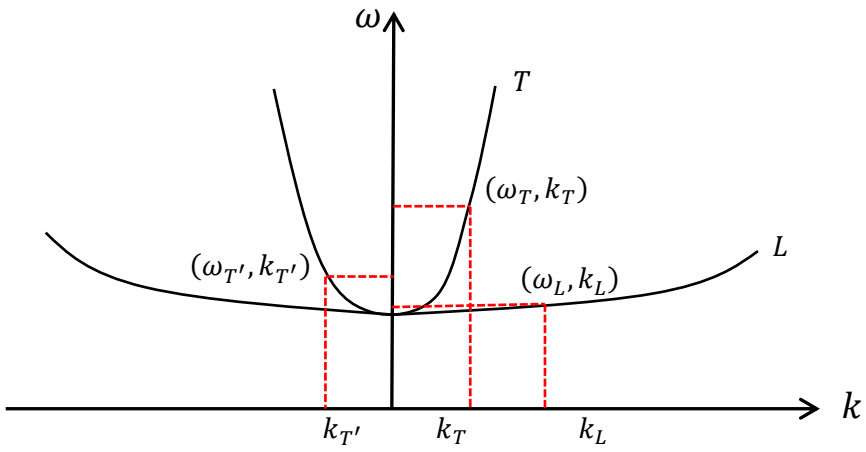

Figure 2.9.2.1 – Frequencies and wavenumbers for stimulated Raman scattering illustrating the three wave decay process consisting of two transverse waves and a Langmuir wave. The red dotted lines indicate the frequency shift between the two transverse waves as a result of energy being transferred to the plasma wave during the scattering process.

References

Akhiezer A. I. and Polovin R. V. Sov. Phys. JETP 3, 696 (1956)

Allen J. E. and Phelps A. D. R. *Waves and microinstabilities in plasmas-linear effects*. Reports on Progress in Physics, 40, 1305-1368 (1977)

Bohm D. *The Characteristics of Electrical Discharges in Magnetic Fields*. McGraw-Hill (1949)

Boyd T. J. M. and Sanderson J. J. *The Physics of Plasmas*. Cambridge University Press (2003)

Bingham R. *Non-Linear Laser-Plasma Interactions*. D. Phil Thesis, University of Oxford (1977)

Bret A., Firpo M. C. and Deutsch C. *Characterization of the Initial Filamentation of a Relativistic Electron Beam Passing through a Plasma*. Physical Review Letters 94, 115002 (2005)

Chen, F. F. *Introduction to plasma physics and controlled fusion*. *Volume 1:Plasma Physics.* Plenum press (1984)

Clemmow, P. C. and Dougherty J. P. *Electrodynamics of particles and plasmas.* Addison-Wesley Pub. Co. (1969)

Cook D. *The Theory of the Electromagnetic Field*. Prentice-Hall (1975)

Dawson J. M. *Nonlinear electron oscillations in a cold plasma*. Physical Review, 113, 383-387 (1959)

Dawson J. *On Landau Damping*. The Physics of Fluids, 4, 869 (1961)

Dendy R. O. *Plasma Dynamics*. Oxford University Press (1990)

Dendy R. O. *Plasma Physics: An introductory course*. Cambridge University Press (1993)

Diamond P. H., Itoh E. and Itoh K. *Modern Plasma Physics Volume 1: Physical Kinetics of Turbulent Plasmas.* Cambridge University Press (2010)

Diver D. A. *A Plasma Formulary for Physics, Technology, and Astrophysics*. WILEY-VCH (2001)

Dobbs E. R. *Electromagnetic Waves*. Routledge & Kegan Paul (1985)

Drake F., Kaw P. K., Lee Y. C., Schmid G., Liu C. S. and Rosenbluth M. N. *Parametric instabilities of electromagnetic waves in plasmas*. Physics of Fluids 17, 778 (1974)

Forslund D. W., Kindel J. M. and Lindman E. L. *Theory of stimulated scattering processes in laser-irradiated plasmas*. The Physics of Fluids, vol. 18, no. 8 (1975)

Grant I. S. and Phillips W. R. *Electromagnetism*. Wiley (1990)

Gurnett D. A. and Bhattacharjee A. *Introduction to plasma physics: with space and laboratory applications*. Cambridge University Press (2005)

Inan U. S. and Gołkowski M. *Principles of Plasma Physics for Engineers and Scientists.* Cambridge University Press (2010)

Jackson J. D. *Longitudinal plasma oscillations*. Journal of Nuclear Energy. Part C, Plasma Physics, Accelerators, Thermonuclear Research, 1, 17 (1960)

Krasovitskiy V. B. *Instabilities of Relativistic Electron Beam in Plasma*. Nova Science Publishers (2008)

Kruer W. L. *The Physics of Laser Plasma Interactions*. Westview Press (2003)

Landau L. D. Journal of Physics. (U.S.S.R), 10, 25 (1946)

Lee R. and Lampe M. *Electromagnetic Instabilities, Filamentation, and Focusing of Relastivistic Electron Beams*. Physical Review Letters, 31, 1390–1393 (1973)

Liu C. S., Rosenbluth M. N and White R. B. *Raman and Brillouin scattering of electromagnetic waves in inhomogeneous plasmas*. Physics of Fluids 17, 1211 (1974)

Lorrain P., Corson D. P. and Lorrain F. *Electromagnetic fields and waves.* Freeman (1988)

Melrose D. B. *Instabilities in Space and Laboratory Plasmas*. Cambridge University Press (1989)

Pozar D. M. *Microwave Engineering*. John Wiley & Sons (2005)

Stix T. H. *Waves in Plasmas*. American Institute of Physics (1992)

Stringer T. E. *Low Frequency Waves in an Unbounded Plasma*. Plasma Physics (Journal of Nuclear Energy Part C), 5, pp.89-107 (1963)

Rosenbluth M. N. *Parametric Instabilities in Inhomogenous Media*. Physical Review Letters, vol. 29, no. 9 (1972)

Thompson W. B. *An Introduction to Plasma Physics*. Pegamon Press Ltd., 1962

Tonks L. and Langmuir I. *A General Theory of the Plasma of an Arc.* Physical Review, 34, 876–922 (1929)

Trines R. M. G. M., Fiuza F., Bingham R., Fonseca R. A., Silva L. O., Cairns R. A. and P. A. Norreys. *Simulations of efficient Raman amplification into the multipetawatt regime*. Nature Physics, 7, 87 (2011)

Weibel E. S. *Spontaneously Growing Transverse Waves in a Plasma due to an Anisotropic Velocity Distribution*. Physical Review Letters, vol.2, no.3 (1958)

Zakharov, V. E. Sov. Phys. JETP 35, 908 (1972)

Chapter 3

Numerical Techniques: OSIRIS Particle-in-Cell Code

The simulations presented in chapters 4, 5 and 6 were performed using a 1-D version of OSIRIS 2.0. This code is a 3-D particle-in-cell (PiC) code developed by the OSIRIS Consortium, consisting of the University of California (Los Angeles) and the Instituto Superior Técnico (Lisbon, Portugal). The OSIRIS framework consists of OSIRIS and visXD, a visualisation infrastructure used for data analysis developed to post-process the scalar and vector results from PiC calculations. The code was designed for scientific applications primarily concerning the study of high intensity beam-plasma interactions. A recent version of OSIRIS may be obtained only by collaboration with either of the research groups above and publication of data obtained as a direct result of use of the code is permitted provided Ref. [Fonseca et al.. 2002] is cited.

In this chapter an overview of the operation of this PiC code and the key physics used to numerically diagnose the behaviour associated with complex systems with many degrees of freedom are presented along with the benchmarks used to validate OSIRIS' results.

3.1 Description of the code

OSIRIS is a fully parallelized, fully implicit, fully relativistic, and fully object-oriented PiC code for modelling intense beam-plasma interactions. Algorithms are

present which allow for 2-D and 3-D simulations requiring the use of Cartesian co-ordinate systems and 2-D simulations using azimuthally symmetric cylindrical co-ordinates, each of which having velocity components in all three directions. The code is written in Fortran 90 and written in such a way that it is largely independent from the dimensionality of the co-ordinate system used.

It supports a variety of boundary conditions such as reflective, absorbing and thermal bath boundaries for the particles and conducting and Lindman open-space boundaries for the fields. In addition to this, periodic boundary conditions are also implemented for the particles and fields and moving window options are configured for simulations requiring a large interaction length.

Due to the highly non-linear and kinetic processes that occur during high intensity laser-plasma interactions the plasma kinetic model is incorporated into the code, in order to provide the most complete plasma description possible. This model is based on the particle in cell (PiC) algorithm, both in the electrostatic and electromagnetic limits.

As the software is required to compute real systems containing an extremely large number of particles, macroparticles are used in order to make simulation of these systems possible. A macroparticle is a computational particle representative of a collection of real particles containing a large number of ions and electrons. The method of introducing macroparticles is very effective due to the fact the Lorentz force (2.3.4) depends only on the charge to mass ratio allowing a computational particle to follow the same trajectory as a real particle.

As it is too time-consuming to calculate inter-particular forces directly, a mathematical mesh across the length of the plasma, typically of rectangular shape, is introduced upon which the fields are calculated. The electromagnetic fields are known only on the mesh points themselves but the particles are free to move with respect to the mesh. The space bounded by adjacent grid points is termed a cell. The fields are calculated from the charge and current densities which are obtained by distributing the charge and current of each particle over the points that define the cell in which the particle resides, hence the name particle-in-cell. The computational grid

serves not only to significantly reduce the simulation run time but inter-particular forces at lengths of less than a grid cell are smoothed away. Therefore, as two simulation particles approach zero separation the force between them goes to zero instead of infinity, avoiding Coulomb singularities. Effectively the grid gives the particles a finite size, reducing short range forces which would otherwise be artificially enhanced by the small numbers of simulation parameters.

3.2 Fields

The OSIRIS plasma simulation framework utilises a finite difference solver which is used to solve the electromagnetic fields locally, in both space and time, from the charge and current densities calculated by weighting discrete particles on to the grid. This is performed via the time-dependent Maxwell's equations [Pozar 2005]:

$$\frac{d}{dt}\int \underline{D}\cdot d\underline{S} = \oint \underline{H}\cdot d\underline{l} - \int \underline{J}\cdot d\underline{S} \tag{3.2.1}$$

$$\frac{d}{dt}\int \underline{B}\cdot d\underline{S} = -\oint \underline{E}\cdot d\underline{l} \tag{3.2.2}$$

where the line integrals are along the cell sides and the surface integrals are across the cell faces. This technique is based on the standard Yee cell algorithm, a second order leap-frog algorithm, which uses edge point elements and midpoint evaluation of fields in both time and space where the midpoint evaluation is achieved by offsetting the grid for the magnetic field by half a division from the grid of the magnetic field. The Yee cell gives an exact representation of the integrated form of Maxwell's equations when the average value of a field component over the face of the square through which it passes is equal to its average value along the edge for which it is defined [Yee 1966].

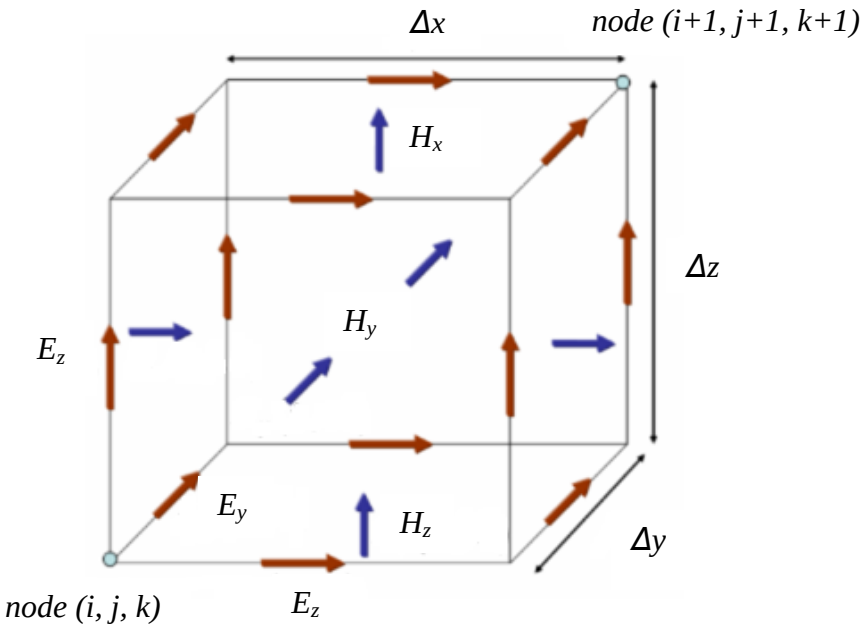

Figure 3.2.1 – Yee cell geometry and field components

The projection of charges and currents on the grid are done in such a way that the continuity equation:

$$\frac{d\rho}{dt} + \underline{\nabla} \cdot \underline{J} = 0 \tag{3.2.3}$$

is satisfied at all times. The following equations are then satisfied by default:

$$\frac{d}{dt}(\nabla \cdot B) = 0 \tag{3.2.4}$$

$$\frac{d}{dt}(\underline{\nabla} \cdot \underline{D} - \rho) = 0 \tag{3.2.5}$$

By setting the initial conditions of the simulations such that $B = E = 0$ and $\rho = 0$ the conditions given by equations (2.5.1 – 2.5.2) are satisfied throughout the duration of the calculation [Trines 2003].

The fields are then advanced in time as follows:

i) The electric field is advanced by $\frac{dt}{2}$ and calculated using (3.2.2),

ii) The magnetic field is advanced by dt and calculated using (3.2.1),

iii) The electric field is advanced by another timestep, $\frac{dt}{2}$, and updated.

This leap-frog scheme ensures that the electric and magnetic fields are diagnosed at the same time-step and not at alternating times.

3.3 Particles

The particle motion is diagnosed from two discrete first-order differential equations, again using a second order leap-frog algorithm, which are integrated separately for each particle:

$$m\frac{dv}{dt} = F \tag{3.3.1}$$

$$\frac{dx}{dt} = v \tag{3.3.2}$$

These equations of motion are replaced by the finite-difference equations:

$$m\frac{v_{new} - v_{old}}{\Delta t} = F_{old} \tag{3.3.3}$$

$$\frac{x_{new} - x_{old}}{\Delta t} = v_{new} \tag{3.3.4}$$

Where the Lorentz force, (2.3.4), is calculated at the particle. Each individual particle is pushed to a new position and momentum via self-consistently calculated fields, therefore the code makes no physics approximations, to the extent that quantum mechanical effects can be neglected.

The particles are pushed as follows:

i) The electric field accelerates the particle over $\frac{dt}{2}$.

ii) The particle velocity is rotated by the magnetic field (but does not change in magnitude) through Boris' algorithm [Birdsall and Langdon 1991].

iii) The particle is once again accelerated by the electric field over $\frac{dt}{2}$.

The computer advances v_t and x_t to $v_{t+\Delta t}$, $x_{t+\Delta t}$ and updates the particle positions and momenta, even although x and t are not known at the same instant in time. This method of leap-frog integration in time and space is seen in Figure 3.3.1

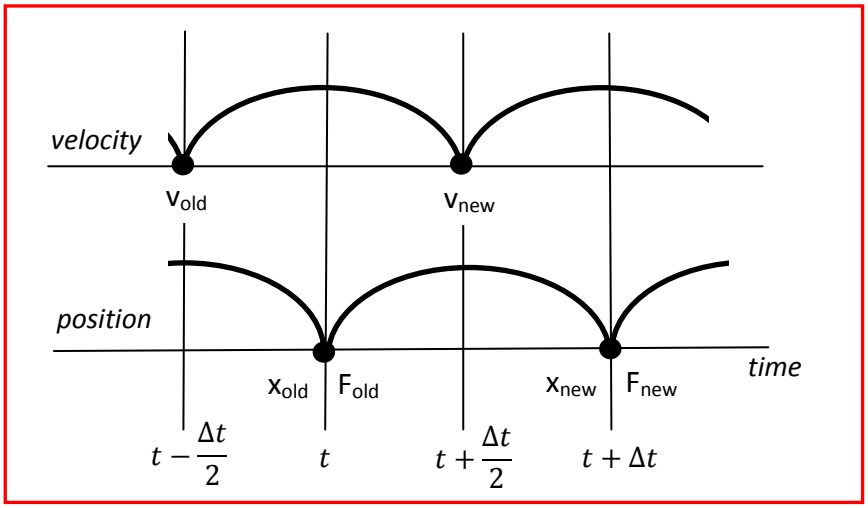

Figure 3.3.1 – Schematic diagram of the leap-frog integration method demonstrating the half-cell offset between the evaluation of the velocity and position. The time between the points marked by t and $t + \Delta t$ indicates one complete time step over which the particles have traversed one grid cell.

In order to obtain the charge and current density the charge and current of each individual particle requires to be projected onto the mesh. This is done by performing weighting calculations which involves interpolation among the grid points nearest to where the particle resides.

3.4 PiC code flow

The flow of operations conducted within a single time step in OSIRIS closely follows the cycle of a typical PiC code. The process begins with carefully chosen

initial conditions of the velocities and positions of the particles at $t = 0$ and execution of the diagnostic routines selected. The particles are then pushed using the updated values for the fields and the current is deposited and smoothed. The code then updates the boundaries for particles and currents. Finally the new values of the electric and magnetic fields are calculated and the boundaries are updated. This loop is repeated until the computer has performed all of the required timesteps. A schematic of this process is seen in Figure 3.4.1.

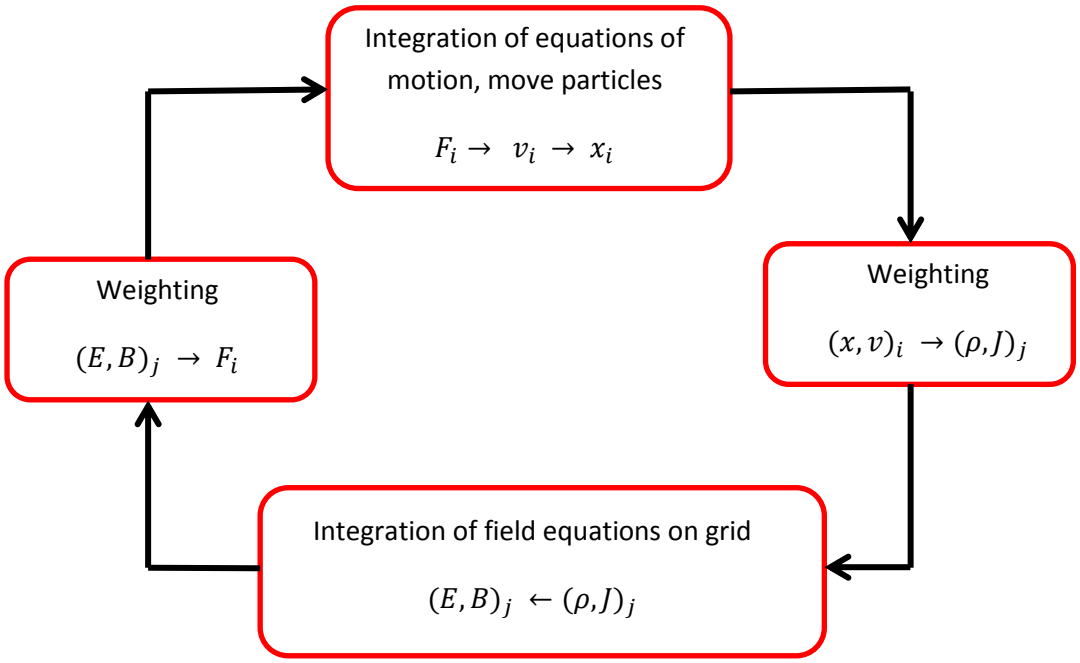

Figure 3.4.1 – Schematic of a typical simulation loop in a particle code.

Where the subscripts i and j denote the particle name and a discrete point in space, respectively.

3.5 Conditions for stability

When using the finite difference time domain method to perform computational calculations, care must be taken when calculating the cell size, Δx and the time step for integration, Δt.

According to the Nyquist sampling theorem:

$$\lambda = 2\Delta x \tag{3.5.1}$$

There must be at least two samples per spatial period in order for the spatial information to be accurately sampled. However in PiC simulations as the sampling is not exact and the smallest wavelength is not precisely determined, more than two grid cells per wavelength are required. For the simulations performed in this thesis a standard of at least ten grid cells per wavelength has been adopted for the highest frequency (shortest wavelength) of interest in each case. This also serves to reduce the numerical dispersion errors inherent in FDTD calculations due to different frequencies travelling across the grid at slightly different speeds [Taflove 1995].

After determining the cell size the length of each timestep immediately follows from the Courant–Friedrichs–Lewy condition. This condition states that no waves or particles may traverse more than one grid cell in any single time step. Violation of this condition leads to inaccuracies in the solutions of the partial differential equations [Kunz and Leubers 1993]. For a grid cell with dimension Δx in all directions, with the maximum velocity of propagation of any wave/particle being c, the speed of light in free space, then:

$$c\Delta \mathrm{t} \leq \frac{\Delta x}{\sqrt{d}} \tag{3.5.2}$$

for stability. Where d is the dimensionality of the grid ($d = 1, 2, or\ 3$).

For a 3-D grid this becomes:

$$c\Delta \mathrm{t} \leq 1 \Big/ \sqrt{\frac{1}{(\Delta x)^2} + \frac{1}{(\Delta y)^2} + \frac{1}{(\Delta z)^2}} \tag{3.5.3}$$

When this equality is upheld the discretised wave most closely approximates the actual wave propagation and grid dispersion errors are minimized.

3.6 Code benchmarking

A number of benchmarks have been conducted on OSIRIS to determine the reliability of the results obtained through its calculations. In 2010 a detailed comparative study was conducted to assess the variations in results between OSIRIS and Vorpal [Neiter and Cary 2004], another well-established particle-in-cell code. This benchmarking process concluded that there were no significant differences between the codes and that the outputs from each were very closely correlated for all values of laser field amplitudes tested [Paul et al. 2008].

For specific benchmarks relating to the SBS results presented in this thesis please refer to Chapters 4, 5 and 6 for numerical, theoretical and experimental benchmarks, respectively.

References

Birdsall, C. K. and Langdon, A. B. *Plasma Physics via Computer Simulation*. Adam Hilger (1991)

Fonseca, R. A., Silva, L. O., Tsung, F. S., Decyk, V. K., Lu, W., Ren, C., Mori, W. B., Deng, S., Lee, S., Katsouleas, T. and Adam, J. C. *High Performance Computing in Particle Accelerator Science and Technology - OSIRIS: A Three-Dimensional, Fully Relativistic Particle in Cell Code for Modeling Plasma Based Accelerators*. Lecture notes in computer science, 2331, 342-351 (2002)

Kunz, K. S. and Leubers, R. J. *The finite difference time domain method for electromagnetics*. CRC Press (1993)

Neiter, C. and Cary, J. R. *VORPAL: a versatile plasma simulation code*. Journal of Computational Physics, 196, 448-472 (2004)

Paul, K., Huang, C., Bruhwiler, D. L., Mori, W. B., Tsung, F. D., Cormier-Michel, E., Guddes, C. G. R., Cowan, B., Cary, J. R., Esarey, E., Fonseca, R. A., Martins, S. F. and Silva, L. O. *Benchmarking the codes VORPAL, OSIRIS, and QuickPIC with Laser Wakefield Acceleration Simulations*. 13th Advanced Accelerator Concepts Workshop, Santa Cruz, CA (2008)

Pozar, D. M. *Microwave Engineering*. John Wiley & Sons (2005)

Taflove, A. *Computational Electrodynamics: The Finite-Difference Time-Domain Method*. Artech House (1995)

Trines, R. M. G. M. *Generation of Highly Energetic Electrons in Laser-Plasma Wakefields*. PhD Thesis, Technische Universiteit Eindhoven (2003)

Yee, K. S. *Numerical Solution of Initial Boundary Value Problems Involving Maxwell's Equations in Isotropic Media*. IEEE Antennas and Propagation Society 14, 302 (1966)

Chapter 4

Damping effects on amplification of laser beams by SBS

In this chapter we report on numerical simulations of energy transfer between a laser pump beam and a counter-propagating seed beam using the Brillouin scattering process in uniform plasma. A comparison is made between collisionless and collisional plasma configurations via particle-in-cell simulations. As collisions are a relatively new addition to many numerical codes there is no existing published work in this area relating to SBS.

Due to the relatively high densities required for adequate levels of Brillouin scattering to be achieved, typically above one quarter of the critical density, it is anticipated that collisions will play a significant role in this energy transfer process. In practise both the naturally occurring Brillouin scattering by the pump wave and the driven beat process, when a seed is introduced, will occur at the same time. It would therefore be advantageous to control the naturally occurring process that can destroy the efficiency of the energy transfer.

4.1 PiC simulation setup

The energy transfer between two counter-propagating laser pulses was simulated numerically in 1D using the fully relativistic OSIRIS particle-in-cell code, as detailed in chapter 3, and was constructed as follows. A pump laser of intensity 10^{16} Wcm^{-2} corresponding to a laser wavelength of 1μm was injected in to a plasma column of

length $650c/\omega_0$, where ω_0 is laser frequency, with the realistic mass ratio for ions to electrons of $m_i/m_e = 1836$ used. The plasma temperature ratio of $ZT_e/T_i = 50$ where $Z = 1$, for a hydrogen plasma, and $T_e = 500eV$ was chosen in order to render Landau damping of the IAW negligible. In all cases discussed in this chapter the density was chosen slightly above the quarter critical level at $0.3n_c$ in order to mitigate mode competition from Raman scattering. The seed pulse, of intensity 10^{15} Wcm^{-2} and a full width at half maximum (FWHM) of 100ps with a $\sin^2$ shape, was launched at the instant the pump pulse had traversed the length of the plasma. A frequency mismatch between the pump and seed laser pulses was also introduced, with the seed pulse frequency being downshifted by an amount equal to the ion acoustic frequency. The pulses are counter propagating through the plasma with the pump pulse travelling from right to left through the simulation box. The time step for integration is $\Delta t = 0.04\omega_0^{-1}$ and the spatial resolution of the simulations is of the order of the Debye length with 100 particles per cell. In the simulations where collisional processes were included these were calculated self-consistently by OSIRIS for a reference plasma density of $3x10^{20}$ cm^{-3} corresponding to a group speed of approximately $0.84c$ for both pulses.

4.2 Collisionless stimulated Brillouin scattering

Figure 4.2.1 shows the evolution of the transverse electric field as the seed and pump fields interact via stimulated Brillouin scattering for the simulations performed where collisional effects are neglected. Energy transfer from the pump to the seed is observed, whilst the seed duration is kept approximately constant avoiding any significant amplification via compression of the pulse. After approximately 1840 ω_p^{-1}, where $\omega_p = \omega_0$ and is the normalizing parameter used for all of the OSIRIS results presented in this thesis, the seed pulse reaches maximum amplitude, after which the energy transfer process begins to degrade and the pulse loses its integrity. It can clearly be seen that the pump field is significantly depleted behind the leading edge of the seed indicating that a significant fraction of the available energy in the pump field has been transferred to the seed. It is also noted, however, that there is a

large proportion of pre-pulse generated when collisional effects are neglected which is particularly unfavorable for use in laser-plasma applications.

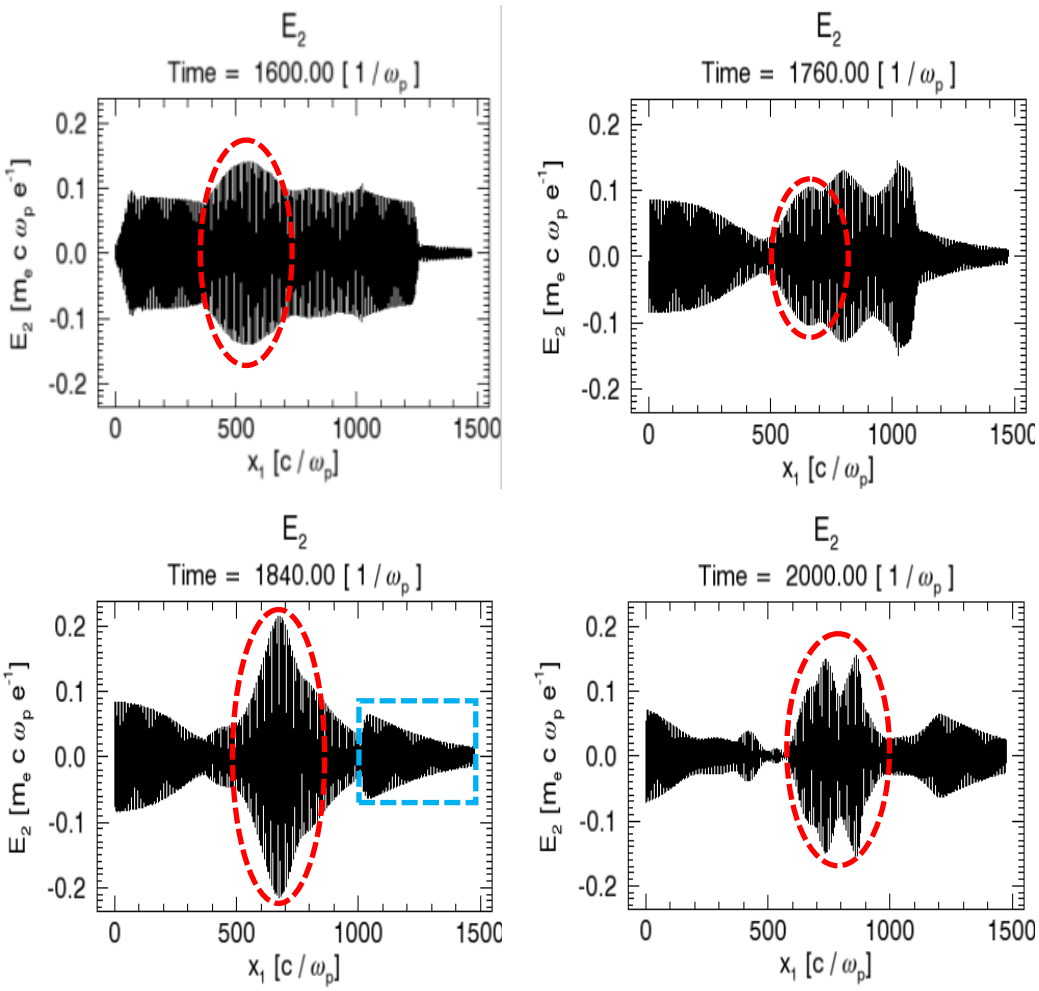

Figure 4.2.1 - Transverse electric field profile at t = 1600, 1760, 1840, 2000ω_p^{-1} for PiC simulation with collisional effects neglected. The amplified seed is circled in red and the pre-pulse is identified with the blue box.

Analysis of the phase space plots for this process strongly indicates the excitation and growth of a number of IAW's associated with the Brillouin scattering mode. Figure 4.2.2 shows phase space plots for the plasma ion population from the point where the energy transfer process is initiated up until the seed has reached maximum intensity. On the left hand side of each of the plots the IAW corresponding to the

driven process, resulting from the beating of the seed and pump fields together, is seen to be excited and grow steadily until a time of $t = 1840\omega_p^{-1}$, commensurate with the saturation of the energy transfer between the seed and pump. It can also be seen, however, that in addition to the excitation of the beat ion acoustic wave associated with the driven process a number of other, naturally occurring, IAW's are also excited. These waves can be seen to emanate from the RHS of the simulation volume and are due to the pump laser undergoing naturally occurring stimulated Brillouin scattering before the pump/seed pulse interaction. Without collisional damping effects being present, the threshold for stimulated Brillouin scattering is effectively zero which results in growth of ion acoustic waves and subsequent depletion of the pump wave before the pump and the seed overlap. This has an adverse effect on the pump/seed energy transfer efficiency.

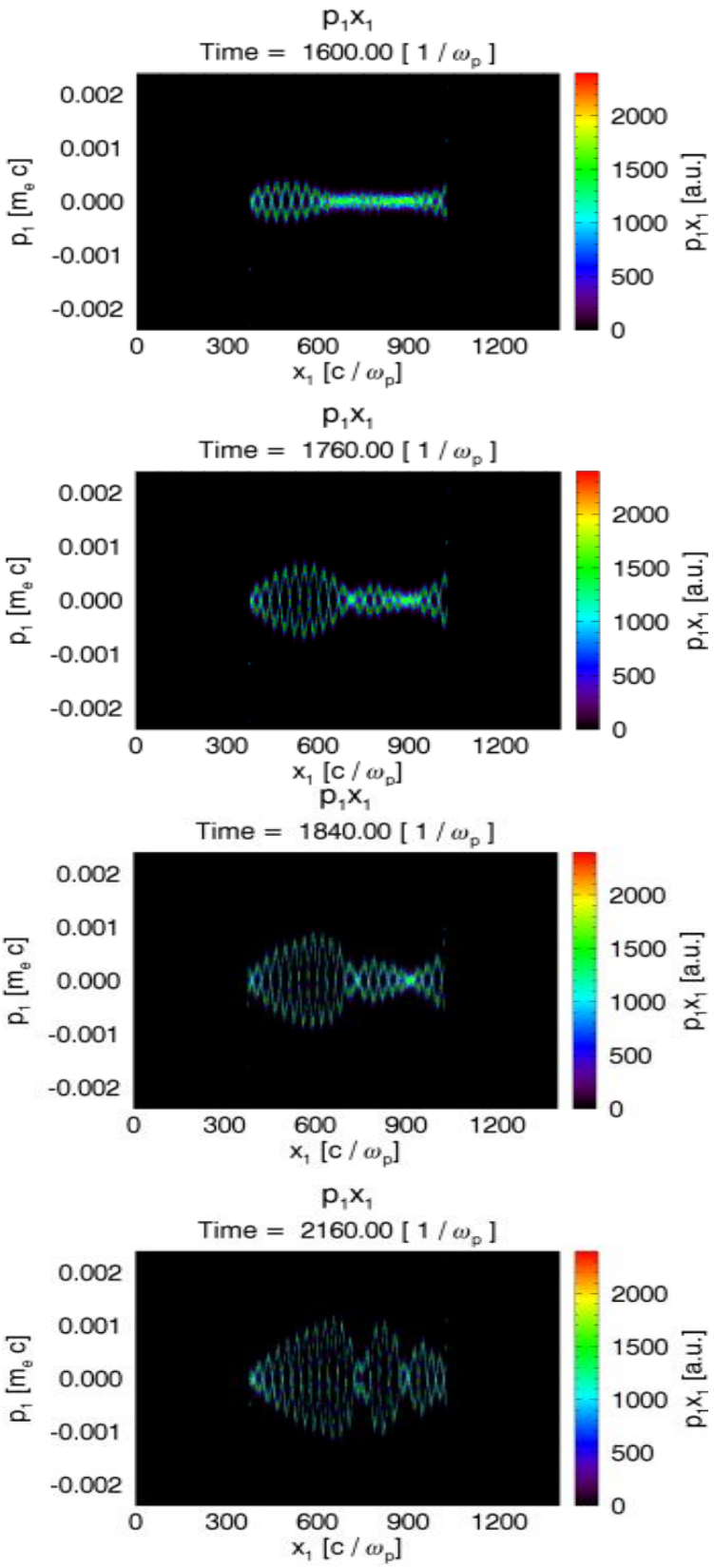

Figure 4.2.2 - Ion phase space plots at t = 1600, 1760, 1840, 2160ω_p^{-1} for PiC simulation with collisional effects neglected.

4.3 Identification of the Brillouin scattering mode

To confirm that the observed seed pulse amplification is as a result of stimulated Brillouin scattering it is necessary to analyse the Fourier transforms of the electric field data. In order to conduct this analysis, calculations of the expected pump laser and ion acoustic frequencies must firstly be theoretically determined to provide a comparison to the observed simulation spectra.

4.3.1 Theoretical calculation of the ion acoustic properties

Beginning with the frequency and wavenumber matching conditions previously given by equations (2.8.1) and (2.8.2) and replacing the subscripts 1 and 2 with S and IA, denoting the scattered and ion acoustic waves, respectively, we get:

$$\omega_0 = \omega_S + \omega_{IA} \tag{4.3.1.1}$$

$$\boldsymbol{k_0} = \boldsymbol{k_s} + \boldsymbol{k_{IA}} \tag{4.3.1.2}$$

where $\boldsymbol{k_0} = {}^{\omega_0}/_{c}$ and $\omega_{IA} = \boldsymbol{k_{IA}} c_s$.

When considering stimulated Brillouin scattering in 1D the scattered wave propagates in the opposite direction to the pump wave but has a wavenumber approximately equal in value, $\boldsymbol{k_0}$, we can deduce that the wavevector for the ion acoustic wave is:

$$\mathbf{k}_{IA} = 2\boldsymbol{k_0} \tag{4.3.1.3}$$

And therefore:

$$\omega_{IA} = 2\boldsymbol{k_0} c_s \tag{4.3.1.4}$$

This provides an indication of the approximate wavevector and frequency at which the IAW should be observed, providing the pump wavevector is known. Evidence of a spectral peak at this value will provide confirmation of the Brillouin mode as the mechanism for the observed energy transfer.

4.3.2 Theoretical calculation of the pump laser properties

The value for the pump laser wavevector is obtained from the dispersion relation detailing wave propagation in plasma. As the dispersion relations for wave propagation in vacuum and in plasma are quite different it is necessary to derive the group speed of the pulse for the plasma density specified in the numerical simulations.

The dispersion relation for wave propagation in a plasma is given by:

$$\omega^2 = \omega_p^2 + c^2 k^2 \tag{4.3.2.1}$$

and the group velocity of an electromagnetic wave is:

$$v_g = \frac{d\omega}{dk} \tag{4.3.2.2}$$

Differentiating (4.3.2.1) with respect to k we get:

$$\frac{d\omega}{dk} = c^2 \frac{k}{\omega} \tag{4.3.2.3}$$

Upon substitution for k, (4.3.2.3) becomes:

$$\frac{d\omega}{dk} = c\sqrt{1 - \frac{\omega_p^2}{\omega^2}} \tag{4.3.2.4}$$

The plasma density used is $0.3n_c$ and as $\omega_p^2/\omega^2 = n_0/n_c = 0.3$

$$v_g = c\sqrt{1 - 0.3} = 0.84c \tag{4.3.2.5}$$

4.3.3 Analysis of Fourier spectra from simulation data

By taking the Fourier transform of the transverse electric field the form of the scattering process can be seen. Figure 4.3.3.1 details four plots each showing the

process evolving as the laser propagates through the plasma. At the first time step displayed, corresponding to $480\omega_p^{-1}$, the pump laser is travelling between the boundary and the plasma in a region of vacuum, resulting in a wavevector value of 1.0, which is normalised to the laser frequency. Early signs of scattering can be seen in this spectrum via the excitation of small sidebands formed on either side of the main peak corresponding to Stokes and anti-Stokes modes. In the second plot, corresponding to $560\omega_p^{-1}$ the leading edge of the pump has traversed into the plasma slab and as such a small second peak corresponding to a wavevector of 0.84 is observed. This part of the spectra corresponds to the wavevector value derived from the dispersion equation for wave propagation in plasma of density $0.3n_c$, detailed in equation 4.3.2.5 above. The third plot details the further excitation and scattering of the laser field in the plasma and the final plot is a close-up view of the scattering observed. It can be seen from this spectra that there is a second, quite distinct, down shifted peak generated. The wave that this peak originated from can be diagnosed via a Fourier transform of the longitudinal electric field.

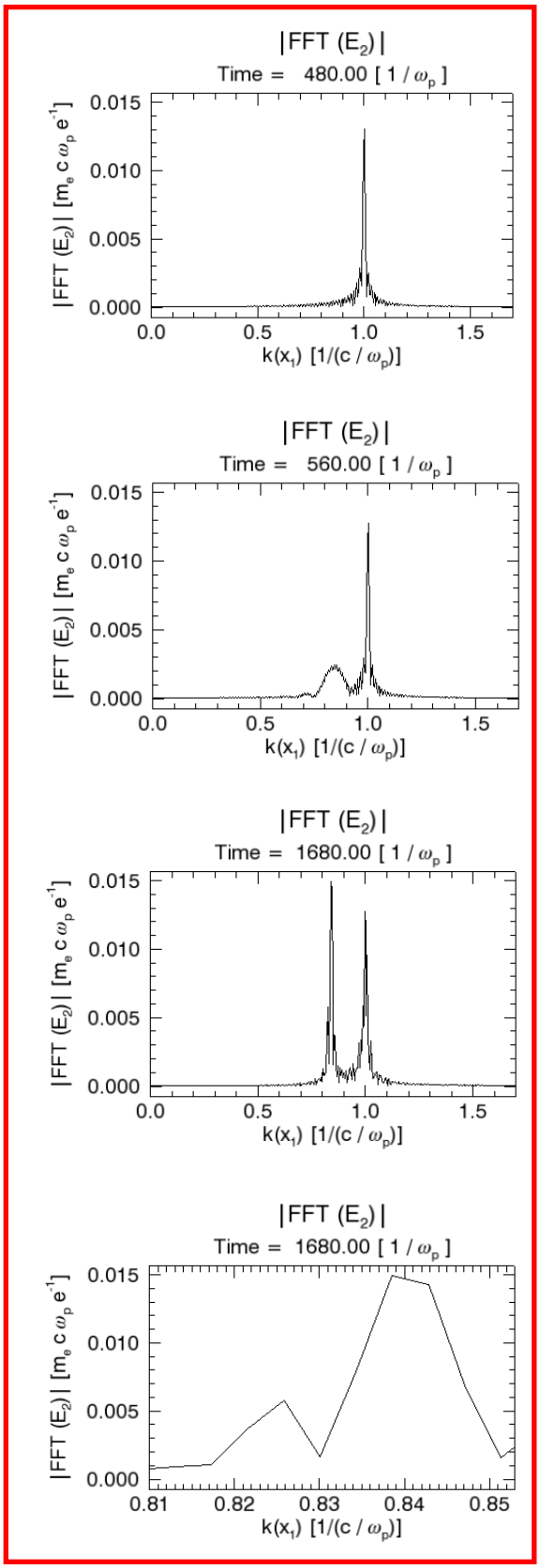

Figure 4.3.3.1 - Fourier transforms of the electric field evolution in the transverse direction at times corresponding to $480\omega_p^{-1}$, $560\omega_p^{-1}$, $1680\omega_p^{-1}$

Fourier transforms of the longitudinal ion acoustic electric field can be seen from figure 4.3.3.2. Spectra are shown for times relating to $1280\omega_p^{-1}$, $1600\omega_p^{-1}$ and $1840\omega_p^{-1}$ where it can be seen that a mode is excited, begins to grow and reaches maximum amplitude, respectively.

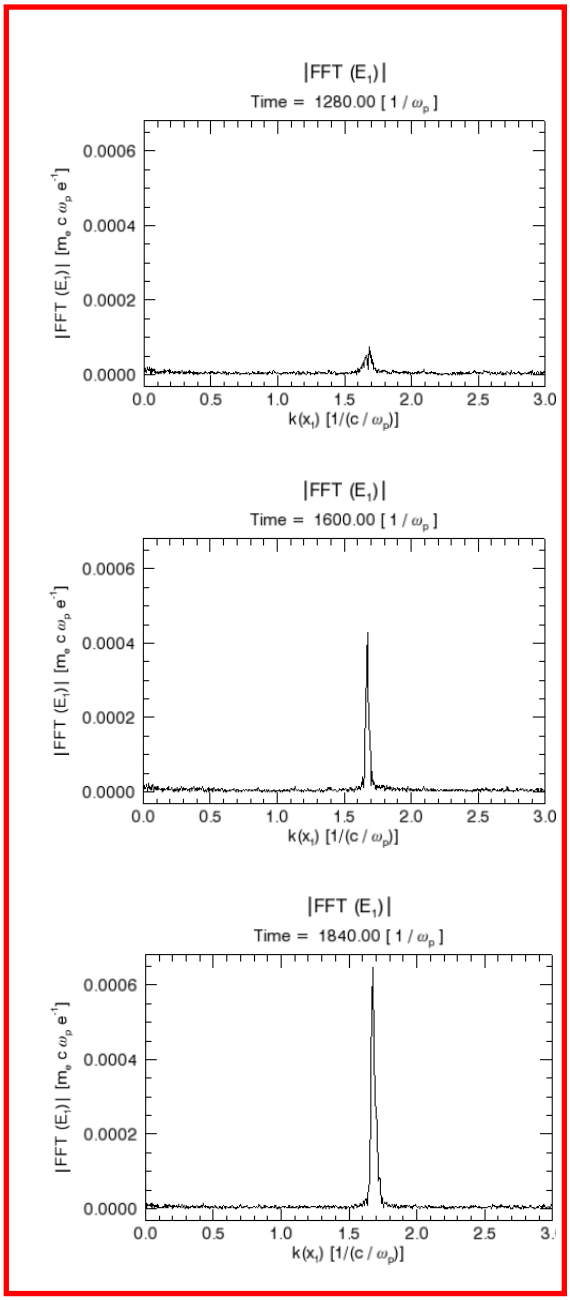

Figure 4.3.3.2 - Fourier transforms of the evolution of the electric field in the longitudinal direction at times corresponding to $1280\omega_p^{-1}$, $1600\omega_p^{-1}$ and $1840\omega_p^{-1}$

Analysis of these waveforms provides confirmation of the existence of an ion acoustic wave and therefore scattering and resulting energy transfer from the pump pulse to a seed laser via the ion acoustic mode driven by SBS. This is due to the fact that this spectral peak occurs at a wavevector of around 1.7 which is approximately $2k_0$. This was the value identified with the presence of an ion acoustic wave, as calculated in sections 4.3.1 and 4.3.2.

4.4 Saturation processes

The mechanisms by which the energy transfer process, from pump to seed laser via stimulated Brillouin scattering, is found to saturate have been previously reported. These processes consist of a combination of ion acoustic wave breaking and the subsequent formation of electron phase space holes. This work on wave breaking [Andreev et al. 2006] and hole formation [Lontano et al. 2006] [Weber et al. 2005a] [Weber, Riconda and Tikhonchuk 2005b] provides a useful benchmark for the simulations performed within this chapter.

4.4.1 Ion acoustic wavebreaking

An investigation of ion acoustic wave breaking was performed and the results of this study are presented in figures 4.4.1.1 and 4.4.1.2

The data in figure 4.4.1.1 shows the excitation of an ion acoustic wave at the first timestep $1680\omega_p^{-1}$, the wave then grows to maximum amplitude and the wavefronts steepen as seen in the second frame at $2080\omega_p^{-1}$, the third plot at $2400\omega_p^{-1}$ shows a drop in wave amplitude as the initial signs of wavebreaking are observed with further signs of wavefront steepening as the particles are accelerated within the wave. The final timestep at $2800\omega_p^{-1}$, shows the full effects of wavebreaking as the periodic wave structure breaks down marking the end of the amplification process.

The corresponding plots in figure 4.4.1.2 detail the Fourier transforms of the longitudinal electric field at the same timesteps as the phase space plots. It can be seen initially at $1680\omega_p^{-1}$ that an ion acoustic wave with the expected wavenumber value is excited, then as the wave becomes unstable and signs of wavebreaking are exhibited a number of harmonics of the original wave are excited, as seen in the

second and third plots at timesteps $2080\omega_p^{-1}$ and $2400\omega_p^{-1}$, respectively. Finally at $2800\omega_p^{-1}$ the original IAW and its harmonics begin to drop in amplitude and show further signs of degradation as the energy transfer process comes to a halt.

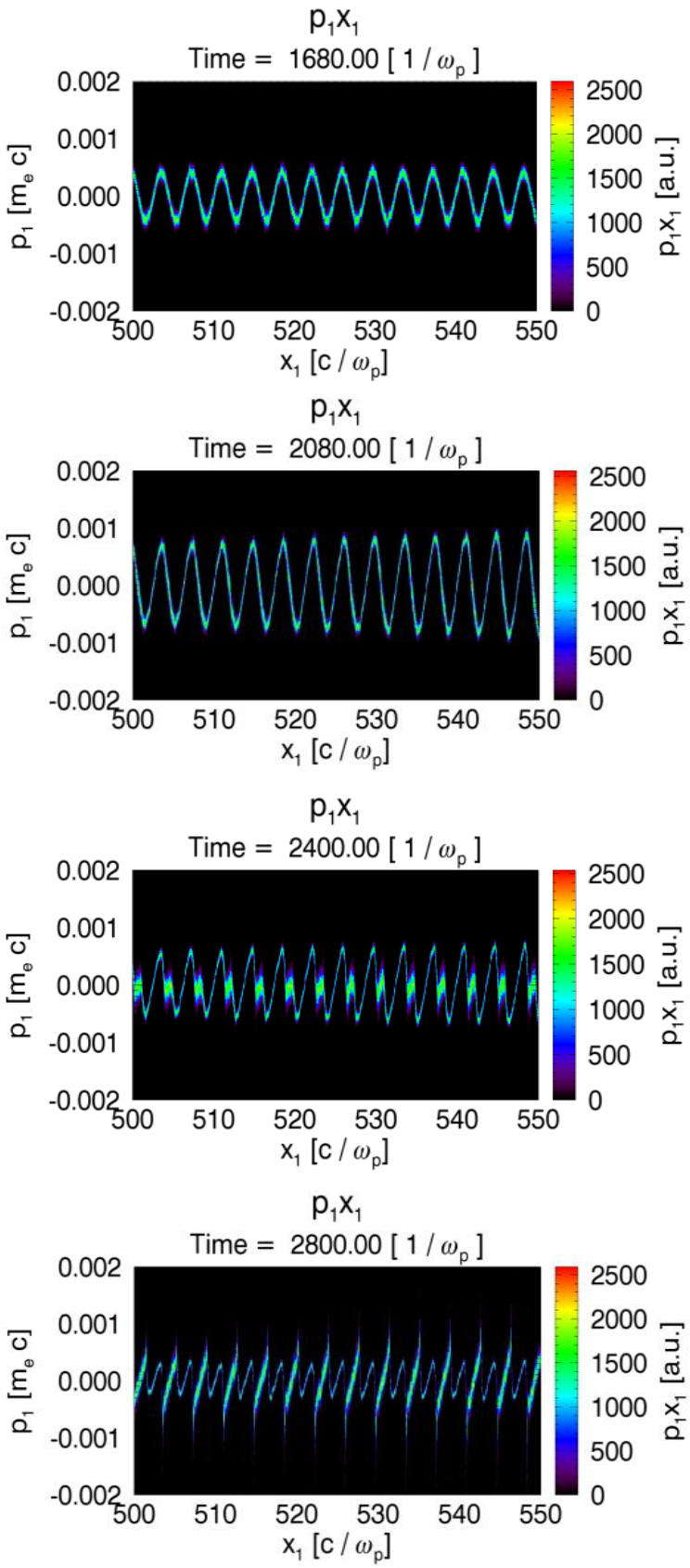

Figure 4.4.1.1 – Phase space plots of ion acoustic waves generated

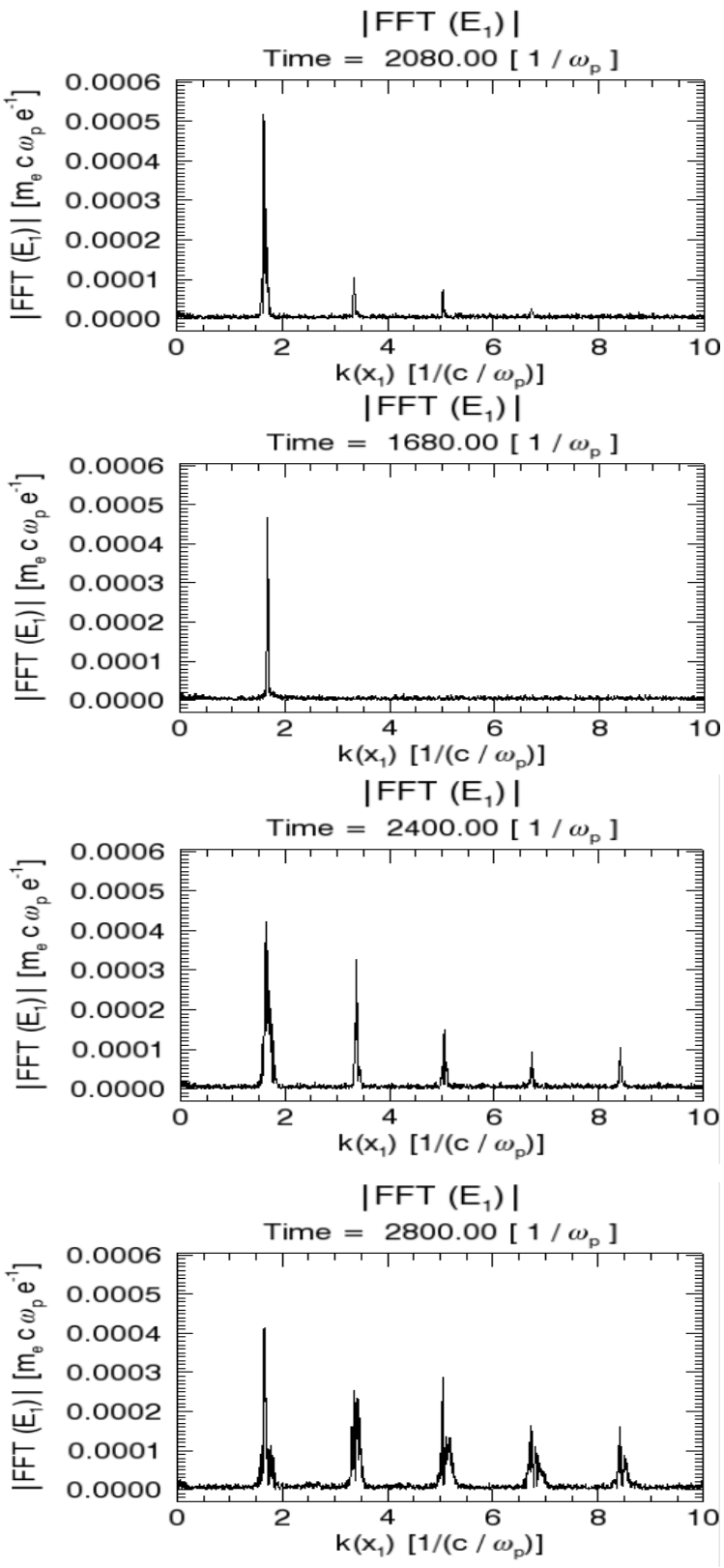

Figure 4.4.1.2 –Fourier transforms of the electric field in the longitudinal direction.

4.4.2 Electron phase space hole formation

As the development of phase space holes have been widely reported by others [Lontano et al. 2006] [Weber et al. 2005a] [Weber, Riconda and Tikhonchuk 2005b], the discussion of these will be limited to a brief analysis of this process, in this section, for completeness. The onset and formation of these structures can be seen in figure 4.4.2.1 at timesteps corresonding to the ion acoustic wave data presented previously in figure 4.4.1.1 and 4.4.2.2.

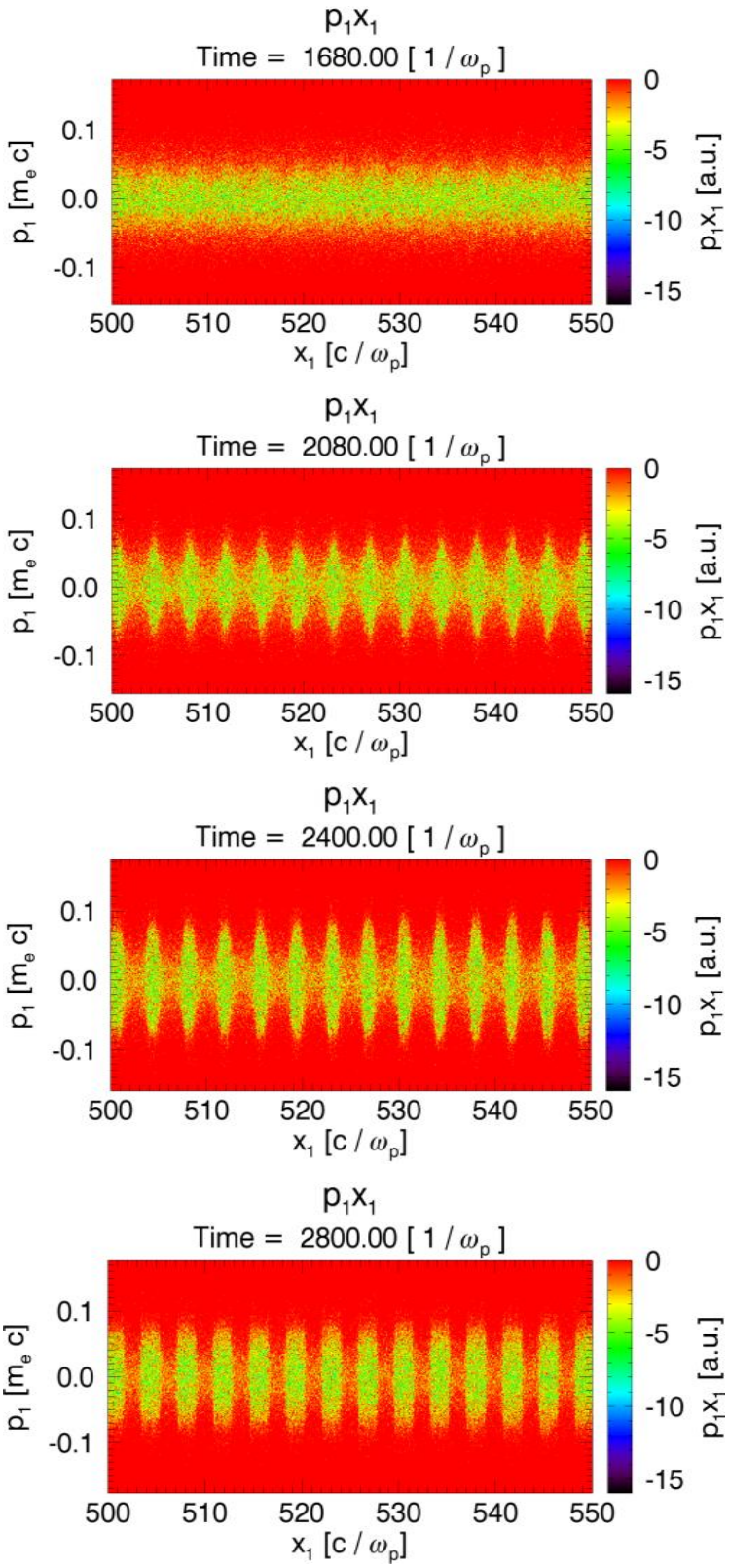

Figure 4.4.2.1 – Phase space plots of plasma electron population at times corresponding to $1680\omega_p^{-1}$, $2080\omega_p^{-1}$, $2400\omega_p^{-1}$ and $2800\omega_p^{-1}$

It can be seen from the first plot at $1680\omega_p^{-1}$ that the plasma electrons have begun to exhibit the initial signs of bunching as the ion acoustic wave is excited and begins to grow, as seen in the ion phase space data in figure 4.4.1.1 at the corresponding timestep. As the ion acoustic wave reaches maximum amplitude and shows regions of particles being accelerated within the waves, as seen in figure 4.4.1.1 at timesteps $2080\omega_p^{-1}$ and $2400\omega_p^{-1}$, the effects of particle trapping in the electron population is increasingly evident where regions of significant particle depletion can be seen. An increase in the species momentum is also noted and is attributed to electron heating. In the final plot displayed at $2800\omega_p^{-1}$ full cavity formation is observed, corresponding to saturation of the Brillouin scattering process and collapse of the ion acoustic wave as seen at the corresponding timestep in figure 4.4.1.1.

4.4.3 Analysis of benchmarks to existing literature

Overall, it has been shown from the data presented in section 4.4 of this thesis that as the ions are accelerated, leading to the onset of wavebreaking, the electrons are strongly heated resulting in the formation of cavity-like structures.

The results presented in this section regarding the mechanisms leading to the saturation of stimulated Brillouin scattering are commensurate with the data and analysis presented by Andreev et al. [Andreev et al. 2006] for ion acoustic wavebreaking and [Lontano et al. 2006] [Weber et al. 2005a] [Weber, Riconda and Tikhonchuk 2005b] for cavity formation. This work provides a useful benchmark for the results presented that confirms that the key physics underpinning the process of stimulated Brillouin scattering is captured by the PiC simulations.

4.5 Collisional stimulated Brillouin scattering

Analysis of the effect of including collisional processes, in the form of Monte-Carlo collisions, into the PiC simulation setup can be seen in figure 4.5.1.

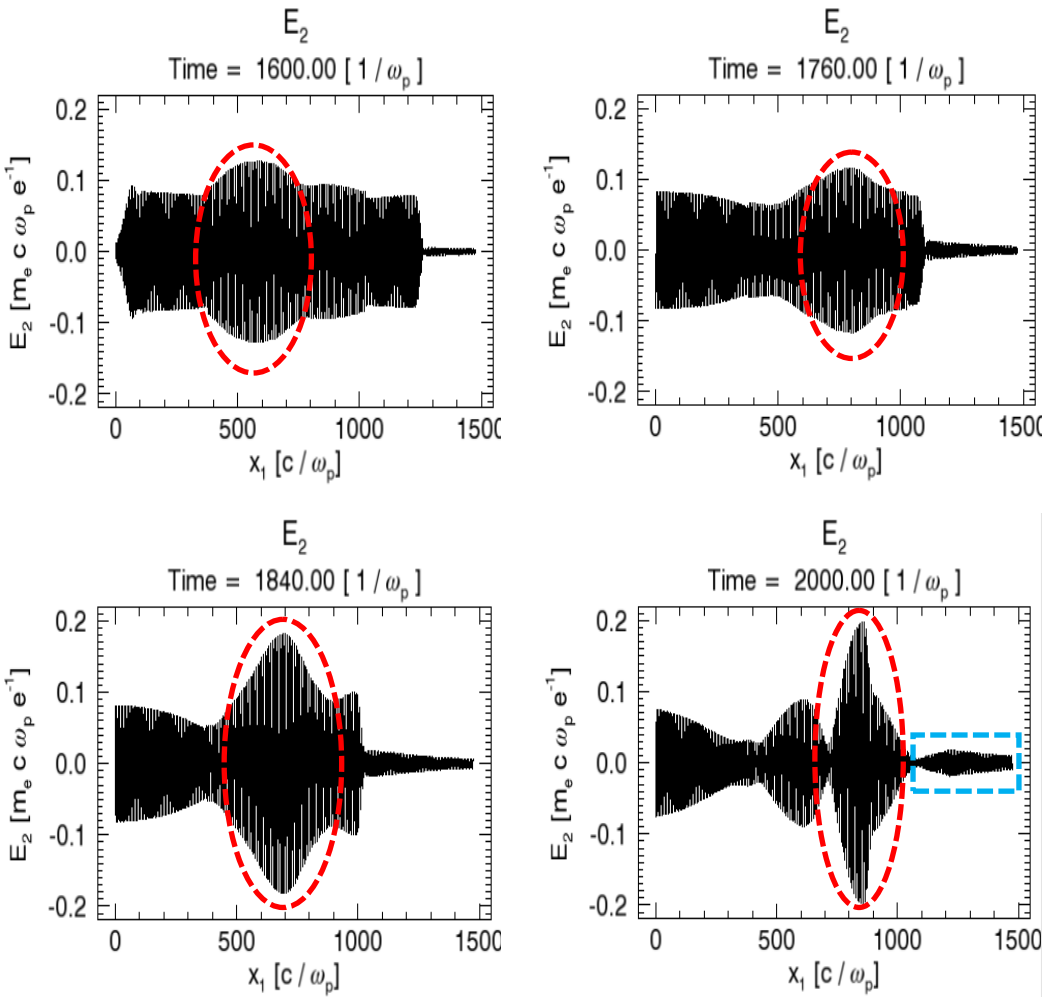

Figure 4.5.1 - Transverse electric field profile at t = 1600, 1760, 1840, 2000ω_p^{-1} for PiC simulation with collisional effects included. The amplified seed is circled in red and the pre-pulse is identified with the blue box.

Upon comparison of these transverse electric field plots to the plots at the same timestep in figure 4.2.1, associated with the collisionless setup, it can be seen that there are some significant differences. It can be seen that the growth of the energy transfer process is slower; meaning the seed pulse takes longer to reach maximum amplitude. Due to this reduced growth rate, the resultant seed has a shorter duration as it takes longer to deplete the pump field. This causes the pulse to split into a number of beamlets resulting in a marginal decrease in the final seed amplitude from that of the collisionless case. Again it is seen that the portion of the pump laser field which has interacted with the seed pulse is significantly depleted indicating that the energy transfer mechanism remains efficient with the collisional effects included in

the code. Of particular interest is the significant reduction in the volume of pre-pulse generated when collisional processes are accounted for. The introduction of collisions therefore provides a significant improvement in the contrast of the laser beam with a very small sacrifice in the resultant laser amplitude, compared with the same pump length, for amplified pulses resulting from stimulated Brillouin scattering.

The most significant difference between the two cases can be observed from figure 4.5.2 when compared directly with the plots at the same time iterations in figure 4.2.2.

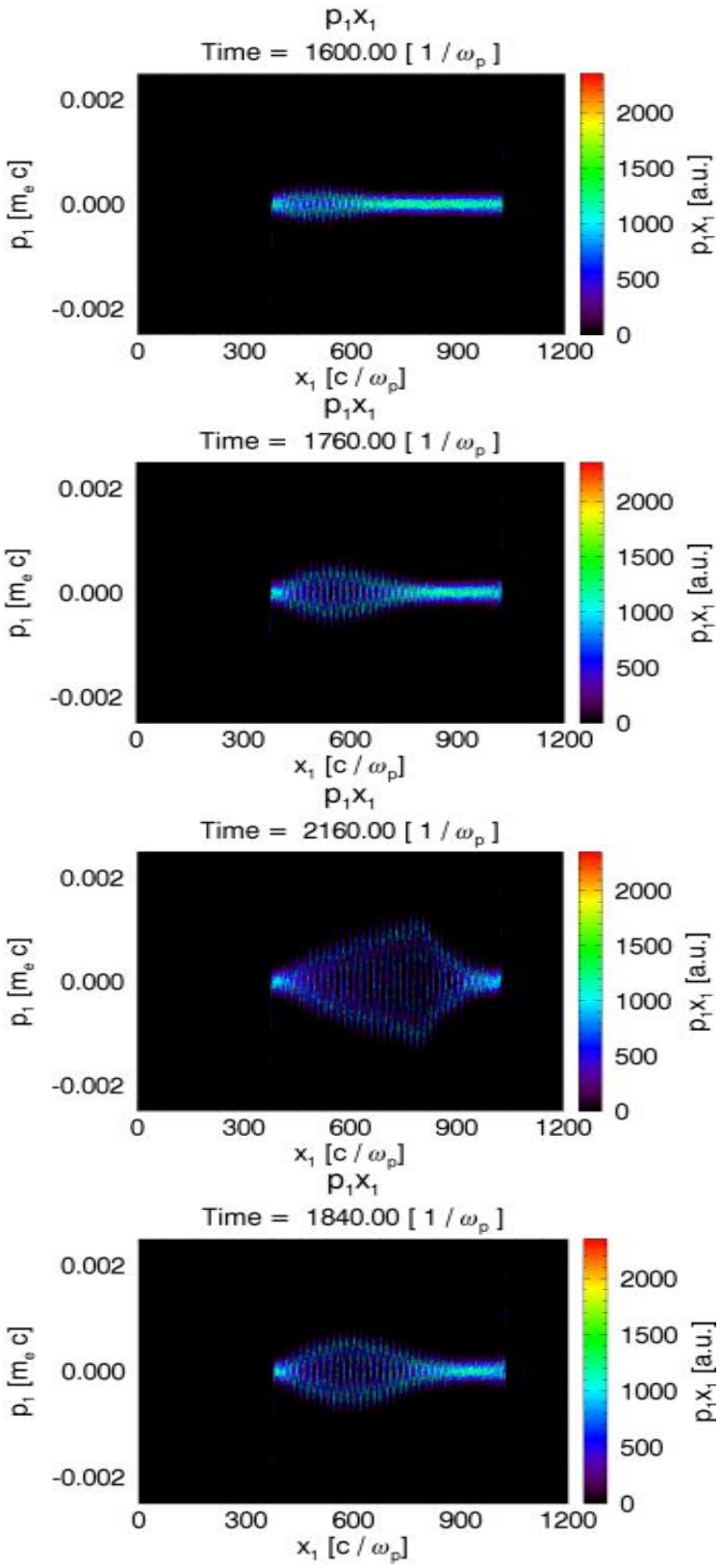

Figure 4.5.2 - Ion phase space plots at t = 1600, 1760, 1840, 2160ω_p^{-1} for PiC simulation with collisional effects included.

It can be seen that the naturally growing IAW's previously seen on the RHS of the simulation box have vanished. This is due to the fact that by including collisional processes into the simulation we encounter a threshold for the normal three-wave scattering process that prevents mode competition between the beat-wave driven and naturally occurring Brillouin scattering mechanisms. In the absence of collisions there is no such threshold meaning that both the naturally occurring three-wave Brillouin scattering and the beat wave Brillouin scattering process are present. This is consistent with the pump and seed frequencies, equaling 10^{16} Wcm^{-2} and 10^{15} Wcm^{-2}, respectively, being above the threshold for SBS. By damping the unwanted normal three-wave Brillouin process, resulting from the scattering of the pump field before the pump/seed laser interaction, premature depletion of the pump laser can be minimized ensuring that the energy available for exchange between the pump and seed lasers is maximized.

4.6 Efficiency considerations

4.6.1 Overview

In order to gauge the fraction of energy that is transferred from pump to probe a measure of the efficiency of the process can be obtained using:

$$E_{ff} = \frac{1}{2} \times \frac{L_1 \times I_1}{L_0 \times I_0} \times 100\% \qquad (4.6.1.1)$$

Where L denotes the length of the pulse, I is the intensity and the subscripts 1 and 2 relate to the seed laser and pump laser pulses, respectively. This efficiency calculation is based on the shape of the laser pulses with the triangular seed pulse having an area equal to $0.5 \times base \times height$ and the rectangular pump pulse having an area equal to its $base \times height$, respectively.

For the purposes of comparison an intensity plot of the initial amplitudes of the pump and seed pulses are shown in figure 4.6.1. This plot denotes the initial conditions for both the collisionless and collisional cases.

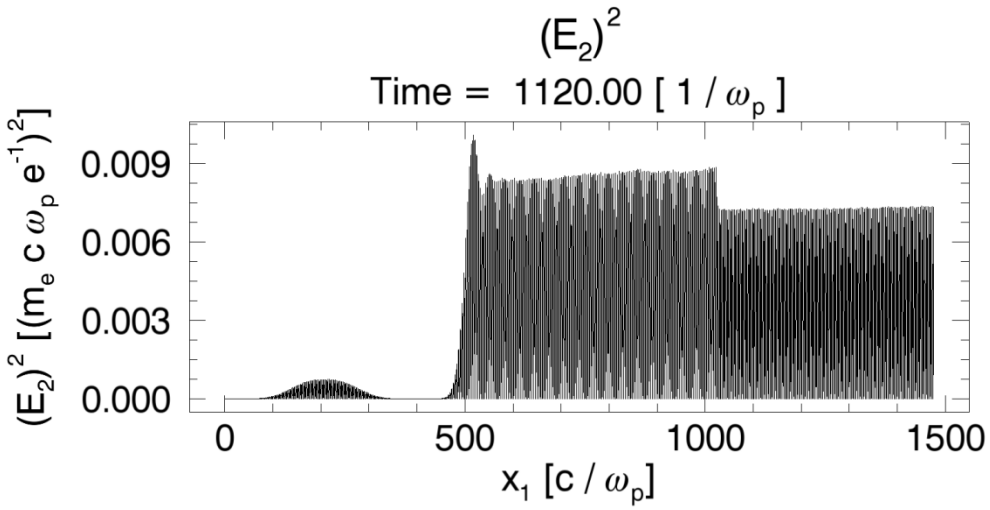

Figure 4.6.1 – Plot of the square of the transverse electric field of the initial pump and seed pulses

4.6.2 Collisionless Calculations

The final, amplified, seed pulse for the case where there are no collisions can be seen in figure 4.6.2. The efficiency of the energy transfer via SBS in this case was calculated using equation 4.6.1 and found to be 28%.

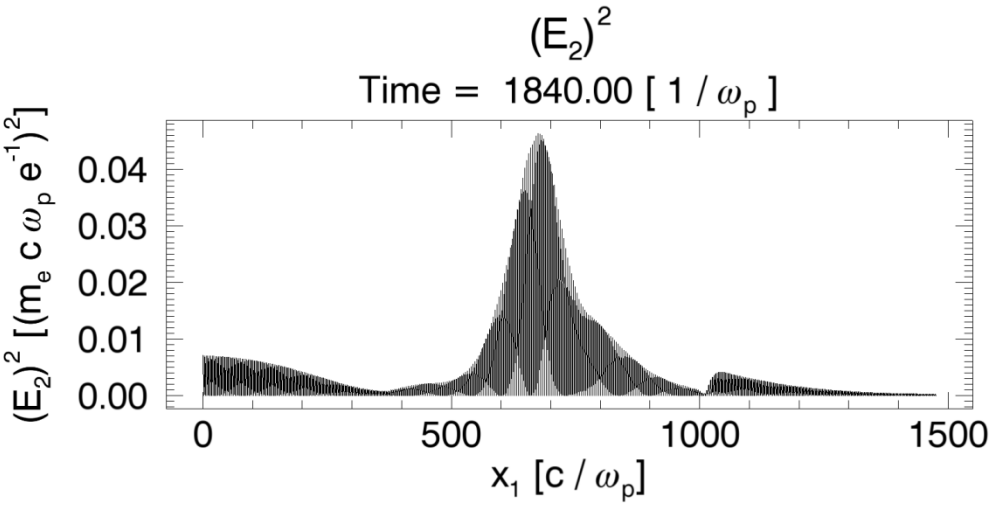

Figure 4.6.2 – Plot of the square of the transverse electric field for the amplified seed pulse for the collisionless simulation

4.6.3 Collisional Calculations

The final intensity of the seed pulse, after amplification, for the collisional case can be seen in figure 4.6.3. The efficiency of the energy transfer in this case, again calculated using equation 4.6.1, was found to be 38%.

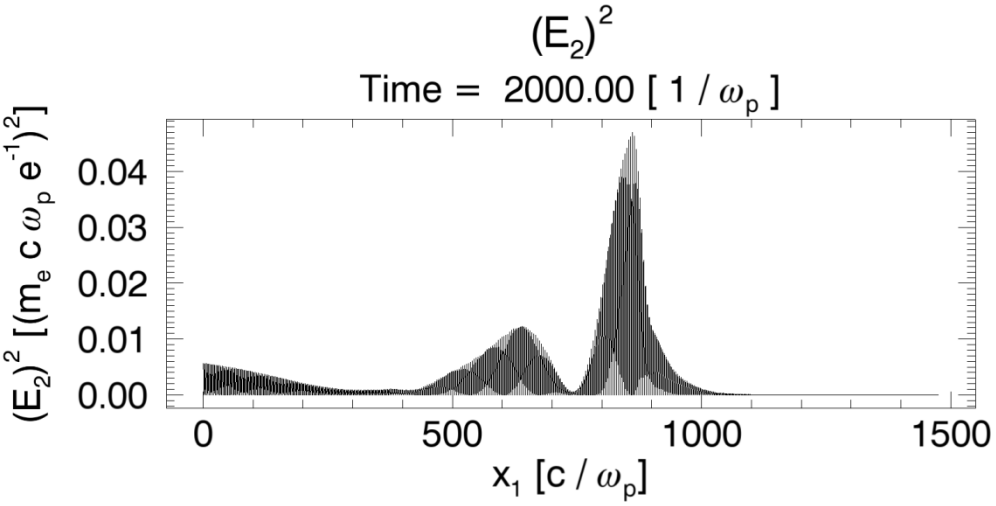

Figure 4.6.3 - Plot of the square of the transverse electric field for the amplified seed pulse for the collisional simulation

4.6.4 Discussion

Upon comparison of both sets of results it is found that the efficiency of the collisional process is found to be 10% higher than that for the collisionless process. This is attributed to the fact that in the collisional case the Brillouin scattering process resulting from the pump field is no longer able to prematurely deplete the energy available for transfer to the seed pulse, causing degradation in the energy transfer process. This is as a direct result of the induced collisional threshold which is introduced when collisional effects are accounted for.

A good representation of the extent of the energy transfer observed from the numerical simulations of stimulated Brillouin scattering for each of these cases is observed upon comparison of figure 4.6.4 with figures 4.6.2 and 4.6.3. Figure 4.6.4 details the initial laser intensities before resonance has occurred on a scale comparable with the final pulse amplitudes observed in 4.6.2 and 4.6.3. It can therefore be seen that the seed pulse has been amplified by a factor of approximately 60 times with respect to the initial seed pulse amplitude.

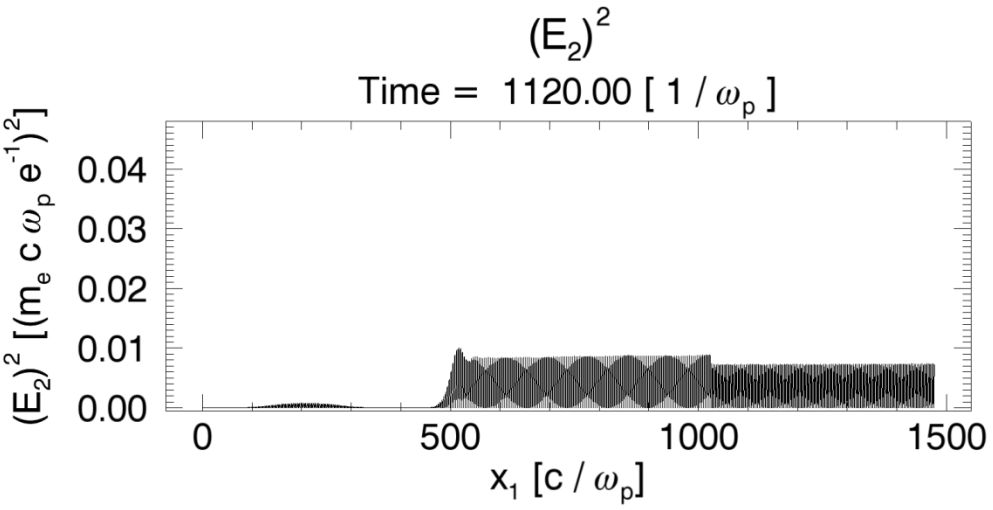

Figure 4.6.4 - Plot of the square of the transverse electric field for the initial counter-propagating seed and pump pulses before resonance has occurred

4.7 Effect of ion temperature variations on SBS

An investigation was also conducted to assess the effect on SBS caused by variations in the plasma ion temperature. The electron temperature was fixed at 500eV for a hydrogen plasma, as in all previous results presented in this chapter, and the ion temperature was varied such that $ZT_e/T_i = 10$, 5, 1 and 0.5, respectively.

In each of the following simulations we introduce normal collisions that are effective all the time and have no dependence on the temperature ratio of the plasma species. This prevents the pump field from scattering and interfering with the energy transfer process, as reported in section 4.6.4. The results of this study can be seen in figure 4.7.1

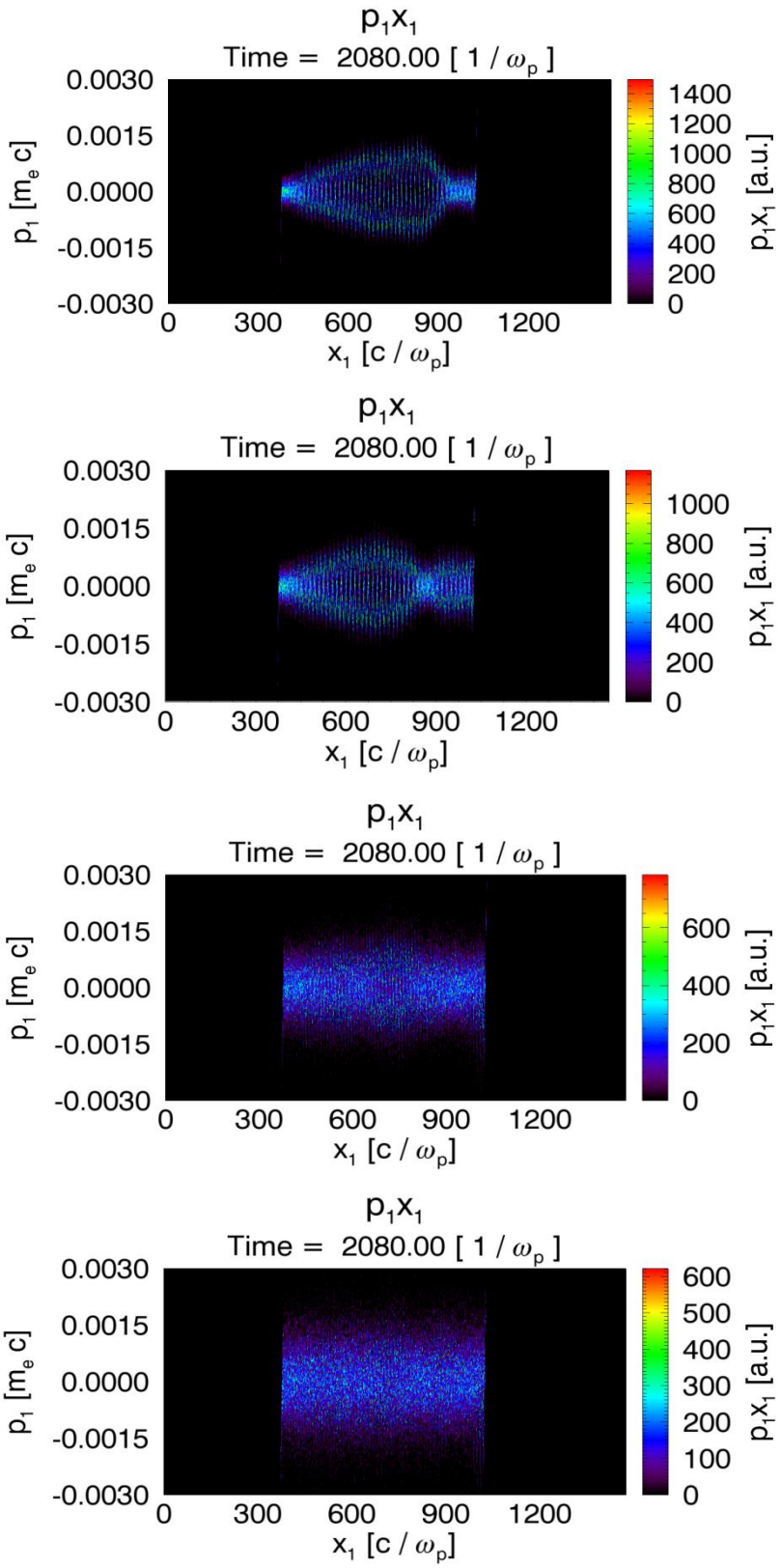

Figure 4.7.1a, b, c, d - Ion phase space plots at t = $2080\boldsymbol{\omega_p^{-1}}$ for PiC simulations with collisional effects included where ZT_e/T_i = 10, 5, 1, 0.5, respectively.

Upon studying the effect of raising the plasma ion temperature such that the ratio of $ZT_e/T_i \rightarrow 0.5$, we can see from each of the frames in figure 4.7.1 that the ion acoustic waves associated with the beat wave generated Brillouin process are increasingly damped. This is due to the fact that for small ZT_e/T_i Landau damping of the ion acoustic wave becomes important.

It has already been demonstrated, in figure 4.5.2, that when $ZT_e/T_i = 50$ the IAW associated with the naturally occurring Brillouin process is damped as the pump wave does not reach the collisional instability threshold, but the beat wave generated IAW is unaffected. However, when the ion temperature is increased such that $ZT_e/T_i = 5$ it can be seen from figure 4.7.1b that both the beat wave driven Brillouin process and the normal three-wave Brillouin scattering processes are present. This is due to the fact that the normal three-wave Brillouin process has exceeded the collisional threshold for the instability. When the ion temperature is raised further such that $ZT_e/T_i = 1$ and $ZT_e/T_i = 0.5$ then it can be seen in figures 4.7.1c and 4.7.1d, respectively, that the IAW's associated with both Brillouin scattering processes are completely damped. This is attributed to Landau damping of the waves as the phase velocity of these waves now lies in a region where there is a large negative slope in the ion distribution function due to the fact that the ions are no longer much cooler than the plasma electron population.

These results are particularly interesting as, in addition to the fact that for high values of ZT_e/T_i the normal three wave Brillouin scattering process can be damped, mitigating competition with the beat wave driven Brillouin process, it is seen that for high enough plasma ion temperatures the Brillouin instability in general, meaning both the beat wave driven and the normal three wave processes, can be completely damped. Thus meaning that energy exchange between beams can be avoided for applications where SBS is undesirable.

4.8 Effect of electron temperature variations on SBS

The effect of variations in the electron temperature on SBS was also investigated. In the results presented here the ion temperature was fixed at 10eV and the electron temperature varied between 1keV and 50eV. As was the case in section 4.5, where a

study of plasma ion temperature variations was conducted, the following simulations have normal collisions enabled that are effective at all times and have no dependence on the temperature ratio of the plasma species. The ion acoustic waves associated with each of these simulations can be seen in figure 4.8.1.

These results show that as the plasma electron temperature is raised from 50eV to 1keV there appears to be little effect on the excitation and growth of the ion acoustic waves generated. It can be seen that each of the IAW's displayed has an approximately equal amplitude and profile.

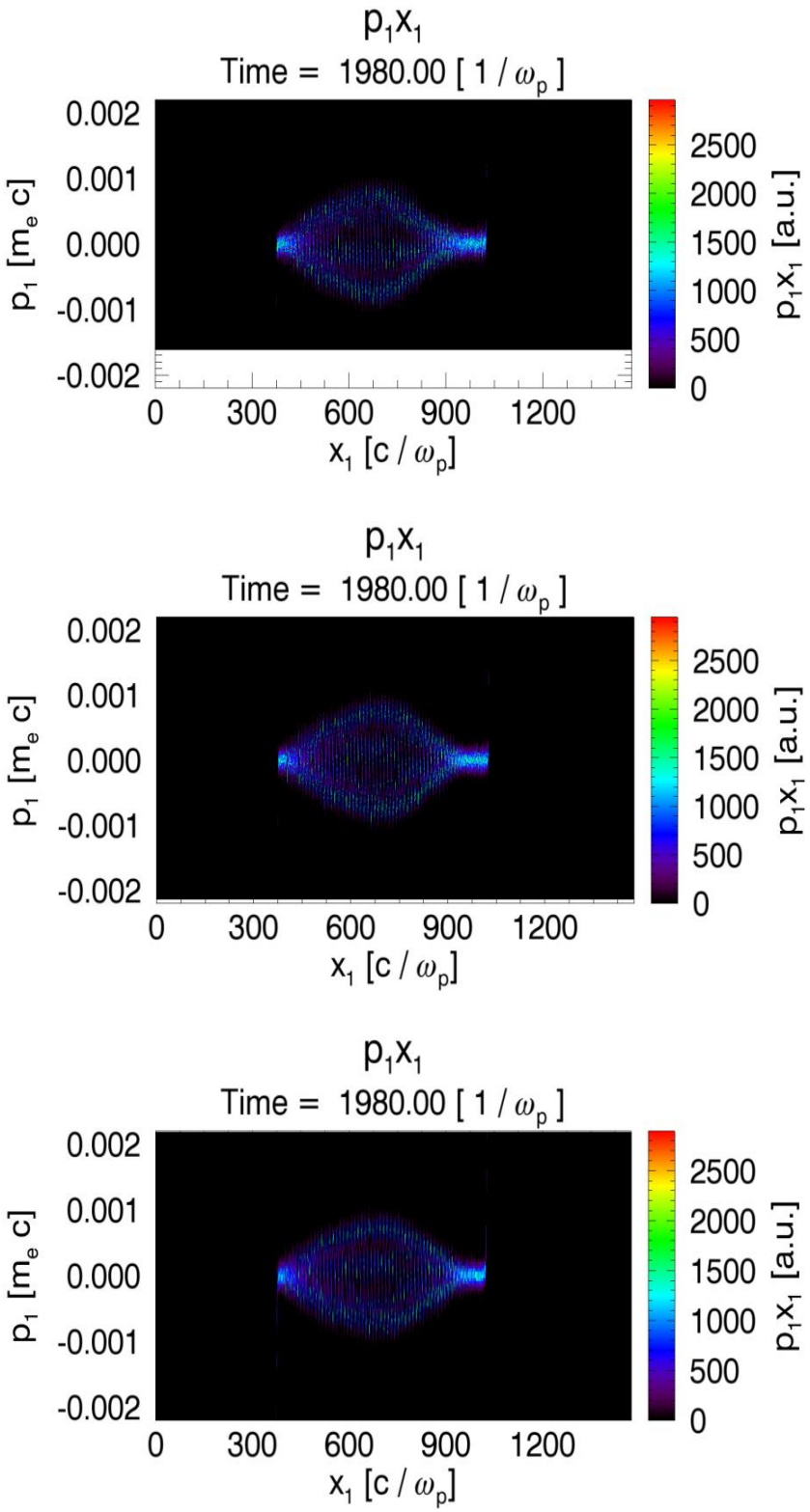

Figure 4.8.1a, b, c - Ion phase space plots at t = $1980\omega_p^{-1}$ for PiC simulations with collisional effects included where T_e = 50eV, 100eV and 1keV, respectively.

As an analysis of the ion phase space data does not detail any noticeable differences to the SBS process as a result of altering the electron temperature, it is necessary to look to the seed pulse growth within the plasma. Figure 4.8.2 shows data where the seed pulse intensity is taken at $1980\omega_p^{-1}$, corresponding to the timestep associated with the phase space data above, and at $2046\omega_p^{-1}$, which corresponds to the maximum amplitude reached by the seed in each of the three cases.

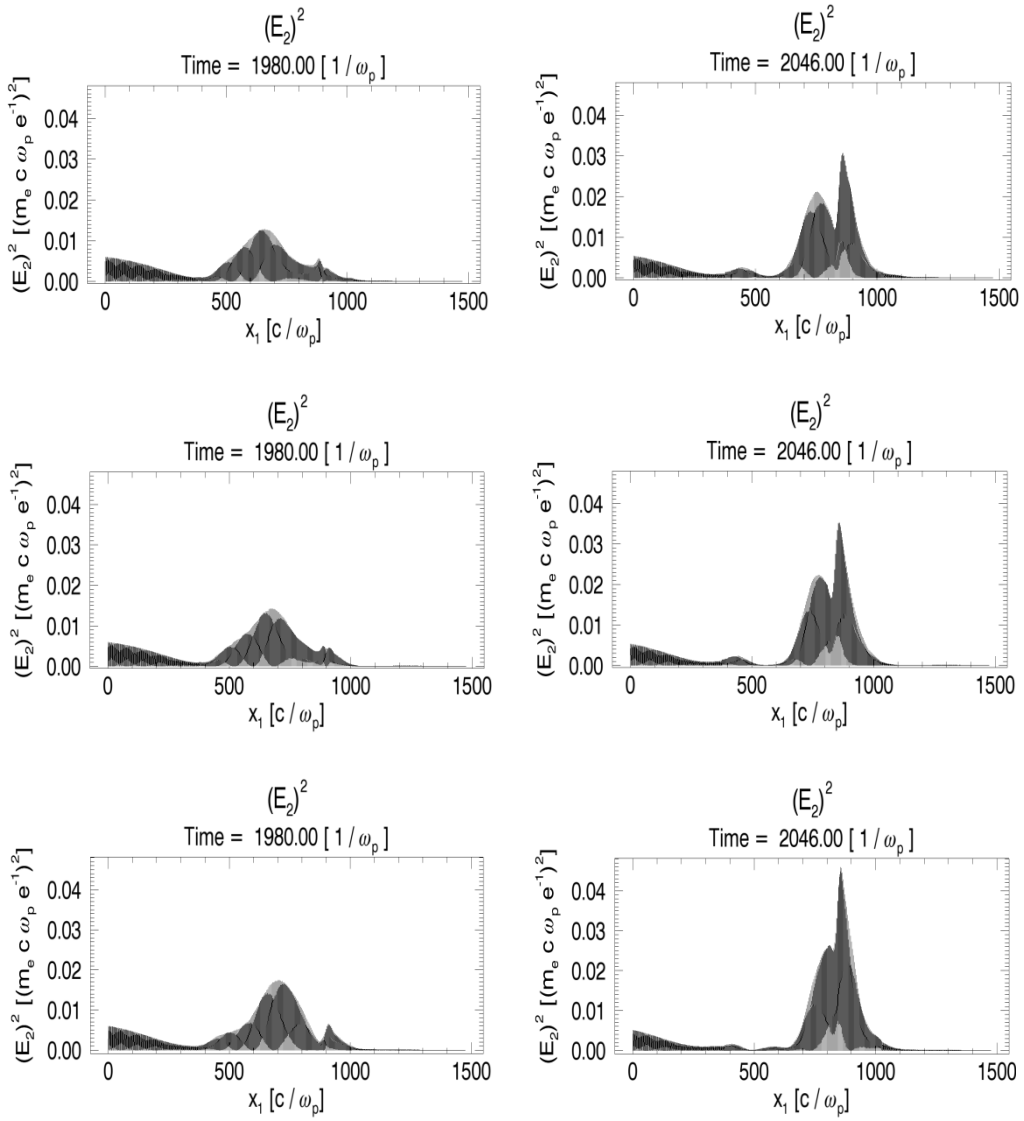

Figure 4.8.2a, b, c – Spectra plot of the square of the transverse electric field at t = $1980\omega_p^{-1}$ and $2046\omega_p^{-1}$ for PiC simulations with collisional effects included where T_e = 50eV, 100eV and 1keV, respectively.

It can be seen from the data above that the evolution of the seed pulses in each of the three cases is very similar and the levels of pump depletion in each case are very high. At $1980\omega_p^{-1}$ each of the pulses has a similar profile with a small increase in amplitude noted as the temperature is increased from 50eV through 100eV to 1keV. At $2046\omega_p^{-1}$ the maximum amplitude is reached for all three pulses with the most noticeable differences between the initial and final pulses evident at this stage in the process.

As the speed of the ion acoustic wave is given by:

$$c_s = \sqrt{(ZT_e + T_i)/m_i} \tag{4.8.1}$$

when the electron temperature is raised the phase speed of the ion acoustic wave also increases. This electron temperature increase, whilst the ion temperature remains fixed, means fewer ions are resonant with the wave and only a small number of the total population of particles can therefore contribute to Landau damping the wave. Thus, accounting for the increase in amplitude observed as the electron temperature is raised.

In addition to these effects it can be seen that the seed spectra begins to split into two, most noticeably when the electron temperature decreases. This observed splitting of the seed pulse is an important behavioural characteristic of stimulated Brillouin scattering and will be described in detail in the following chapter.

4.9 Summary and discussion

We have investigated the effect of damping processes, via collisionless and collisional PiC simulations, on the energy transfer between laser pulses by stimulated Brillouin scattering. We have shown that, for a constant pump to probe ratio, collisional effects are found to damp the normal three-wave Brillouin scattering by inducing a threshold for the instability that is overcome only by the Brillouin process generated by the beating of the pump and seed laser frequencies. This collisional

damping ensures that the pump laser is unable to scatter before interaction with the seed pulse which is found to lead to premature depletion of the energy available for transfer to the seed pulse. In addition to this we have observed the introduction of collisions results in an increase in the efficiency of stimulated Brillouin scattering by 10% and a significant increase in the contrast of the resultant seed laser beam. This is of particular interest in the study of intense laser-plasma interactions where the presence of pre-pulse is particularly unfavorable.

We have also shown that by raising the plasma ion temperature, such that $ZT_e/T_i < 5$, the ion acoustic waves associated with both the normal three wave Brillouin scattering and the beat wave driven Brillouin scattering processes are Landau damped, mitigating the onset and subsequent growth of the instability. This is of particular interest to applications such as direct drive inertial confinement fusion as it has been shown that the Brillouin instability can be completely damped and unwanted energy exchange between beams can be avoided by heating of the ion population. However for applications where Brillouin scattering is desirable it has been shown that an increase in the temperature of the plasma electron population serves only to reduce the amplification of the seed pulse by a minimal amount. This shows the applicability of SBS for a wide range of applications requiring a variety of different plasma parameters.

It can therefore also be concluded that the inclusion of collisional processes in PiC simulations is necessary to diagnose the key physics of stimulated Brillouin scattering in plasmas. Therefore all simulation data presented in this thesis hereafter will be inclusive of collisions.

References

Andreev, A., Riconda, C., Tikhonchuk, V. T. and Weber, S. *Short light pulse amplification and compression by stimulated Brillouin scattering in plasmas in the strong coupling regime.* Physics of Plasmas 13, 053110 (2006)

Lontano, M., Passoni, M., Riconda, C., Tikhonchuk, V. T. and Weber, S. *Electromagnetic solitary waves in the saturation regime of stimulated Brillouin backscattering*. Laser and Particle Beams 24, 125 (2006)

Malkin, V. M., Shvets, G. and Fisch, N. J. *Fast Compression of Laser Beams to Highly Overcritical Powers.* Physical Review Letters 82, 4448 (1999)

Weber, S., Riconda, C. and Tikhonchuk, V. T. *Strong kinetic effects in cavity-induced low-level saturation of stimulated Brillouin backscattering for high-intensity laser-plasma interaction.* Physics of Plasmas 12, 043101 (2005b)

Weber, S., Lontano, M., Passoni, M., Riconda, C. and Tikhonchuk, V. T. *Electromagnetic solitons produced by stimulated Brillouin pulsations in Plasmas.* Physics of Plasmas 12, 112107 (2005a)

Chapter 5
Optimisation of SBS in parameter space

In this chapter analytical theory and particle in cell simulations will be presented to demonstrate the effectiveness of stimulated Brillouin scattering as an alternative technique to Raman scattering for the production of high power laser pulses. As it has already been shown that the final duration of a Raman amplified probe can be increased by reducing the pump pulse intensity, while parasitic laser-plasma instabilities could be kept under control [Trines et al. 2011a], here it will be investigated whether a similar approach also works for Brillouin amplification.

Scaling laws governing the optimal parameter space for the pump beam, seed beam and plasma will be derived using a self-similar model for Brillouin scattering and verified via particle-in-cell simulation data. A comparison with Raman scattering will also be made to determine which scheme is most appropriate for a range of laser-plasma configurations.

5.1 Self-similar model for SBS

In order to effectively optimise SBS for use as a laser amplification technique it is necessary to diagnose the behavioural characteristics associated with this instability. One means of investigating these features is via analysis of the self-similar theory developed for Brillouin scattering. Using the self-similar model of Andreev et al.. [Andreev et al.. 2006] as a starting point it is possible to investigate a number of

interesting features of stimulated Brillouin scattering and, in particular, explore how the final duration of a Brillouin amplified probe pulse can be controlled.

By considering homogenous plasma with electron density n_0, plasma frequency:

$$\omega_{pe}^2 = \frac{e^2 n_0}{\varepsilon_0 m_e} \tag{5.1.1}$$

and ion plasma frequency given by:

$$\omega_{pi} = \omega_{pe}\sqrt{Z^2 m_e/m_i} \tag{5.1.2}$$

and a pump laser pulse with wavelength λ, intensity I, and frequency:

$$\omega_0 = \frac{2\pi c}{\lambda} \tag{5.1.3}$$

with a dimensionless amplitude:

$$a_0 \equiv 8.55x10^{-10}\sqrt{g}\,\sqrt{I\lambda^2[Wcm^{-2}\mu m^2]} \tag{5.1.4}$$

where g = 1 (g = ½) denotes linear (circular) polarisation and wave group speed:

$$\frac{v_g}{c} = \sqrt{1 - \omega_p^2/\omega_0^2} \tag{5.1.5}$$

Let the durations of the pump and probe pulse be given by τ_{pu} and τ_{pr}, respectively, and define the Brillouin scattering growth rate in the strong coupling regime [Forslund, Kindel and Lindman 1975] as:

$$\gamma_B = \left(\frac{\sqrt{3}}{2}\right)\left[a_0\left(\frac{v_g}{c}\right)\omega_{pi}\sqrt{\omega_0}\right]^{2/3} \tag{5.1.6}$$

The model developed by Andreev et al. [Andreev et al.. 2006] is based on finding solutions to the three-wave equations, describing the pump, seed and ion acoustic

waves, as a function of the self-similar co-ordinate. This self-similar co-ordinate is given by:

$$\xi = \eta\sqrt{\tau} \tag{5.1.7}$$

A full expansion of this self-similar co-ordinate, ξ, gives:

$$\gamma_B \tau_{pr} \sqrt{\gamma_B \tau_{pu}} = \sqrt{g/\eta}\xi_B \tag{5.1.8}$$

where $\xi_B \approx 5$ is a numerical constant and η denotes the pump depletion efficiency.

The salient points of (5.1.8) are as follows:

i) The final probe duration increases with decreasing pump intensity, similar to that of Raman amplification. This is due to the fact that the pump intensity is contained within γ_B which is proportional to $I^{1/3}$, so ${\gamma_B}^{3/2} \sim I^{1/2} \sim a_0$. Thus, if τ_{pu} is kept fixed and I goes up then τ_{pr} must come down. If $I\lambda^2$ is kept fixed, there is no difference between linear and circular polarisation as the g factors, which are contained within a_0 and encompassed in the definition of γ_B, on either side of the equation cancel.

ii) Due to the fact that $\omega_{pi} \ll \omega_p$ longer probes are favoured and longer initial probes are needed, compared to Raman amplification. The equivalent expression for Raman amplification contains the factor $\omega_{pe} \times \tau_{pr}$ while this expression contains the factor $\omega_{pi} \times \tau_{pr}$ (ω_{pe} and ω_{pi} are buried in the growth rate gamma). For roughly similar values of $\omega \times \tau_{pr}$, the Brillouin probe will be much longer than the Raman probe because ω_{pi} is much smaller than ω_{pe}.

iii) As there is a square root in equation 5.1.8 extreme Brillouin compression is not very efficient. On the other hand, moderate compression is "almost linear" rather than "square root", i.e. almost as efficient as Raman amplification. This due to the fact that for Raman amplification we have $\tau_{pu} \times \tau_{pr} = constant$, so if we double the pump duration the probe duration will be halved. For Brillouin scattering, we

have $\tau_{pu} \times \sqrt{\tau_{pr}} = constant$ so we have to make the pump 4 times longer if we want to halve the probe duration. However, as there is an offset contained within this expression due to the fact that initial probe cannot have an infinite duration, the expression becomes: $\tau_{pr} \times \sqrt{(\tau_{offset} + \tau_{pu})} = constant.$ This expression is almost linear in τ_{pu} for shorter pump durations, while it behaves as $\sqrt{\tau_{pu}}$ for $\tau_{pu} \gg \tau_{offset}.$

It can therefore be said that Brillouin amplification favours longer pulses and less extreme compression than Raman amplification. Due to this and the fact that Brillouin amplification has a lower growth rate than that of Raman scattering it cannot produce the kind of ultrashort (~25 fs) pulses that can be obtained via Raman amplification. While this is sometimes seen as a drawback, it is this very property that renders Brillouin amplification even more suitable for the production of high-energy picosecond pulses than Raman amplification. This feature of SBS will be investigated in more detail later in this chapter.

5.2 Numerical verification of seed duration predictions

To illustrate this behaviour, a series of 1-dimensional particle-in-cell simulations using the Osiris 2.0 framework were conducted. The simulation parameters were as follows: fully-ionised hydrogen plasma was assumed with $m_i/m_e = 1836$ and $Z = 1$, where $T_e = 500eV$, $T_i = 10eV$ and $n_e = 0.3n_c$ for $\lambda_0 = 1\mu m$. Furthermore, $\omega_0 \delta t = \omega_0 \delta x/c = 0.04$ so $\delta x/\lambda_D = 0.7$ and 100 particles per cell were used. The probe laser pulse had an intensity of 1.0×10^{15} W cm^{-2} and a duration of 200fs in each simulation, moving to the right. The counter-propagating pump laser pulse had a duration of 1.45ps, while its intensity was varied to study the effect on the final probe duration. The probe pulse was launched just to the left of the plasma column, of length $200\mu m$, at the moment that the pump pulse front had traversed the entire plasma column and was about to emerge from it.

The simulation results from this study are displayed in Figure 5.2.1. From top to bottom the developing probe pulse is shown for a pump intensity of $1.0\text{x}10^{16}$, $3.0\text{x}10^{15}$, $1.0\text{x}10^{15}$ and $3.0\text{x}10^{14}$ Wcm^{-2}, respectively. Snapshots were taken at $\omega_0 t$ = 3360, or 0.86ps after the launch of the probe pulse, just after it had emerged from the plasma column.

From the results shown it can be seen that the duration of the (leading spike of the) final probe pulse clearly increases with decreasing pump pulse intensity, from about 50fs for the highest intensity to about 300fs for the lowest, corresponding to factor 6 in length increase for a factor 5.8 decrease in a_0. It can also be said that the lower the pump pulse intensity the longer it takes for the pump pulse to transfer energy to the seed pulse in order for amplification of the seed to occur. This is confirmed upon analysis of the amplitudes of the seed pulses shown in figure 5.2.1 as the resultant seed amplitude is found to steadily decrease as the pump intensity is lowered.

It is therefore clearly demonstrated that, as predicted from the self-similar theory detailed in section 5.1, little pulse compression is exhibited which shows that SBS favours longer pulse lengths and the final probe duration increases with decreasing pump intensity in a similar fashion to Raman amplification.

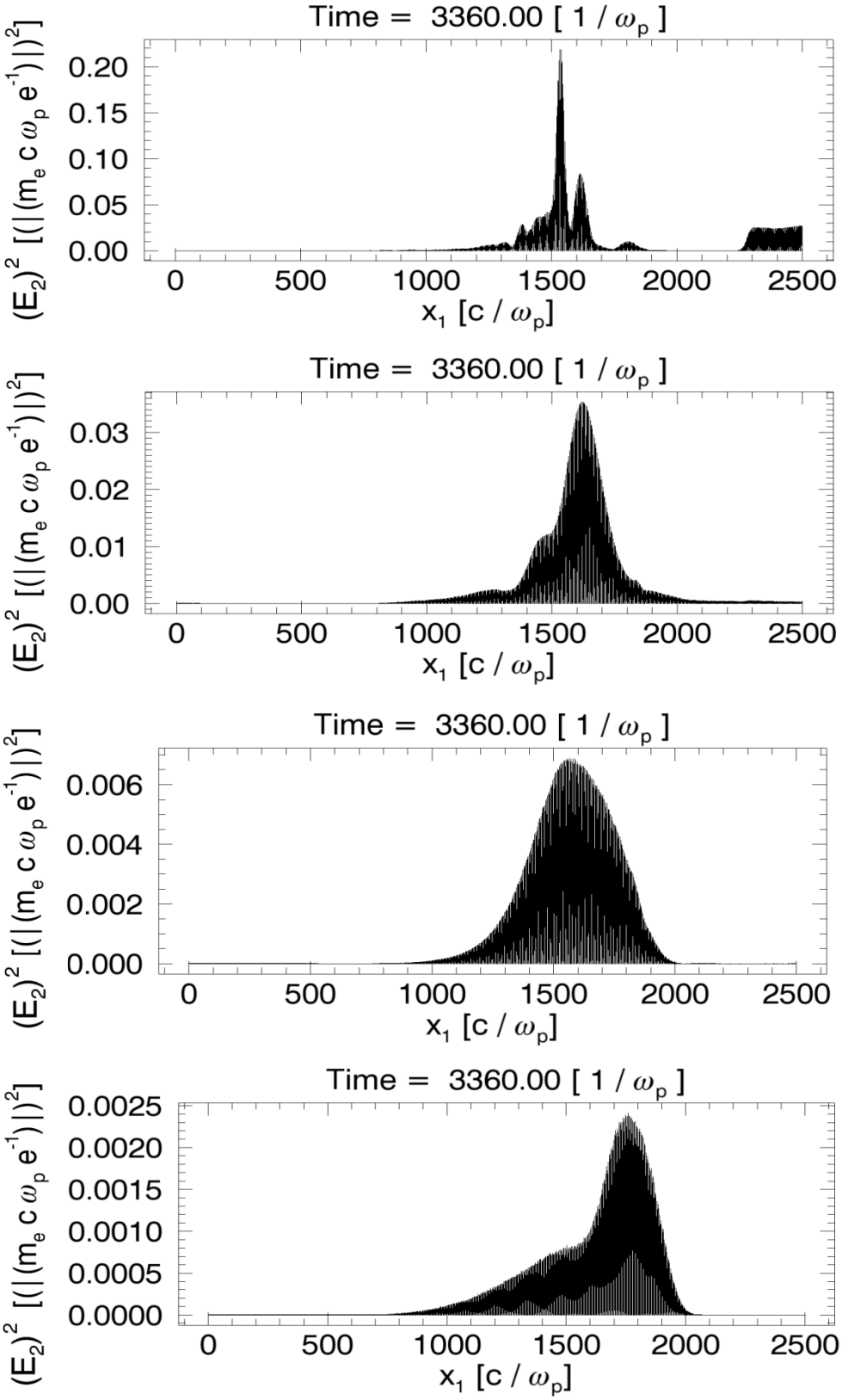

Figure 5.2.1 – Plot of the square of the transverse electric field to illustrate the dependence of probe duration on pump intensity. Top-bottom: probe pulse for a pump intensity of 1.0×10^{16}, 3.0×10^{15}, 1.0×10^{15} and 3.0×10^{14} Wcm^{-2}.

5.3 Optimal probe duration considerations

From the self-similar theory [Malkin, Shvets and Fisch 1999] [Andreev et al. 2006] and numerical simulations [Kim et al. 2003], it follows that an ideal self-similar probe also has a well-defined optimal duration at all times which is dependent on its initial intensity. Following from this, if the probe has a non-zero amplitude, given by a_1, when it meets the pump at $t = 0$, it should also have a well-defined optimal duration τ_{opt} which fits the self-similar evolution of the probe.

It is important to launch a probe with a duration close to τ_{opt}: although a non-ideal probe will attempt to reshape itself into an ideal probe (since the self-similar solution is an "attractor" [Malkin, Shvets and Fisch 1999]), this reshaping could extend the linear stage of the pump-probe interaction [Malkin, Shvets and Fisch 1999] [Andreev et al. 2006] [Kim et al.. 2003], lead to a longer start-up period [Trines et al. 2011b] or even cause probe growth to saturate prematurely [Ping et al. 2009]. All of these reduce the efficiency of the amplification. For Brillouin amplification, this matters even more than for Raman amplification because of the lower growth rates involved. Thus, knowledge of the optimal initial duration of the probe will improve the design of future simulations and experiments.

Since the growing probe already has a finite energy content when it meets the pump at $t = 0$, it is necessary to introduce a time offset t_0. Firstly by rewriting equation 5.1.7 as:

$$\gamma_B \tau_{pr} \sqrt{\gamma_B (t_0 + t)} = \sqrt{g/\eta}\, \xi_B \tag{5.3.1}$$

and using the energy balance equation:

$$a_{pr}^2 \tau_{pr} = 2\eta a_0^2 (t_0 + t) \tag{5.3.2}$$

We observe that $a_{pr} = a_1$ and $\tau_{pr} = \tau_{opt}$ at $t = 0$, so the characteristic growth time, $t_0 = \tau_{opt} a_1^2 / 2\eta a_0^2$. Inserting this into (5.3.1) at $t = 0$ yields:

$$\tau_{opt} = \frac{1}{\gamma_B}\left(\frac{\sqrt{g}\xi_B}{\sqrt{2}}\ \frac{a_0}{a_1}\right)^{2/3} \propto a_1^{-2/3} \tag{5.3.3}$$

as the optimal duration for the probe pulse.

From ref. [Andreev et al. 2006], we find the following scalings:

$$\tau_{pr} = \tau_{opt}(1 + t/t_0)^{-1/2} \tag{5.3.4}$$

$$a_{pr} = a_1(1 + t/t_0)^{3/4} \tag{5.3.5}$$

It can be seen that τ_{opt} only depends on a_1 not on a_0 or η. The probes evolution is governed by t_0, however, which does depend on both a_0 and η.

5.4 Importance of choosing the correct initial probe conditions

To illustrate this behaviour for Brillouin amplification, two simulations with initial probe durations of 100fs and 400fs were conducted. In these simulations, the initial pump and probe intensities were $1.0\text{x}10^{15}$ Wcm^{-2} and $1.0\text{x}10^{14}$ Wcm^{-2}, respectively, with each of the other parameters the same as in section 5.2. The results of these simulations are displayed in Figure 5.4.1 and compared with the optimum probe intensity, calculated via equation 5.3.3, where τ_{opt} = 0.56ps for a probe intensity of $1.0\text{x}10^{14}$ Wcm^{-2}.

In the case of the 400fs probe it can be seen that the amplification process starts immediately and a peak intensity of $6.2\text{x}10^{15}$ Wcm^{-2} is reached. In the case of the 100fs probe, however, it is seen that the onset of the amplification process is delayed. The effect of this delay can be seen in the peak intensity of the seed pulse where the final intensity only reaches around 60% of the amplitude achieved for the 400fs pulse. In both cases, the probe stretches to acquire the optimal self-similar duration

for its intensity, but for the 100fs probe this takes much more time, taking away from the amplification process and making the scattering less efficient.

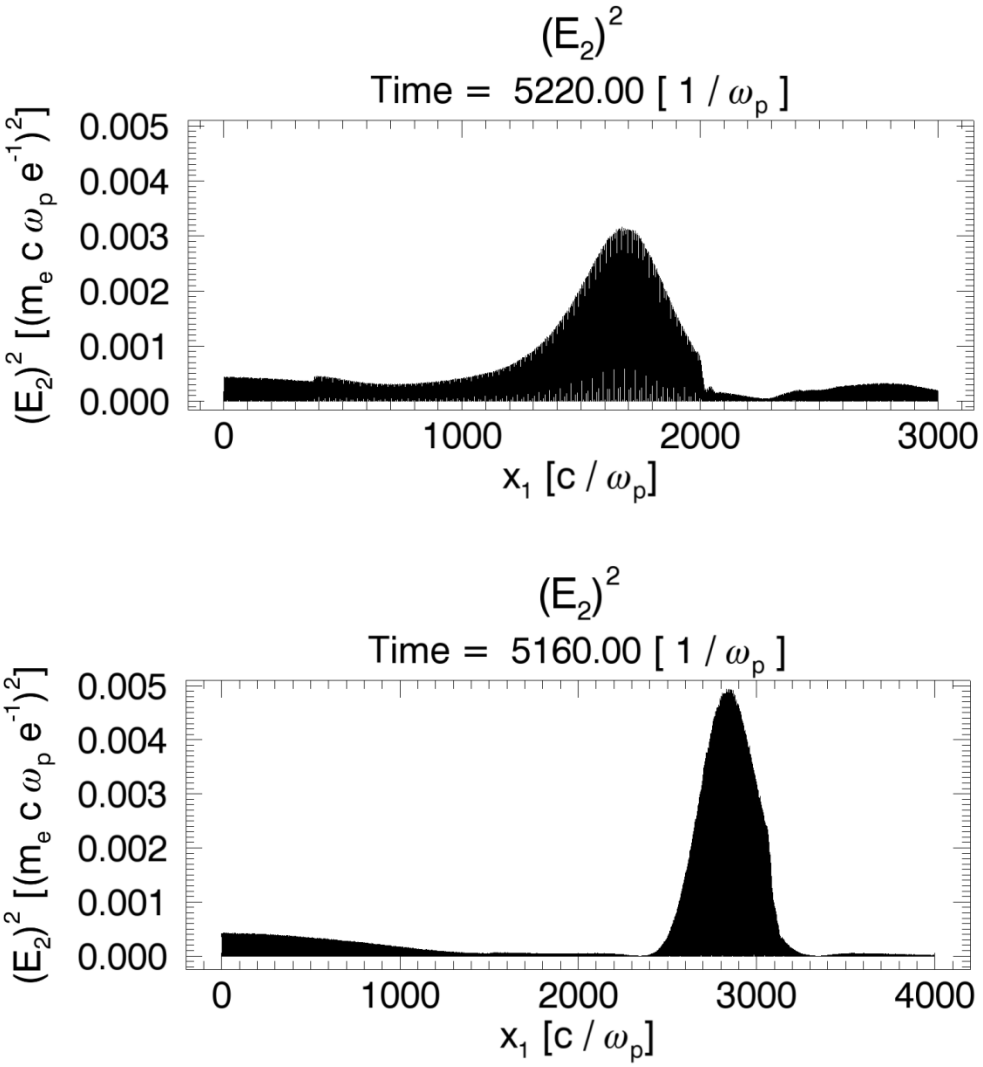

Figure 5.4.1 – Importance of choosing the correct initial probe duration. Top: snapshot of 100fs probe after interaction. Bottom: Snapshot of 400fs probe after interaction. The amplitude of the seed pulse is higher and a greater proportion of the pump pulse is depleted by using the longer 400fs pulse length as opposed to the shorter 100fs duration probe pulse.

5.5 Scalability of SBS in parameter space

5.5.1 Summary of simulation data

In order for stimulated Brillouin scattering to be used effectively for a wide range of practical applications it is necessary to investigate the range of laser-plasma parameters where seed laser amplification is exhibited. This allows determination of the regimes under which this energy transfer technique could potentially be employed.

A summary of the simulations conducted so far throughout this thesis can be seen in table 1. The parameters for each set of results are shown, including: the initial pump (a_0) and probe (a_1) amplitudes, initial pump (t_{pu}) and initial and final probe ($t_{pr,i}$ and $t_{pr,f}$) duration, the energy transfer efficiency and $\xi_B = \gamma_B \tau_{pr} \sqrt{\gamma_B \tau_{pu}}$ to verify compliance with the self-similar theory. Simulation I corresponds to the simulation presented in section 4.5 where collisional processes were first accounted for, simulations II, III, IV and V correspond to the results presented in section 5.2 and simulations VI and VII relate to the results presented on the importance of the initial seed duration, as seen in section 5.4.

	I	II	III	IV	V	VI	VII
ao	0.0855	0.0855	0.0468	0.027	0.015	0.027	0.027
a1	0.027	0.027	0.027	0.027	0.027	0.086	0.086
t_{pu} (ps)	0.75	1.44	1.44	1.44	1.44	2.3	2.3
$t_{pr,i}$ (fs)	100	200	200	200	200	100	400
$t_{pr,f}$ (fs)	194	100	341	854	1024	485	336
Eff. (%)	38	57	44	-	-	25	32
ξ_B	3.7	5.4	5.1	7.4	2.1	5.2	3.6

Table 1 – Summary of simulation results using static window

From the results presented above, is can be seen that simulations I, II, III, VI and VII each have probe pulses which have had time to evolve sufficiently, such that they are adequately described by the self-similar theory. This can be seen from the values of ξ_B localised around the idealised probe value of 5, as detailed previously by (5.3.7), with corresponding energy transfer efficiencies ranging from 25% to 57%. Simulations IV and V, however, do not have fully self-similar probes as can be seen from their values for ξ_B which fall far from the idealised value predicted, therefore efficiency measurements for this data cannot be accurately determined.

The most impressive result is obtained in simulation II where an intensity gain in the seed pulse of around 60 times is realised. This is due to a number of reasons: Firstly, the initial probe duration is closest to the optimum probe duration as calculated via (5.3.3); and secondly the probe has had adequate time to become sufficiently well-developed such that it is very well described by the self-similar theory. This is reflected in the self-similar parameter being close to the predicted value of 5 and the highest efficiency seen throughout the set of numerical simulation data presented.

The importance of choosing the initial seed intensity is further highlighted by comparison of the results obtained from simulations I and II, with the results previously discussed in section 5.4, corresponding to simulation numbers VI and VII. It can be seen that doubling the duration of the seed pulse from simulation I to II, such that the initial probe more closely resembles the conditions describing an optimum probe pulse, equates to an efficiency boost of almost 20% and an increase in ξ_B such that it more closely resembles the idealised solution. A similar result, although not as dramatic, is seen upon comparison of the efficiencies and self-similar parameters from simulations VI and VII. It can be seen as the probe duration is altered from VI to VII, again to more closely resemble an “ideal” probe; an increase in efficiency is seen here also.

Another interesting feature of SBS can be seen upon comparison of simulations II and III and IV and V, respectively. In each of these sets of simulations only the pump intensity has been altered between each pair. This allows a comparison to be drawn between intensity and plasma amplifier length. Firstly looking at the results from simulations II and III it can be seen that as the pump intensity is reduced, while

all other parameters are kept constant, a significant reduction in the efficiency of the process is observed. This indicates that that a drop in pump intensity is linked to less growth for the same plasma length, therefore indicating that when the pump intensity is lowered adjustments to the plasma amplifier are required. Upon contrast of IV and V, where the intensities of both pulses is reduced from that of II and III, it can be seen that the drop in intensity from simulation V to simulation IV equates to an inadequate description by the self-similar theory of the evolution of the seed. This is due to the fact that the seed has simply not developed sufficiently such that its behaviour is fully self- similar in nature.

There are many potential reasons why some of the values of ξ_B calculated for these simulations fall far from the idealised value of 5.0 as predicted from the theory. These include the fact that the scaling calculations do not account for the presence of laser-plasma instabilities which could of course be present in results obtained through the PiC simulations and also the interaction length simulated may not be sufficiently long for the pulse to be fully self-similar in all cases which is also not accounted for in the theoretical analysis either.

5.5.2 Scalability of SBS energy transfer mechanism

In this section the effect of seed length and amplifier length are further examined via the following simulations. Three distinct cases, A, B and C, are examined. In each of the simulations the pump intensity was fixed at $1.0\text{x}10^{15}\text{Wcm}^{-2}$ and the seed intensity was set to $1.0\text{x}10^{14}\text{Wcm}^{-2}$. In case A the seed duration is 100fs and the amplifier length $650\omega_p^{-1}$, in case B the plasma amplifier length was increased by a factor of four and in case C the plasma length was fixed as in simulation B and the seed duration was extended to 400fs. It should also be noted here that due to the way the simulations are constructed, an increase in the plasma amplifier length means a corresponding increase in the pump laser duration.

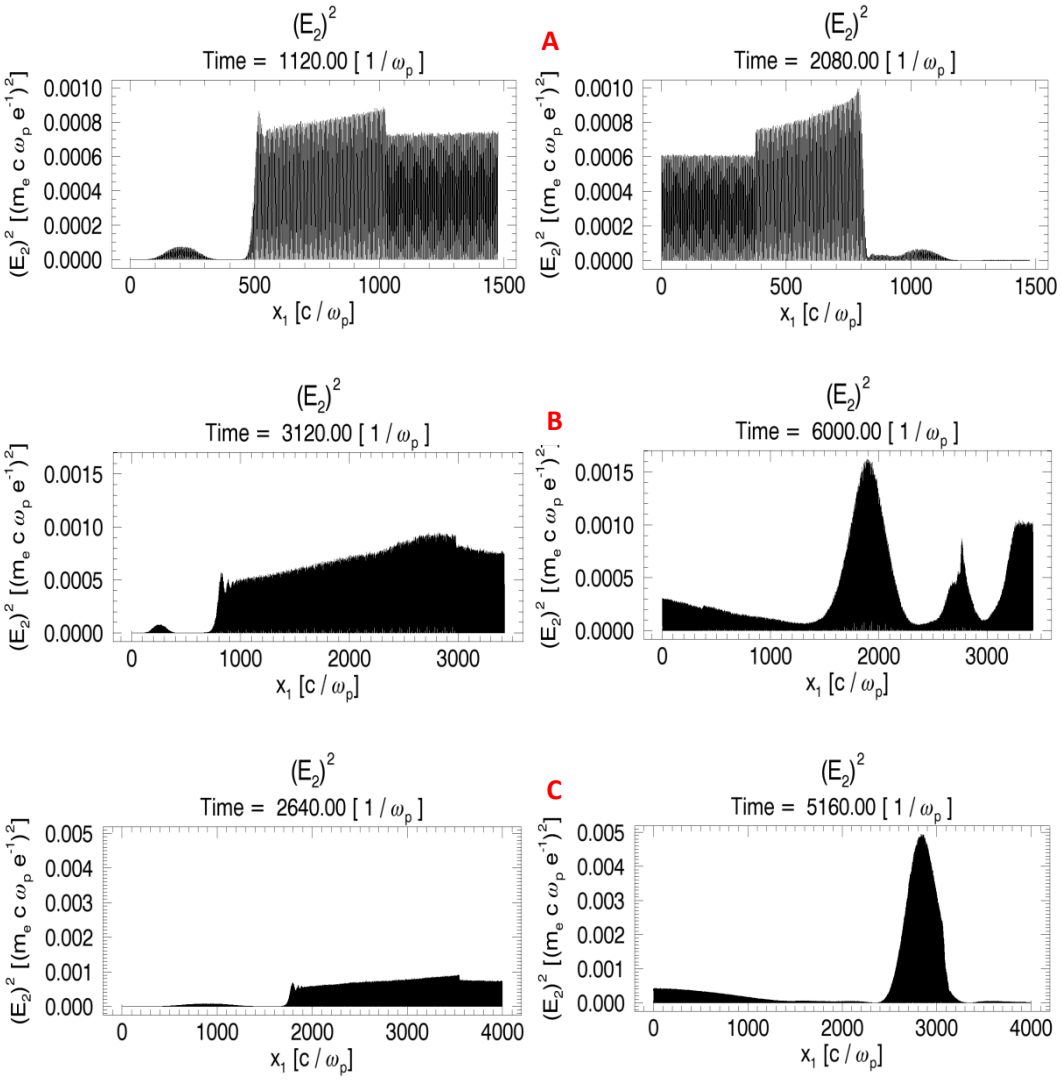

Figure 5.5.2.1A, B, C – Initial (LHS) and final (RHS) seed pulses for the cases A, B and C, respectively.

Upon examination of the top set of data in figure 5.5.2.1, relating to simulation A, it is seen that energy transfer via SBS has not occurred and as a result the seed has not undergone amplification. Of particular interest is that the amplifier length used to perform this simulation is the same as was used to obtain the most efficient amplification as previously seen in simulation II. This gives an early indication that plasma amplifier length, in addition to seed duration, is a key parameter for optimisation of the energy transfer process via stimulated Brillouin scattering. This effect is seen in the second set of data relating to simulation B where it is observed

that the seed has been amplified as a direct result of increasing the plasma amplifier length. The efficiency of this process, however, was found to be very low at 8% but the self-similar parameter showed that the pulse evolution was well developed with a value of ξ_B = 4.4 obtained. Finally, the results from simulation C show that further amplification of the seed pulse is obtained by increasing the seed duration in addition to extending the plasma amplifier length. As a result of this the efficiency of the simulation dramatically increased to 33% with the self-similar parameters still showing good agreement with the theory at ξ_B = 4.3.

Upon comparison with the results obtained from simulations A, B and C with simulation II it is confirmed that in order for efficient amplification by SBS to be achieved at lower intensities, an increase in the plasma amplifier length in addition to an extension of the seed pulse duration is required, as predicted by the self-similar theory. This is due to the fact that SBS with less intense lasers takes longer to grow as the scattering process is not driven as hard as in cases when the process is strongly driven by a high intensity pump pulse. Conversely, following directly from this analysis, the opposite scaling is true when moving from lower intensities to higher intensity pulses.

The approximate form of the scaling of the seed pulse duration can be obtained via the self-similar theory. As:

$$a_0 \omega_{pi} \tau_{pr} \sqrt{\omega_0 \tau_{pu}} = constant \qquad (5.5.2.1)$$

If we assume that the laser frequency ω_0, is a constant, ω_{pi} is also fixed and that τ_{pu} is constant then we find that:

$$\tau_{pr} \sim \frac{1}{a_0} \sim \frac{1}{\sqrt{I}} \qquad (5.5.2.2)$$

where I is the pump laser intensity.

It can therefore be deduced that if the pump laser intensity is reduced by an order of magnitude then the seed duration should be increased by a factor of ~ 3.1.

5.5.3 Upper and lower intensity bounds for energy transfer

As energy transfer via SBS has been shown to occur at various laser intensities by appropriate scaling of the laser-plasma parameters, it is now pertinent to examine the upper and lower intensity bounds where this energy transfer mechanism can be applied in plasma.

It has already been seen that seed amplification is observed in simulations with pump intensities ranging from $1x10^{16}Wcm^{-2}$ to $3x10^{14}Wcm^{-2}$. However when the pump intensity is raised above this upper limit of $1x10^{16}Wcm^{-2}$, parasitic stimulated Brillouin backscattering from the pump laser can be seen, leading to a large scale disruption to the coherence of the beam. Figure 5.5.3.1 shows the effect of a pump beam with an intensity of $1x10^{17}Wcm^{-2}$ and a seed laser of $1x10^{16}Wcm^{-2}$ on the energy transfer process.

At $480\omega_p^{-1}$ it can be seen that the pump beam is uniform and shows no signs of premature scattering or laser-plasma instabilities, however as it propagates further into the plasma, at $720\omega_p^{-1}$ the initial signs of pump instability can be seen. This initial disturbance then begins to grow and severe parasitic backscattering of the pump laser field is seen at $1120\omega_p^{-1}$, just as the seed laser enters the plasma. As the seed propagates through the pump field it can be seen that the pump laser is too unstable and is already significantly depleted of energy such that energy transfer between the pulses does not occur. It can therefore be said that the upper intensity limit for stimulated Brillouin scattering to occur in plasmas is close to a pump intensity of $1x10^{16}Wcm^{-2}$. The determination of the precise intensity at which SBS can no longer efficiently operate would require detailed analysis of the range between $1x10^{16}Wcm^{-2}$ and $1x10^{17}Wcm^{-2}$.

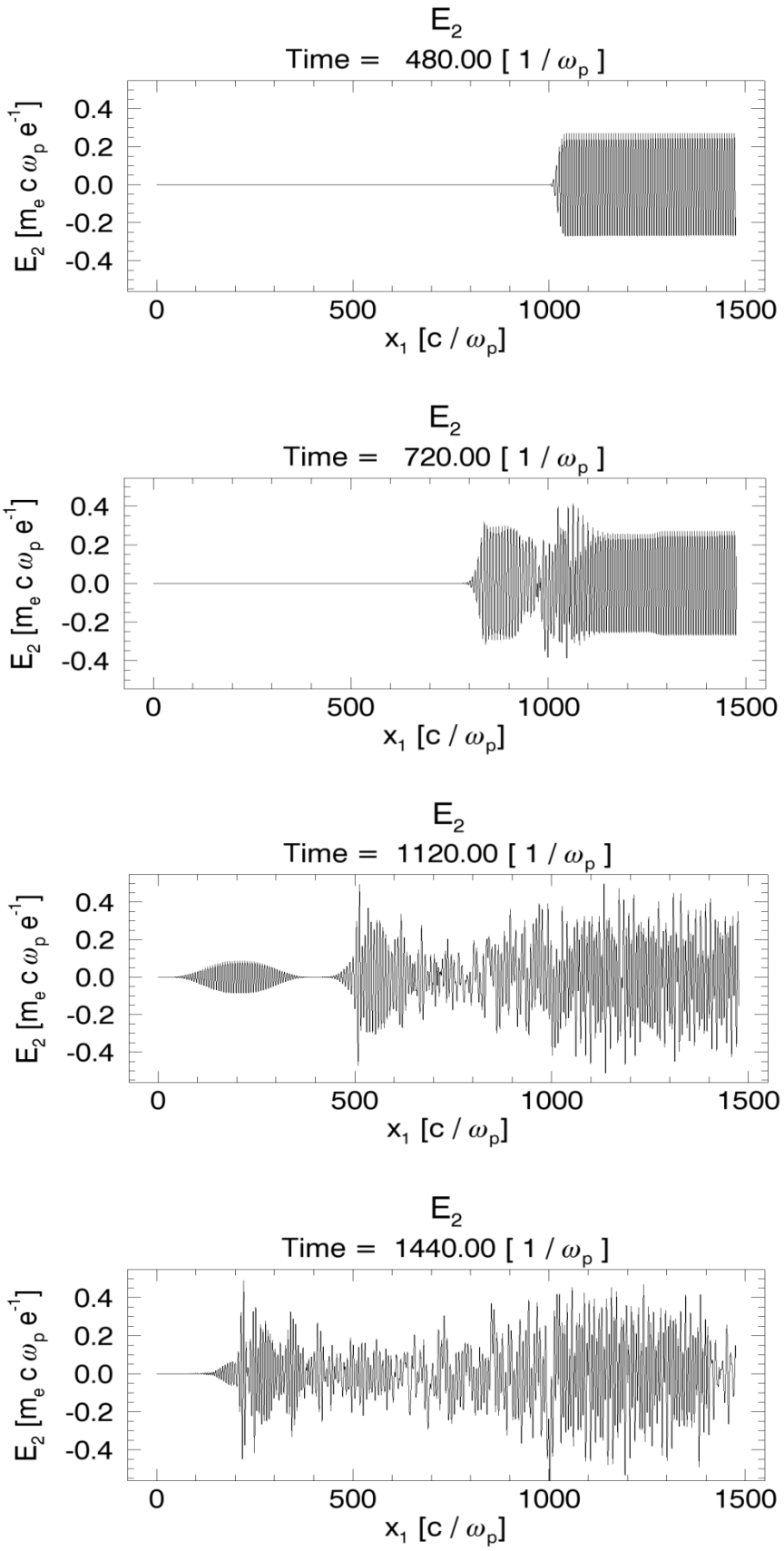

Figure 5.5.2 – Seed and pump pulse evolution at a pump intensity of $1x10^{17}Wcm^{-2}$

Determination of the lower bounds for the pump intensity, in order to realise energy transfer via SBS, are much more difficult to determine than the upper bounds in a static window simulation configuration. This is due to the fact that, as already shown in 5.5.2, as the pump intensity is reduced a substantial increase in the length of the plasma amplifier is required which has the effect of significantly increasing the run time of the calculation.

Initial signs of seed growth at pump intensities of $3x10^{14}Wcm^{-2}$ have already been shown, in section 5.2, however when the pump intensity is reduced to $1x10^{14}Wcm^{-2}$ it can be seen that the energy transfer process fails to initiate. The results of this study, for a pump intensity of $1x10^{14}Wcm^{-2}$ and a seed intensity of $1x10^{13}Wcm^{-2}$, are shown in figure 5.5.3. The plasma amplifier length in this case is set to such a length that this simulation took over three weeks on 96 processors to complete.

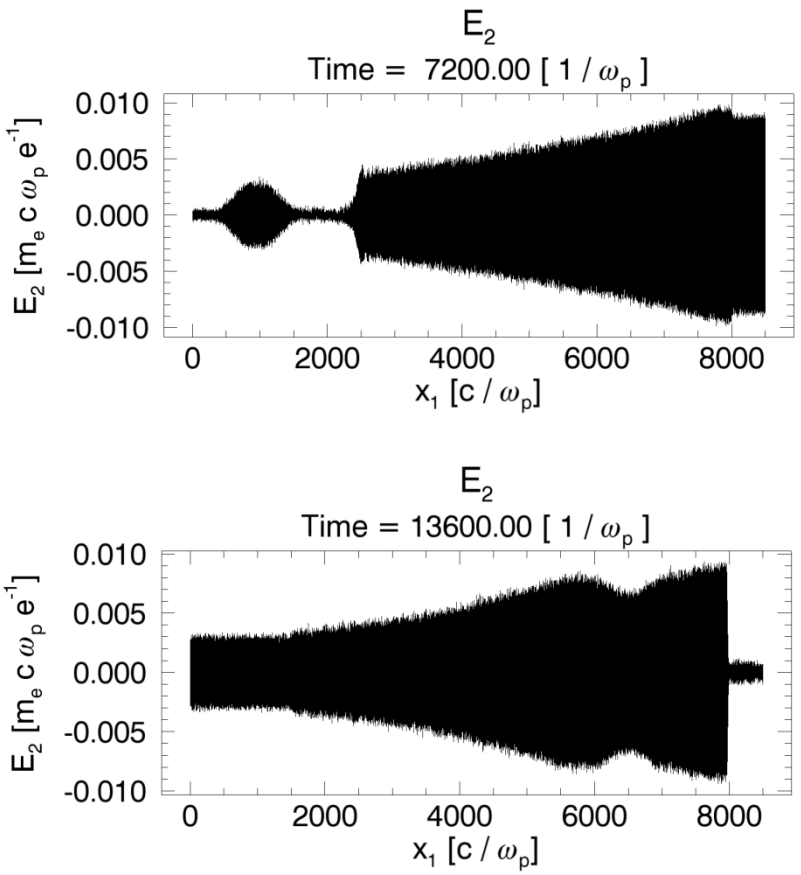

Figure 5.5.3 – Seed and pump pulse evolution at low intensity

In the first snapshot of figure 5.5.3 at $7200\omega_p^{-1}$ it can be seen that the seed pulse is introduced after the pump pulse has traversed through a long plasma amplifier. After an extended duration in time it can be seen from the second snapshot of figure 5.3.3 that the seed pulse has traversed a significant distance within the plasma amplifier but there appears to be no significant interaction with the pump field and no growth of the seed pulse. By analysing the Fourier spectra of the transverse and longitudinal electric fields we can determine whether scattering via SBS is occurring.

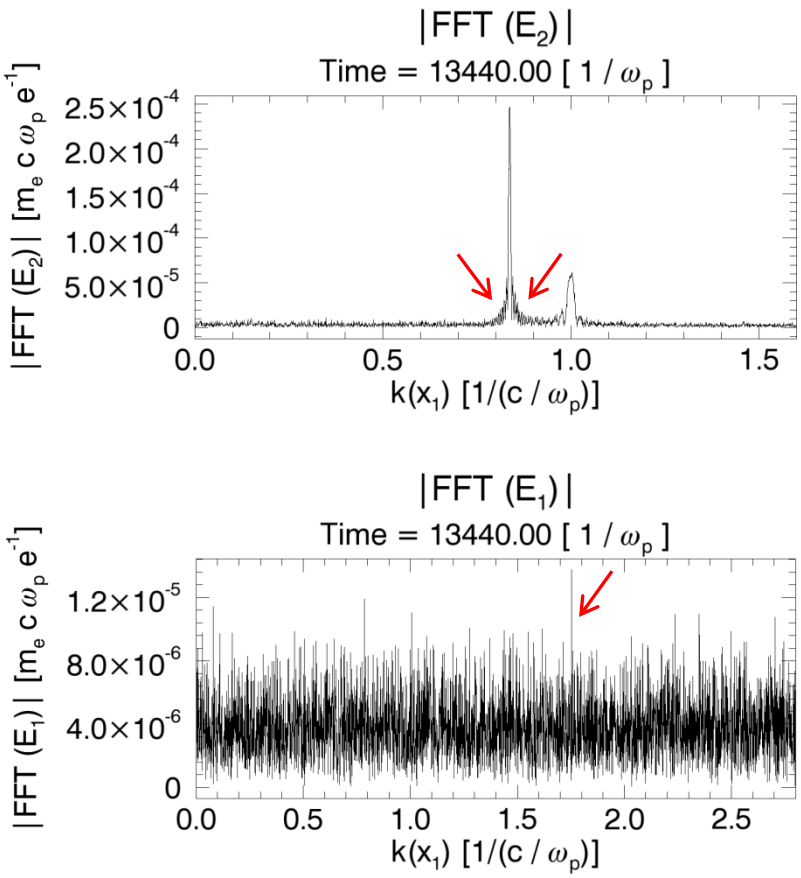

Figure 5.5.4 – Fourier spectra of the transverse and longitudinal electric fields, respectively.

The first plot in figure 5.5.4 shows a Fourier transform of the transverse electric field. Some initial signs of scattering in the pump field can be seen and are indicated with a red arrow; however this scattering is very weak. Analysis of the Fourier

transform of the longitudinal electric field shows very little in the way of spectral behaviour and no clear indication of a well-developed ion acoustic wave. It can be seen however, amongst the background noise, that there is one wavenumber at which the amplitude of the signal is highest, this corresponds to the approximate wavenumber at which we would expect to see a spectral peak for a SBS generated ion acoustic wave for the simulation parameters used. It is therefore clear that in order to have conclusive evidence for the scalability of SBS to such low intensities as this, plasma amplifiers of much longer length than is reasonably practical in a static window simulation are required.

For the simulations presented here it is clear that limits are reached as to what can be run in a sensible time frame using a static simulation window. This is particularly true for the low intensity simulations where extended amplifier lengths and seed durations are essential for energy transfer from pump to seed to be realised. Therefore further work is needed to see whether the amplification factor of the seed pulses can be increased when the amplifier length is extended far beyond that which is practical in a static window setup. It is also pertinent to determine whether the most impressive of amplification factors obtained, particularly that of simulation II, can be further boosted by an extended amplifier length also. These points are investigated in more detail in 5.6 using OSIRIS' moving window feature.

5.6 Moving window simulations for energy transfer optimisation

With the implementation of the moving window feature in OSIRIS it is now possible to simulate very long interaction lengths as the simulation box is set to follow only the region of the simulation associated with the evolution of the seed pulse. Thus, meaning that the rest of the simulation volume is ignored and does not need to be computed. To date there are no published results of this nature with any other numerical simulation code.

In OSIRIS the mesh is kept stationary with respect to the background and as the simulation steps forward in time new particles and fields are created at the leading edge of the window and the particles and fields already in the box are shifted one cell to the left (for a window moving from left to right). When the contents of the mesh reach the leftmost cell, marking the end of the simulation window, they are discarded. For the simulation results shown in this thesis the seed pulse was launched backwards from the leading edge of the moving window, where the window moves from left to right through the simulation geometry.

The parameters for the simulations detailed in this part of the thesis (section: 5.6.1) are set as in section 5.2, in accordance with the static window simulations. In these cases, however, the simulation box is scaled to the seed duration and the plasma amplifier lengths and pump durations have been significantly extended to take full advantage of the moving window.

5.6.1 The four distinct stages of seed amplification via SBS

In order to determine the maximum amplification factor that a seed laser can reach, via SBS, for a given set of parameters the seed intensity should be measured when the pulse is fully developed, i.e. the seed should be adequately described by the self-similar theory. The observation of this fully self-similar behaviour requires the observation of the seed laser pulse over a significant duration of time, further highlighting the requirement for numerical simulations with an integrated moving window feature.

Figure 5.6.1 details the self-similar evolution of a seed pulse where the four distinct stages of the amplification process are shown for pump and seed intensities of $1x10^{16}Wcm^{-2}$ and $1x10^{15}Wcm^{-2}$, respectively, with the OSIRIS moving window feature enabled.

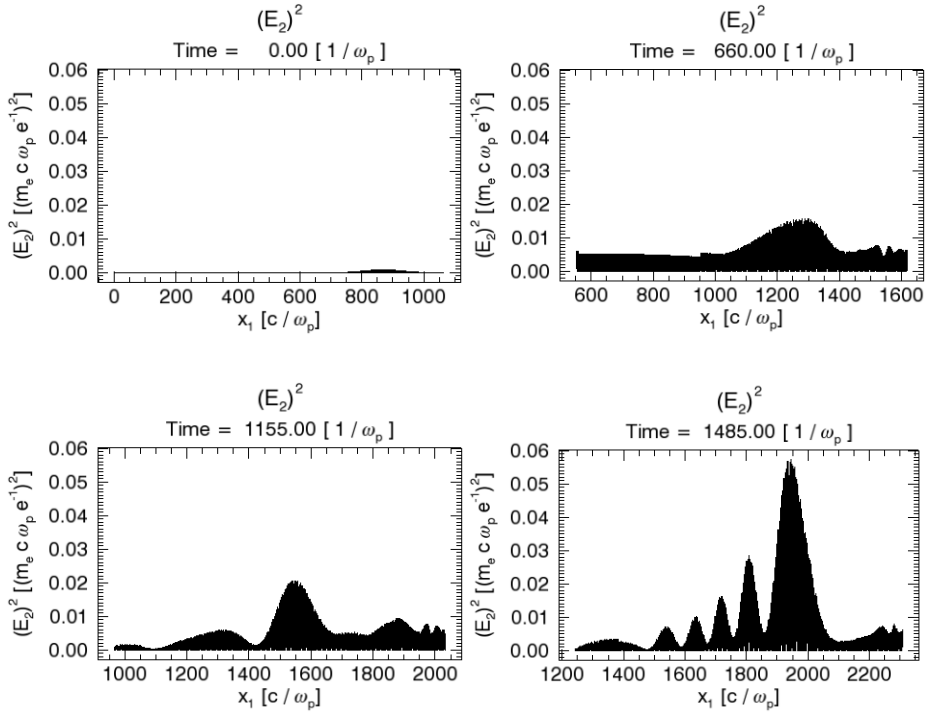

Figure 5.6.1.1a, b, c, d – The four stages of seed amplification via SBS

From the first snapshot of figure 5.6.1.1 it can be seen that the seed pulse is injected into the plasma volume just before the injection of the long pump laser. At $660\omega_p^{-1}$ the pulse begins to exhibit signs of broadening with a small amount of amplification also noted, and then at $1150\omega_p^{-1}$ the seed is compressed as it is amplified further. Finally at $1485\omega_p^{-1}$ the seed undergoes significant amplification and compression with the pulse modulating into a train of pulses of reducing amplitude demonstrating that the self-similar solution is an "attractor". This four stage process is very similar to that identified with Raman scattering and reported by Kim et al. [Kim et al. 2003].

5.6.2 Amplification of seed pulses via OSIRIS moving window

An extensive investigation of SBS has already been conducted in section 5.5 where it was noted that efficient amplification of seed laser pulses via SBS is observed at high intensities but not at low laser intensities, with a static window implementation in the numerical simulations. In this section, however, the results of two simulations where

laser amplification can be seen to occur at low pump and seed intensities of $1x10^{15}Wcm^{-2}$ and $1x10^{14}Wcm^{-2}$ and $1x10^{14}Wcm^{-2}$ and $1x10^{13}Wcm^{-2}$, shown in figures 5.6.2.1 and 5.6.2.2, respectively, are presented where the OSIRIS moving window has been enabled.

Figure 5.6.2.1a and 5.6.2.1b show the initial probe amplitude and the final probe amplitude after amplification for the higher of the two intensities tested with the moving window implementation. It can clearly be seen that the seed pulse has been significantly amplified with respect to its initial amplitude where the efficiency of this process was found to be 26%. This efficiency, although lower than the efficiencies achievable for the high intensity cases examined in table 1, proves that amplification of laser beams via SBS is achievable at laser intensities of $1x10^{14}Wcm^{-2}$.

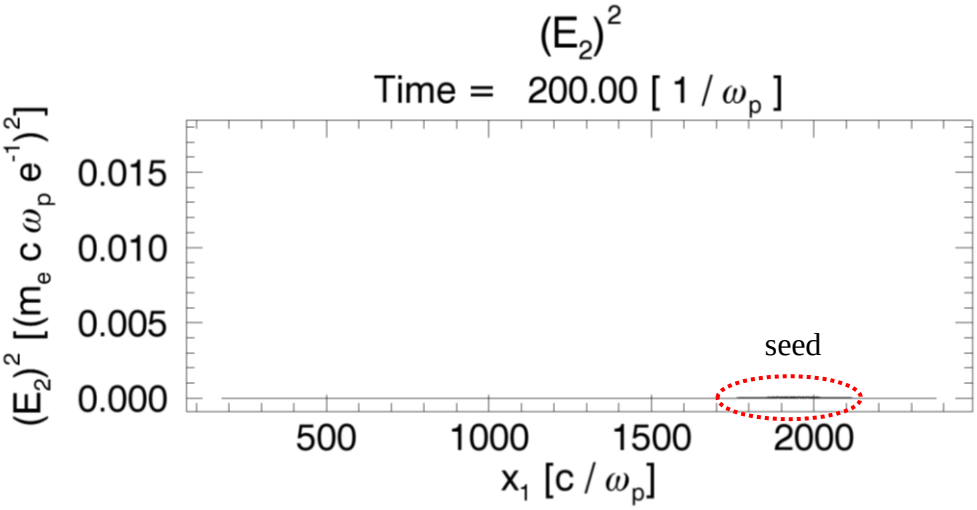

Figure 5.6.2.1a – Square of the transverse electric field of the initial probe pulse of intensity $1x10^{14}Wcm^{-2}$

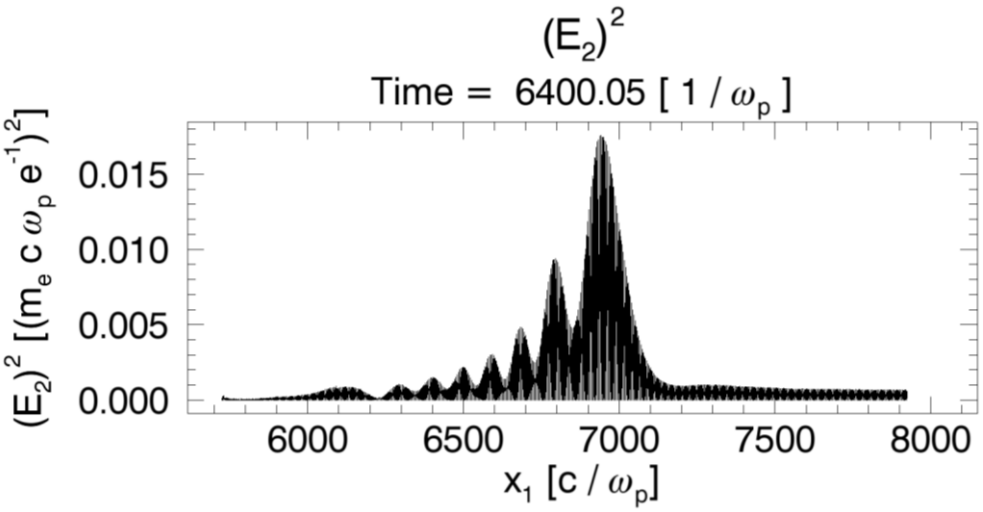

Figure 5.6.2.1b – Square of the transverse electric field of an amplified probe pulse obtained by pump and seed lasers of intensity $1x10^{15}Wcm^{-2}$ and $1x10^{14}Wcm^{-2}$, respectively.

Figures 5.6.2.2a and 5.6.2.2b detail the initial and amplified probe pulses, respectively, for the case of a pump laser of $1x10^{14}Wcm^{-2}$ and a seed laser of intensity $1x10^{13}Wcm^{-2}$. It can be seen, similarly to the case examined above, that the seed has been significantly amplified with respect to its initial intensity. It is also noted however that the final amplified seed occurs after a much longer time and after it has propagated a much greater distance through the plasma amplifier than the higher intensity case examined in figure 5.6.2.1. This causes the efficiency of the Brillouin energy transfer process to drop significantly, resulting in a very poor efficiency of 2% for this parameter set.

Numerical investigations of SBS for laser intensities below the $1x10^{13}Wcm^{-2}$ seed value concluded that although some growth of the initial seed pulse is seen to occur, this occurs at a very low level and after propagation through an extended volume of plasma which limits the efficiency of the process. It is therefore unlikely that laser intensities of $1x10^{13}Wcm^{-2}$ will prove to be useful for laser amplification techniques via SBS.

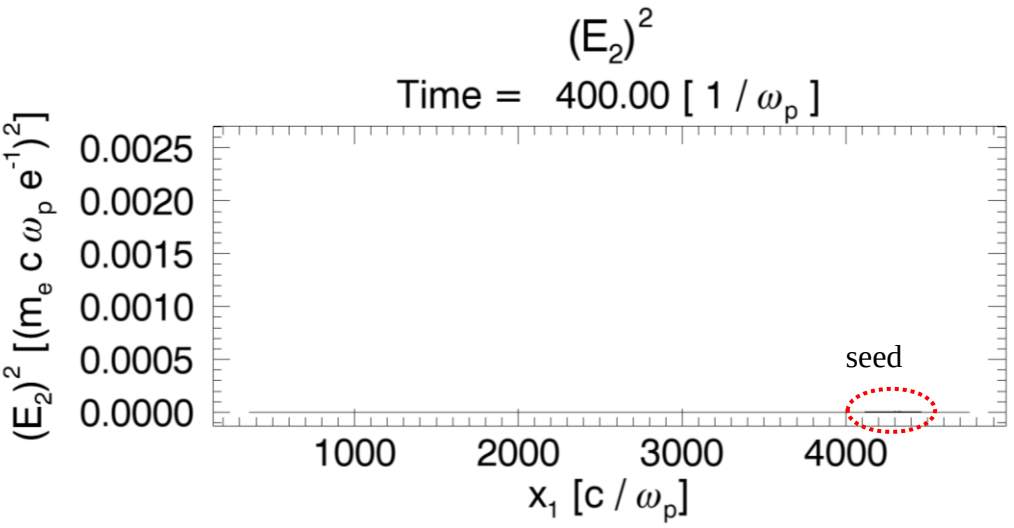

Figure 5.6.2.2b – Square of the transverse electric field of an amplified probe pulse obtained by pump and seed lasers of intensity $1x10^{14}Wcm^{-2}$ and $1x10^{13}Wcm^{-2}$, respectively.

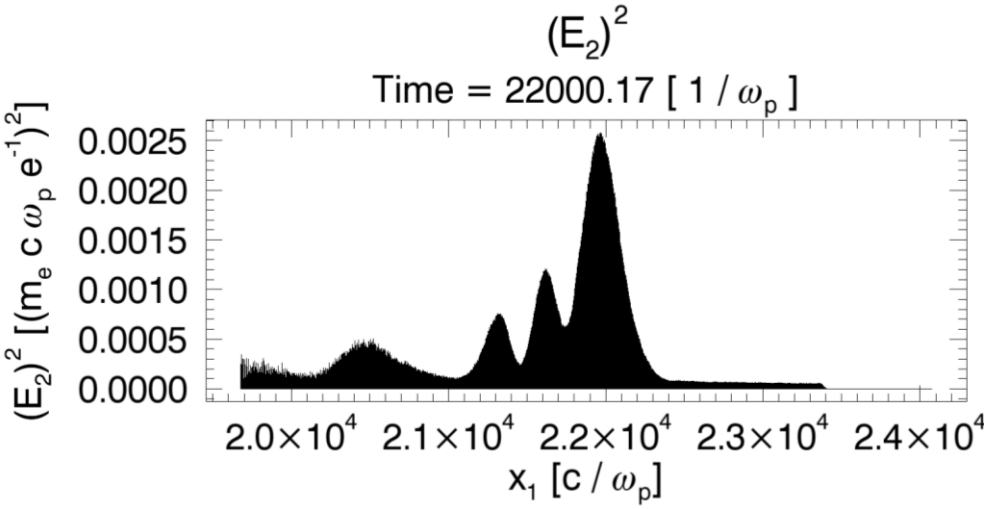

Figure 5.6.2.2 – Square of the transverse electric field of a probe pulse obtained by pump and seed lasers of intensity $1x10^{14}Wcm^{-2}$ and $1x10^{13}Wcm^{-2}$, respectively.

For reference, a summary of the simulation parameters used to calculate the SBS efficiencies for both sets of results presented in this section are detailed in table 2 and labelled as VIII and IX, respectively.

5.6.3 Maximum seed amplification obtainable by SBS via OSIRIS moving window

It has already been demonstrated throughout this chapter that stable, efficient amplification of laser beams can be obtained throughout a wide region of parameter space; however it is also possible to achieve much increased levels of amplification if a more unstable configuration is assumed. The plots below provide an example of this and detail the maximum amplification obtainable from the parameter set in case II, as examined previously. In the results presented below however, the simulation has been allowed to progress in time from a previously stable configuration to a much more unstable configuration where the ion acoustic wave undergoes wavebreaking, just before the energy transfer process between pump and seed saturates.

Figure 5.6.3.1a and 5.6.3.1b detail the square of the electric field for the amplified seed pulse in the stable and unstable regimes, respectively. It can be seen that the pulse integrity in plot a is much more favourable than in plot b, however the amplitude of plot b is around 4 times higher than that exhibited in plot a. This shows the flexibility of SBS to a wide variety of applications: If maintaining a longer output pulse and excellent pulse integrity is the most important consideration then the amplified signal should be harvested before the process enters the unstable regime but on the other hand if the peak power is the most desirable pulse characteristic then the laser should be allowed to continue to traverse the plasma amplifier well into the unstable regime before it is collected.

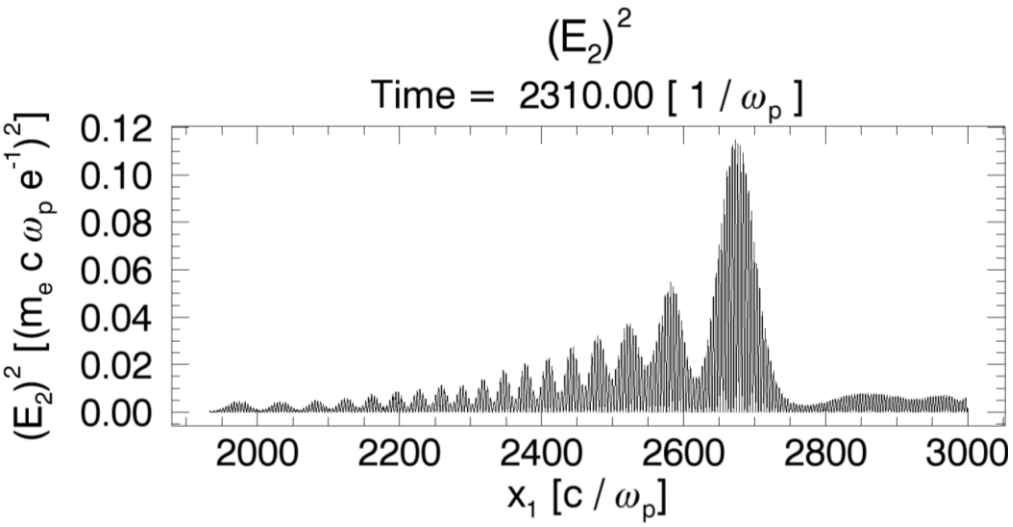

Figure 5.6.3.1a – Peak amplitude reached by pump and seed lasers of intensity $1x10^{16}Wcm^{-2}$ and $1x10^{15}Wcm^{-2}$, respectively, in a stable configuration

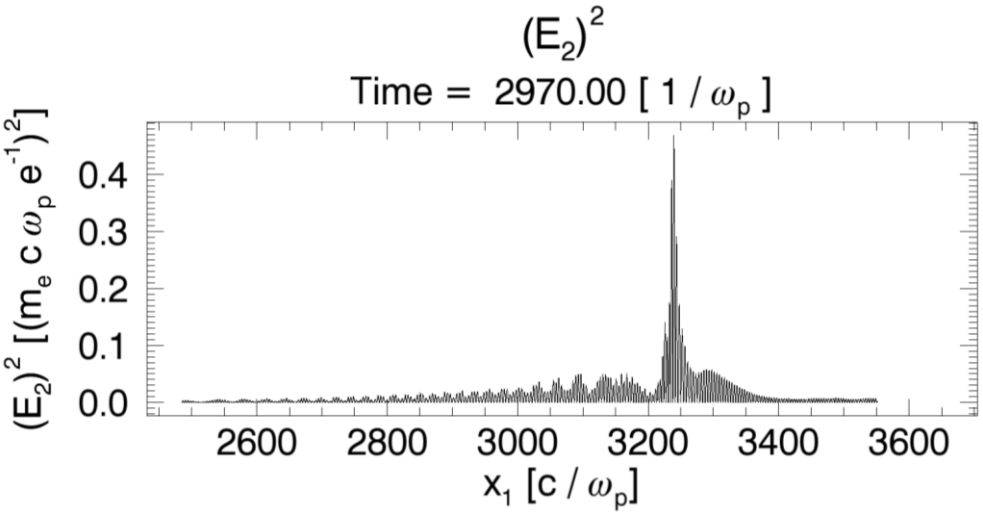

Figure 5.6.3.1b – Peak amplitude reached by pump and seed lasers of intensity $1x10^{16}Wcm^{-2}$ and $1x10^{15}Wcm^{-2}$, respectively, in an unstable configuration

The transition from the stable regime to a regime which is considered unstable is attributed to the excitation and growth of the ion acoustic wave. Figures 5.6.3.2.a and 5.6.3.2.b detail the growth of the ion acoustic wave associated with stimulated Brillouin scattering via phase space plots, for the stable and unstable regimes, respectively.

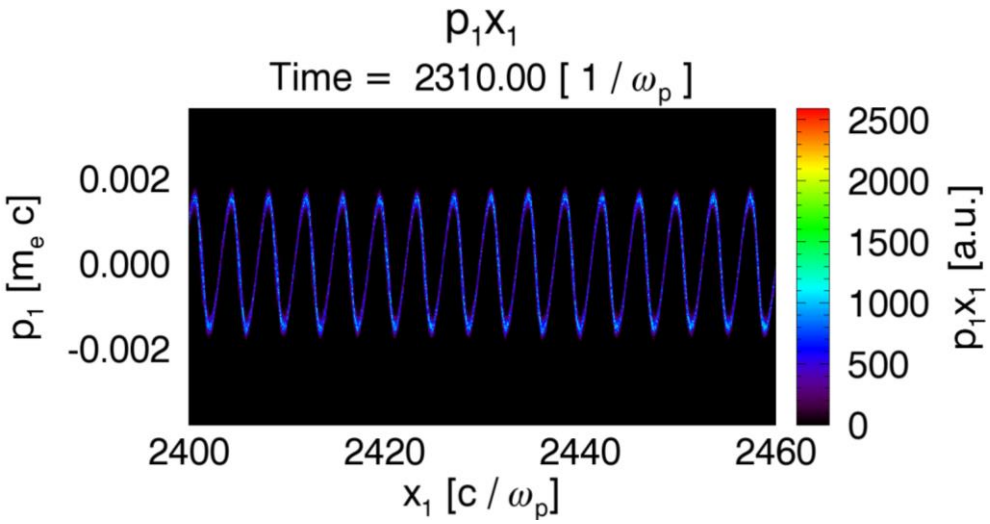

Figure 5.6.3.2a – Peak amplitude of the ion acoustic waves in the stable configuration

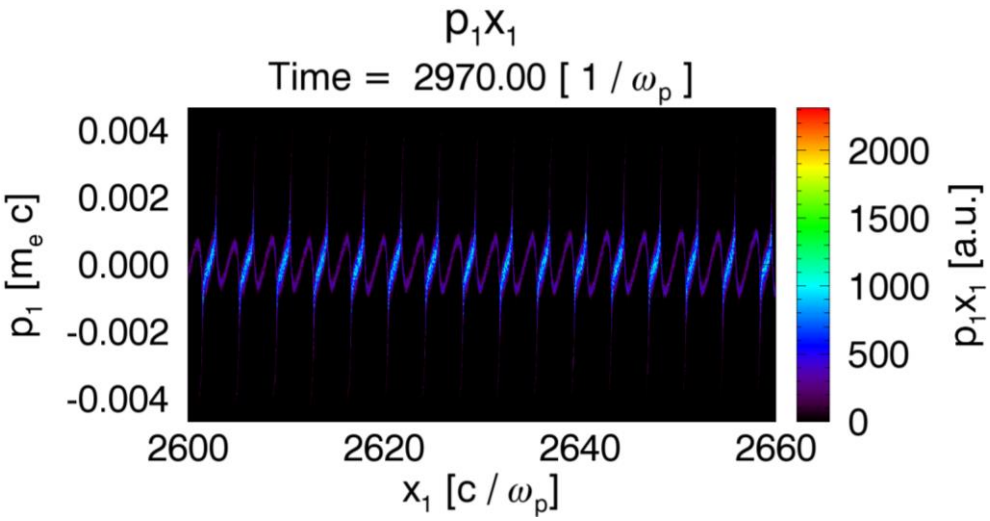

Figure 5.6.3.2b – Peak amplitude of the ion acoustic waves in the unstable configuration

It can be seen from figure 5.6.3.2a that the ion acoustic wave at an earlier time in the simulation is very stable and is of good quality which is commensurate with the pulse profile identified in figure 5.6.3.1a. As the simulation progresses in time it can be seen from figure 5.6.3.2b that the wave exhibits strong signs of wavebreaking and is therefore unstable at this instance in time. The very high amplitude reached by the pulse in figure 5.6.3.1b is therefore attributed to the onset of the saturation of the

energy transfer process by the commencement of the collapse of the ion acoustic wave.

A summary of the simulation parameters for this simulation, labelled as II*, are detailed in table 2. Comparison of the data presented in table 2 with that previously presented in table 1 for simulations II* and II, respectively, shows some notable differences: Namely, the efficiency of the energy transfer process is significantly reduced from simulation II to simulation II*. This drop in efficiency when moving to the unstable regime, associated with simulation II*, is due to the fact that the resultant amplified pulse is also significantly compressed. It has already been demonstrated in section 5.1 of this chapter via equation 5.3.7 that extreme Brillouin compression is found to be an inefficient process. The simulation results presented here further highlight this and the contrast between the processes of Raman and Brillouin scattering as a means of laser beam amplification. The primary difference between Brillouin and Raman scattering mechanisms is seen via the findings by Trines. et al. [Trines. et al. 2011b] who have shown that efficient Raman amplification of laser pulses with a compression ratio of 1000 can be obtained. In the case of Brillouin amplification, however, the results presented throughout this chapter detail that the resultant seed laser pulse after undergoing Brillouin amplification maintains a duration much closer to that of its initial duration and pushing for more extreme compression serves only to drastically reduce the efficiency of the energy transfer process between the pump and seed lasers.

	VIII	IX	II*
ao	0.027	0.00855	0.0855
a1	0.00855	0.0027	0.027
t_{pu} (ps)	7979	23400	1.44
$t_{pr,i}$ (fs)	384	425	200
$t_{pr,f}$ (fs)	43	156	7
Eff. (%)	26	2	30

Table 2 – Summary of simulation results using OSIRIS moving window

5.7 Summary and discussion

In summary, analytical self-similar theory has been used to develop a number of scaling laws for controlling the final probe pulse characteristics and for determining the optimum laser initial conditions to obtain effective laser amplification via stimulated Brillouin scattering. In conjunction with particle-in-cell simulations these scaling laws have been tested and were found to be effective in choosing specific regions of parameter space where efficient energy transfer from pump to seed laser is observed.

Optimal regions of parameter space resulting in maximum efficiencies were identified in addition to extended regions where effective SBS was also exhibited, with reduced efficiencies. The results from the numerical simulations found that efficiencies of up to 57% could be realized with a pump laser intensity of $1x10^{16}Wcm^{-2}$ and a seed laser of $1x10^{15}Wcm^{-2}$. Laser intensities of $1x10^{17}Wcm^{-2}$ and above, however, were found to be ineffective for application to SBS due to the very high levels of parasitic Brillouin backscattering present, which serves to deplete the pump laser of available energy for transfer to the seed laser. Laser intensities between $1x10^{16}Wcm^{-2}$ and $1x10^{14}Wcm^{-2}$ were also found to produce adequate levels of amplification with efficiencies ranging from the highest at 57% down to around 26%, with the efficiency falling with the laser intensity. Although some energy transfer between the pump and seed lasers is exhibited at intensities below $1x10^{14}Wcm^{-2}$, the corresponding efficiencies are found to be very low, around the few per cent level. This is primarily due to the fact that at very low intensities the seed laser takes a significantly longer time to grow than in the high intensity cases and requires to have propagated through a much longer plasma amplifier also. The study of such low intensity regions of parameter space was facilitated by the implementation of a moving window feature into the OSIRIS framework, without which the study of very low intensity regions of parameter space would not have been possible.

Various factors concerning the viability of utilising stimulated Brillouin scattering as an alternative to stimulated Raman scattering for laser beam amplification were also identified from the work contained within this chapter. It was shown through both

the analytical and numerical work performed that extreme Brillouin compression is inefficient, therefore meaning that SBS is most useful in cases where final longer pulse lengths are required. Conversely, SRS produces ultrashort laser pulses as extreme compression for Raman scattering is very efficient. This means that instead of stimulated Brillouin scattering being used as an alternative to stimulated Raman scattering, both processes are complementary and the decision to utilise one process or the other should be determined by the desired output characteristics of the amplified seed pulse.

It can therefore be seen, through the analytical theory and the simulation results presented within this chapter, that efficient amplification of laser beams via stimulated Brillouin scattering in plasma is possible through careful selection of the regime of operation in parameter space. This highlights the importance of the selection of suitable initial conditions for such a scheme and the requirement for self-similar theory and numerical simulations for guiding the design of future experiments.

References

Andreev, A., Riconda, C., Tikhonchuk, V. T. and Weber, S. *Short light pulse amplification and compression by stimulated Brillouin scattering in plasmas in the strong coupling regime.* Physics of Plasmas 13, 053110 (2006)

Forslund, D. W., Kindel, J. M. and Lindman, E. L. *Theory of stimulated scattering processes in laser-irradiated plasmas.* Physics of Fluids 18, 1002 (1975)

Kim, J., Lee, H. J., Suk, H. and Ko, I. S. Characteristics of pulse compression in laser pulse amplification by stimulated Raman backscattering. Physical Review Letters A 314, 464 (2003)

Malkin, V. M., Shvets, G. and Fisch, N. J. *Fast Compression of Laser Beams to Highly Overcritical Powers.* Physical Review Letters 82, 4448 (1999)

Ping, Y., Kirkwood, R. K., Wang, T.-L., Clark, D. S., Wilks, S. C., Meezan, N.,Berger, R. L., Wurtele, J., Fisch, N. J., Malkin, V. M., Valeo, E. J., Martins, S. F., and Joshi, C. *Development of a nanosecond-laser-pumped Raman amplifier for short laser pulses in plasma.* Physics of Plasmas 16, 123113 (2009)

Trines, R. M. G. M., Fiúza, F., Bingham, R., Fonseca, R. A., Silva, L. O., Cairns, R. A. and Norreys, P. A. *Simulations of efficient Raman amplification into the multipetawatt regime.* Nature Physics 7, 87 (2011a)

Trines, R. M. G. M., Fiúza, F., Bingham, R., Fonseca, R. A., Silva, L. O., Cairns, R. A. and Norreys, P. A. *Production of Picosecond, Kilojoule, and Petawatt Laser Pulses via Raman Amplification of Nanosecond Pulses*. Physical Review Letters 107, 105002 (2011b)

Chapter 6
SBS with a single laser frequency

Typically, as stimulated Brillouin scattering produces a frequency shift in the scattered wave spectra, it is necessary for the seed laser to be downshifted by an amount equal to the ion acoustic frequency in order for coupling between the laser beams to be realised. When utilising long beams, which naturally have a very narrow bandwidth, an adjustment to the seed laser is essential for ensuring that the necessary frequency component for scattering is present in the seed for resonance to occur. This creates an additional technical complexity to achieving Brillouin scattering in plasma.

In this chapter however, we report on the feasibility of Brillouin scattering using two beams incident from the same laser, one long pump beam and one short seed beam counter-propagating with respect to one another through a volume of plasma, with no modifications made to the frequency of either pulse. Results from a recent experimental campaign will be presented, conducted by E. Guillaume et al. [Guillaume et al. 2013], and compared with particle-in-cell simulation data of single frequency SBS. These experimental results will also be used to conduct an additional benchmarking exercise for the numerical simulation data presented throughout this thesis.

6.1 Experimental setup

The experiments were conducted on the VULCAN Nd:Glass laser facility at the Rutherford Appleton Laboratory and were constructed as seen in figure 6.1.1.

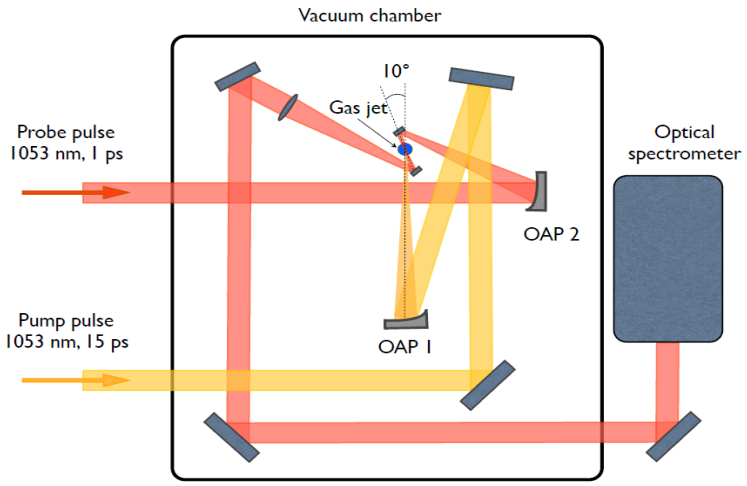

Figure 6.1.1 – Schematic diagram of SBS Experimental set-up

This facility provided two linearly polarized laser pulses of central wavelength 1053nm and bandwidth of 2nm with laser spot sizes on target of 130μm, achieved by reducing the beam diameters to 120mm via pierced plastic plates. Each laser pulse was focused onto the target using f/30 off-axis parabolic mirrors with a focal length of 612mm. The laser-plasma parameters were varied from shot to shot however the parameter ranges were as follows: The pump beam contained between 570mJ and 860mJ of energy with a pulse duration of 15ps giving a pump intensity on target around $3x10^{14}$ Wcm^{-2}; the seed beam contained between 38mJ and 477mJ with a pulse duration of 1ps providing a seed intensity on target between $2.5x10^{14}Wcm^{-2}$ and $3.3x10^{15}Wcm^{-2}$;the pulses were focussed onto the centre of a 5mm long supersonic gas jet target, comprising either argon or deuterium, producing uniform plasmas when ionized - with background electron densities of between $1.7x10^{17}cm^{-3}$ and $1.7x10^{20}cm^{-3}$. The plasma in this case was created by the interaction pulses themselves; therefore no ionization pulse was required to trigger the multi-photon ionization of the gas and collisions between electrons and atoms. The laser pulses were then injected into the target from opposite directions with an angle of 10 degrees between the two counter-propagating beams. The temporal delay between the pump and seed lasers was adjusted such that the two ascending edges of the pulses crossed in the centre of the gas target, maximizing the region of interaction. This geometrical setup resulted in an interaction region of 1.65mm. The light transmitted through the plasma in the direction of propagation of the seed beam was

collected and collimated using a lens of 600mm focal length. The collimated beam was then steered out of the target chamber using silver mirrors and focused onto the entrance slit of an optical spectrometer, equipped with a 150 lines/mm diffraction grating coupled with a 16-bit CCD camera recording the spectra with a 0.1nm resolution.

6.2 Experimental results

The results presented in figures 6.2.1 – 6.2.4 detail the observations from the experimental investigation of SBS in plasma using a single laser frequency. In each of the four cases examined, normalised intensity versus normalised angular frequency has been plotted in relation to the different laser-plasma configurations investigated.

In order to provide a benchmark for the behaviours identified in this study, a reference spectrum for the case where the gas jet is switched off and a single seed laser of intensity $6.1 \times 10^{14} Wcm^{-2}$ was allowed to propagate through the geometry is examined in figure 6.2.1.

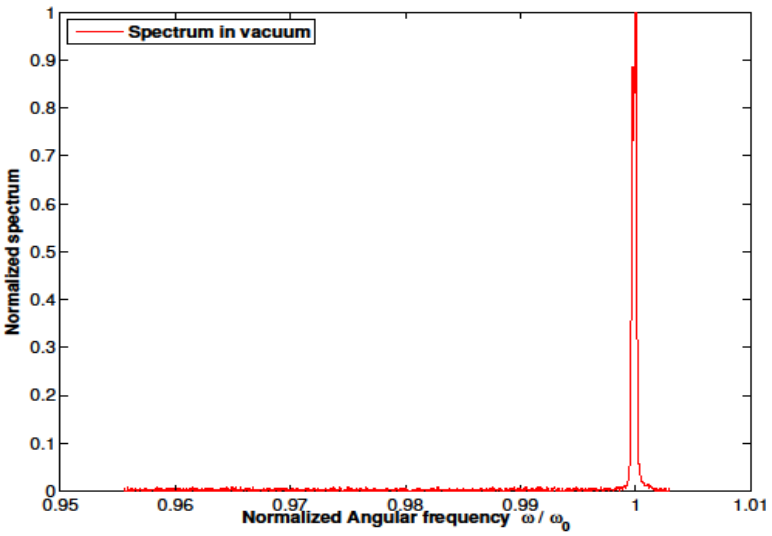

Figure 6.2.1 –Spectrum for a single laser pulse of intensity $6.1 \times 10^{14} Wcm^{-2}$ propagating through the experimental setup in vacuum as a reference for the experimental data results with plasma

It can be seen from figure 6.2.1 that the propagation of a single seed pulse through the system, where the gas jet has not been fired, has resulted in a single peak commensurate with the propagation of the laser frequency in vacuum. There are no signs of any scattering processes, as expected, as the resonance conditions for stimulated Brillouin scattering cannot be satisfied in the absence of plasma. This result therefore provides a useful reference for the scattering processes observed in the spectra for the following three data sets: A, B and C.

Data set A, seen in figure 6.2.2, relates to the propagation of the seed laser, of intensity approximately equal to that in the reference case, through a plasma of density $2 \times 10^{19} cm^{-3}$. It can be seen upon comparison with figure 6.2.1, plotted with a red dotted line, that there are some additional frequency components in the spectra. The main peak in the spectra is seen to have a lower amplitude than that of the vacuum case which is attributed to the fact that the main laser frequency has been depleted due to the presence of scattering processes. In addition to this there is a clearly distinguishable, although very small amplitude, secondary peak, upshifted from the fundamental peak by 2.5nm – which is equivalent to a frequency downshift

of $4x10^{12}$rad/s. As the plasma density in this case is $2.0x10^{19}cm^{-3}$, the plasma frequency is therefore $2.5x10^{14}$rad/s which corresponds to a wavelength separation of 172nm between the Stokes peaks of stimulated Raman scattering and the fundamental peak – since they are separated from ω_0 by the electron plasma frequency. As this value is much larger than the separation observed from the experimental data, the hypothesis that the scattering seen could be due to Raman scattering is excluded. It is therefore more likely that the source of this scattering is Brillouin scattering due to the very small wavenumber shifts between the scattered wave and the fundamental peak. However as there is limited experimental data, confirmation of the exact source of this scattering cannot be determined by the laboratory data alone.

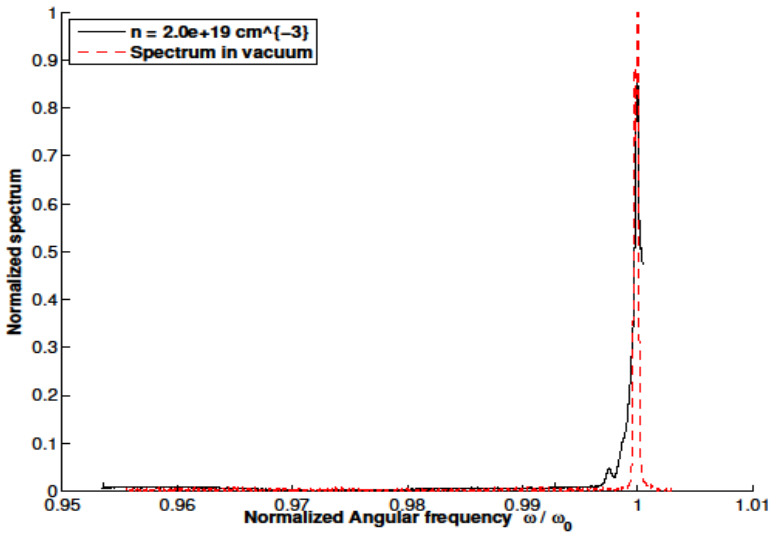

Figure 6.2.2 – Fourier spectra for data set A with a single seed laser, where $n_e = 0.018n_c$

Data set B, seen in figure 6.2.3, details the spectra when both a pump and seed pulse of intensity $5.4x10^{15}Wcm^{-2}$ and $6.2x10^{14}Wcm^{-2}$, respectively, are counter-propagating through a plasma of density $2x10^{19}Wcm^{-2}$, very close to that of figure 6.2.2. It can be seen that there is a much larger proportion of scattering observed in this spectra as compared to figure 6.2.2 and, again, the presence of a secondary peak

is identified occurring very close to the fundamental peak with a wavenumber commensurate with that of the data obtained through the scattering process identified in case A with a single seed laser. In this case however, it can be seen that the relative intensity of the downshifted peak is much higher than for the case where a single seed laser was used, indicating that the scattering mechanism present is enhanced by the introduction of a pump pulse.

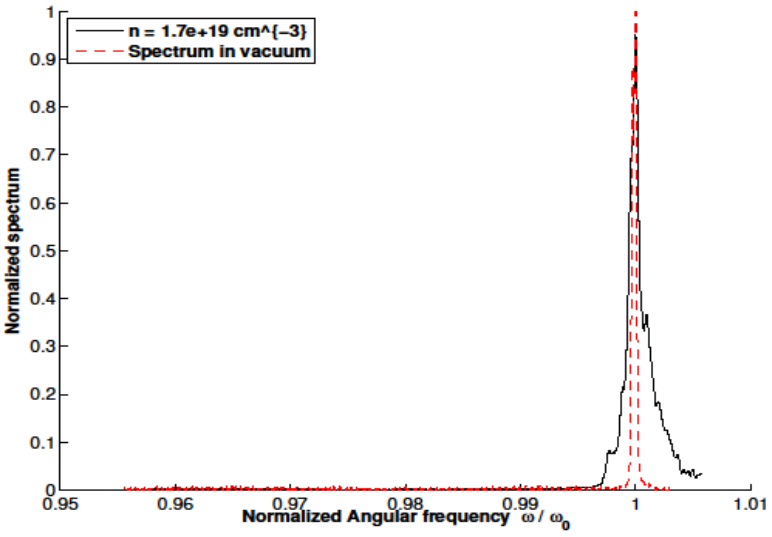

Figure 6.2.3 – Fourier spectra for data set B of pump and seed interaction in plasma where $n_e = 0.015n_c$

The final experimental data set for examination, corresponding to data set C, is viewed in figure 6.2.4 where counter-propagating laser beams of intensities $4.9\text{x}10^{14}\text{Wcm}^{-2}$, for the pump, and $4.9\text{x}10^{14}\text{Wcm}^{-2}$, for the seed laser, traversed through a plasma of density $1.7\text{x}10^{20}\text{cm}^{-3}$. Although the pump pulse is of a slightly lower intensity from that of the experimental setup associated with case B, analysis of this spectral data shows that the highest levels of scattering are exhibited for this case. This is clearly seen from a significant drop in the main beam intensity and the presence of a number of secondary peaks in the spectrum. It can be seen that the first scattered peak has the highest relative intensity seen throughout the entire experimental data set and is attributed to the increase in plasma density, from case B,

by approximately one order of magnitude. The wavenumber of the primary scattered wave in this case is again indicative of a scattered wave resultant from SBS with a small wavenumber shift between the spectral peaks noted. The secondary scattered signal, however, is sufficiently downshifted from the fundamental peak such that its source is unlikely to be from a Brillouin scattering process. Further examination of this parameter set, in addition to analysis of cases A and B, is therefore required in order to determine the origin of the scattering processes observed. As spectral data for the longitudinal electric fields is required for this analysis and there is no such experimental data this study was conducted numerically using PiC simulations.

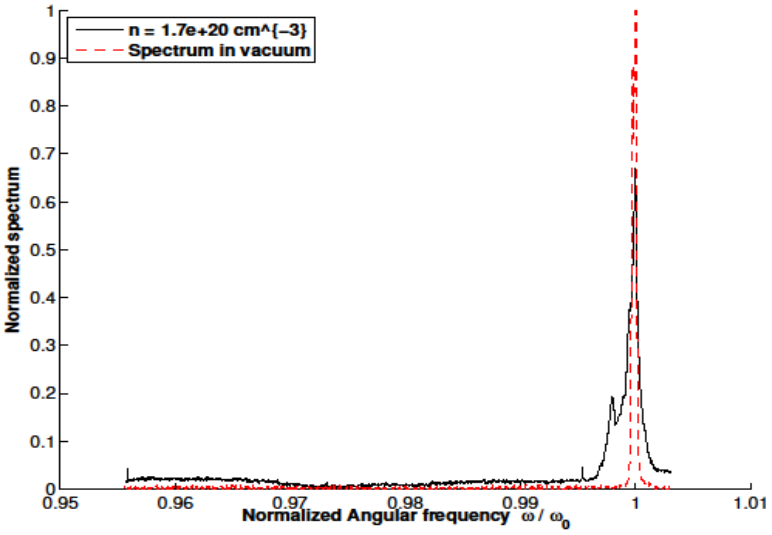

Figure 6.2.4 – Fourier spectra for data set C of pump and seed interaction in plasma where $n_e = 0.15n_c$

6.3 PiC simulation setup

Three sets of simulation results corresponding to each of the three experimental regimes, examined previously, are presented and were set up as follows. In simulation A a single laser of intensity $6x10^{14}Wcm^{-2}$ was injected into an argon plasma of density $0.018n_c$ with a mass ratio for ions to electrons of Zm_i/m_e =14688. The plasma temperature ratio was set such that ZT_e/T_i = 25 where Z = 5 and T_e =

20eV, assuming a neon-like argon with the majority of the outer shell of electrons depleted. For simulation B two counter-propagating pulses were launched into a plasma of density $0.015n_c$, in this case comprising of deuterium, with a mass ratio of ions to electrons where $m_i/m_e = 3672$ with the plasma ion and electron temperatures kept constant at 20eV for the ions and 120eV for the electron species. Laser intensities of $6.2\text{x}10^{14}\text{Wcm}^{-2}$ and $5.4\text{x}10^{14}\text{Wcm}^{-2}$ for the pump and seed, respectively, were used where the seed pulse was launched at the instant the pump laser had traversed the length of the plasma. In the case of simulation C, two counter-propagating beams were used and their intensities were both set to $4.9\text{x}10^{14}\text{Wcm}^{-2}$ and propagated through an argon plasma with a configuration such that $m_i/m_e = 73440$, $ZT_e/T_i = 5$ where $Z = 1$ and $T_e = 5\text{eV}$ and a density of $0.16n_c$. The following parameters are consistent throughout each of the three simulations presented: the pulses propagate through a plasma column of length $1410c/\omega_0$ with the pump pulse traveling from right to left through the simulation box, the pump pulse has a duration of 1.5ps and the seed pulse a duration of 100fs, each of the pulses are from a laser of wavelength $1\mu m$, the time step for integration is $\Delta t = 0.04\omega_p^{-1}$ where ω_p is the plasma electron frequency and the spatial resolution of the simulations is of the order of the Debye length with 100 particles per cell. Due to computational limitations the pulse lengths and plasma column have been scaled down by a factor of ten from that of the parameters used to obtain the experimental results.

6.4 PiC simulation results

The results from the PiC simulations corresponding to the three parameter sets: A, B and C, as examined via the experimental data, are detailed below.

Case A

In figure 6.4.1 the Fourier transform of the transverse electric field is shown. It can be seen that the spectra is closely correlated with that of the experimental spectra (figure 6.2.2), with the small scattered peak very close to the main laser peak, which

corresponds to the laser field in the plasma. From equation 4.3.2.5 the wavenumber of the laser beam propagating through the plasma can be determined and is found to be ~0.99, which is the wavenumber observed in the FFT E_2 spectra seen in figure 6.4.1

The slight shift in the wavenumber spectra observed in the PiC simulations compared with that of the experimental data set as detailed in 6.2.2, and indeed in the two sets of simulation data to follow, is due to the fact that the simulation spectra is normalised to the laser field in vacuum whereas the experimental data set is normalised to the laser field in plasma. However, for case A as the plasma density is so low this shift is very small. It is also noted that the spectra obtained through the PiC simulations is much narrower than the experimental spectra, this will be discussed in greater detail in section 6.5.

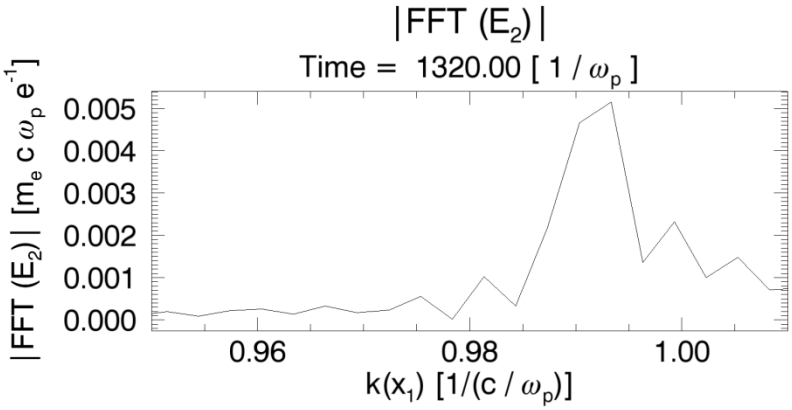

Figure 6.4.1 – Fourier spectra of the transverse electric field for simulation A

The source of the scattering exhibited in the experimental data can be determined via analysis of the Fourier spectra of the longitudinal electric fields in the PiC data for the same data set. This data is displayed in figure 6.4.2.

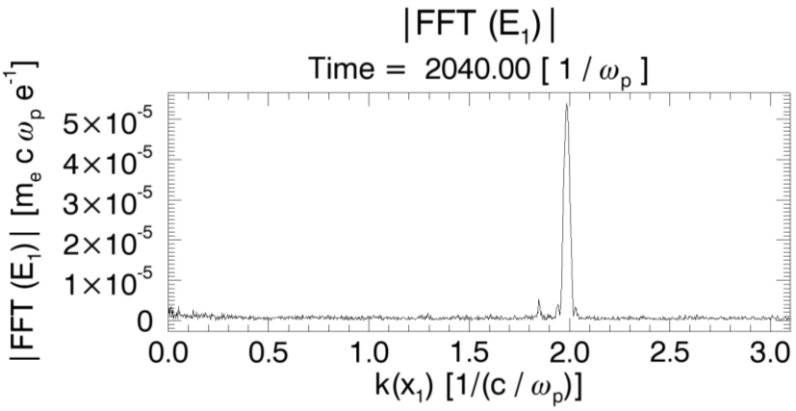

Figure 6.4.2 – Fourier spectra of the longitudinal electric field for simulation A

Observation of the data in figure 6.4.2 shows that a strong signal is detected at a wavenumber of approximately $2\omega_p/c$ which corresponds to the expected ion acoustic wave for Brillouin scattering. This wavenumber is calculated via equation 4.3.2.3 and found to be approximately twice the calculated k_0 value from the Fourier transform of the transverse electric field data above. From this theoretical analysis the ion acoustic wavenumber is therefore expected to be close to $1.98\omega_p/c$ confirming SBS as the observed scattering mechanism. The presence of a second spectral peak is also noted at a wavenumber of 1.85 commensurate with that of Raman back scattering. The presence of SRS is due to the fact that the plasma density in this case is very low, at $0.018n_c$, allowing the simultaneous excitation of both Brillouin and Raman scattering. It is noted, however, that the Raman scattering observed is at a very low level compared to the level of Brillouin scattering obtained, therefore it is initially anticipated that SRS will not be significantly detrimental to the laser amplification process for this parameter set.

Very low levels of SBS are observed at the timestep corresponding to $3000\omega_p^{-1}$ in figure 6.4.3. Initially it can be seen that the pump field is very stable but after an extended simulation time it can be seen that the onset of the scattering processes are beginning to have an effect on the propagation of the laser beam through the plasma. It can therefore be said that stimulated Brillouin scattering can be observed from a single laser frequency propagating through plasma even at densities far below what are considered ideal for SBS where low level Raman scattering is also excited. However, as there are no signs of energy exchange between the pump and seed laser

beams, even after an extended simulation time, it can be concluded that the mode competition between Raman and Brillouin scattering in this case serves to prevent laser amplification via SBS in such low density plasma.

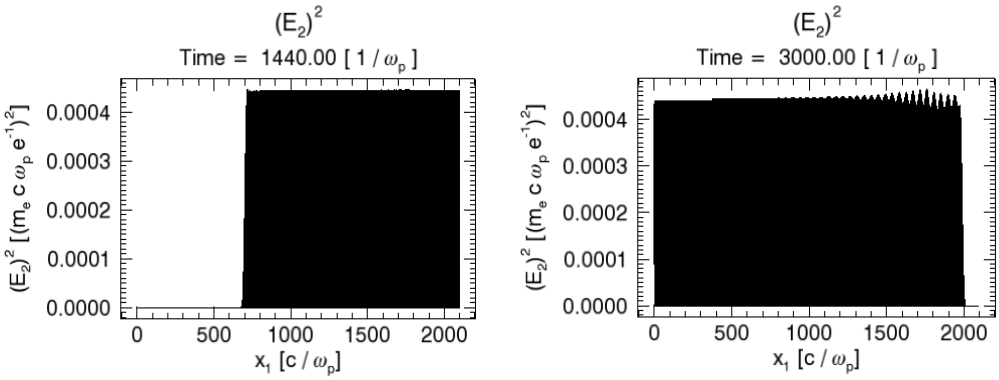

Figure 6.4.3 – Square of the electric field of the seed pulse propagation for simulation A

Case B

The data presented for case B further examines the experimental data set as seen previously in figure 6.2.3 and is used to determine whether SBS is, again, the scattering mechanism which is producing the downshifted low intensity peak in the Fourier spectra of the transverse electric field. For the parameters used in this case, the fundamental laser frequency within the plasma of density $0.015n_c$ should correspond to ~0.99 as calculated from equation 4.3.2.5. This is approximately equal to the fundamental laser wavenumber in case A as the plasma densities are almost identical. It can be seen from figure 6.4.4 that the laser wavenumber spectral peak is commensurate with this theoretical calculation with the spectral peak excited where predicted. It is, again, noted that the spectra produced from the experiments is broader than that indicated from the simulation data.

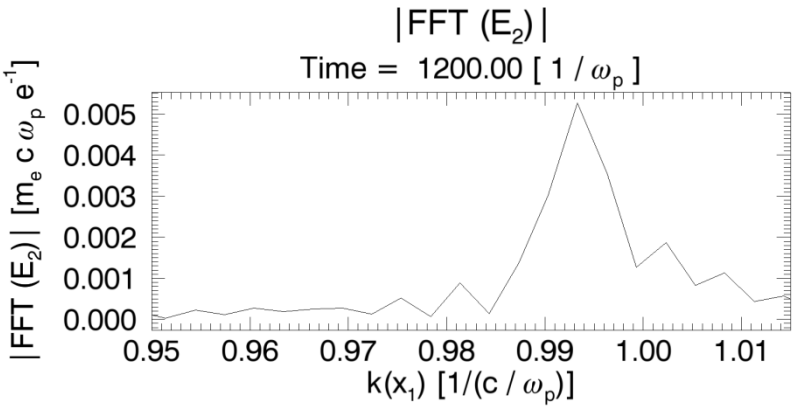

Figure 6.4.4 – Fourier spectra of the transverse electric field for simulation B

The scattering mechanism for this set of data can also be confirmed to be originating from SBS. This is due to the fact that the spectral peak observed in the Fourier spectra of the longitudinal electric field, as seen in figure 6.5.5, is also equal to $2k_0 \approx 1.98\,\omega_p/c$. Thus, indicating that it is an ion acoustic wave that is performing the scattering as seen above in figure 6.4.4, originating from the driven SBS process which grows linearly in time. It is also noted that the amplitude of the ion acoustic wave in this case is equal to the intensity achieved in case A but much earlier in the simulation, indicating that the presence of the second laser beam serves to boost the levels of SBS obtained by driving the scattering process harder. The presence of a second, much lower amplitude, spectral peak is also observed in figure 6.4.5 occurring at a wavenumber of approximately 1.86. This wavenumber excitation is, again, attributed to the presence of Raman backscattering occurring within the simulation further illustrating that SBS and SRS undergo mode competition when low density plasma, in this case equal to $0.015n_c$, is used. As the amplitude of the Brillouin scattered peak is much larger than that of the Raman scattered peak it can be deduced that, although SRS and SBS are both excited for this laser-plasma configuration, stimulated Brillouin scattering is more strongly affected by the addition of a second laser pulse.

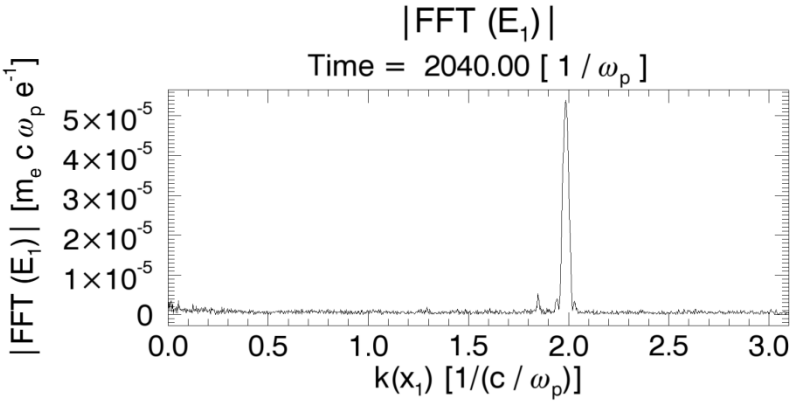

Figure 6.4.5 – Fourier spectra of the longitudinal electric field for simulation B

The effect of SBS on the propagation of the seed pulse through the plasma is also investigated via the intensity plots shown in figure 6.4.6. It can be seen that the seed pulse is injected at $1800\omega_p^{-1}$ after the pump wave has traversed the length of the plasma. The seed laser then propagates from left to right through the pump field and is amplified by a very small amount by the pump. As the interaction length in the simulation is much shorter than in the experiment it is possible that the seed pulse is amplified beyond that which is observed at $2880\omega_p^{-1}$ in figure 6.4.6. Nonetheless, the PiC data demonstrates that for the parameters used in the experimental investigation signs of possible seed pulse amplification in low density plasma are exhibited when two laser beams are introduced, even in the presence of very low levels of Raman scattering.

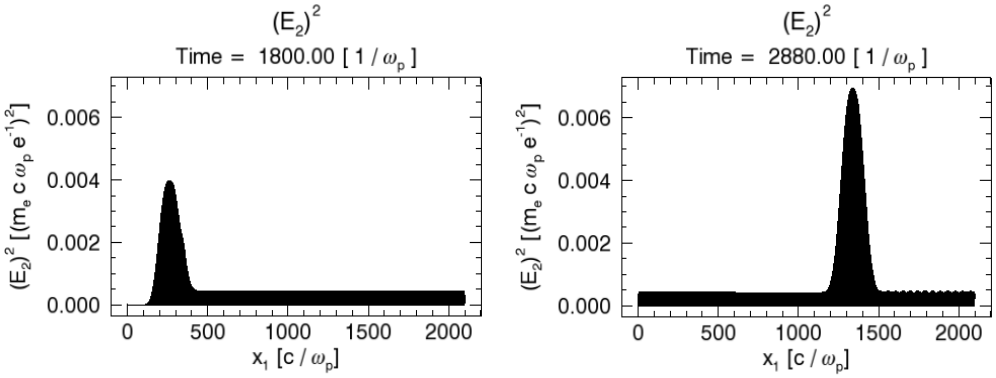

Figure 6.4.6 – Square of the transverse electric field of the seed pulse propagation for simulation B

Case C

The simulation data presented here in case C is identified with the experimental data set presented previously in figure 6.2.4. Theoretical calculation of the fundamental laser frequency within a plasma of $0.16n_c$ is found to be ~0.92 via equation 4.3.2.5. This is corroborated by the data presented in figure 6.4.7 corresponding to the Fourier spectra of the transverse electric field. Again, similarly to the experimental data for this parameter set, the presence of a small amplitude downshifted spectral peak is noted immediately to the left of the spectrum associated with the experimental findings. This case, however, shows the largest discrepancy between the positions of the spectral peaks obtained via the simulation and experimental data respectively. This is due to the fact that the plasma density is much higher than in the previous two parameter sets studied.

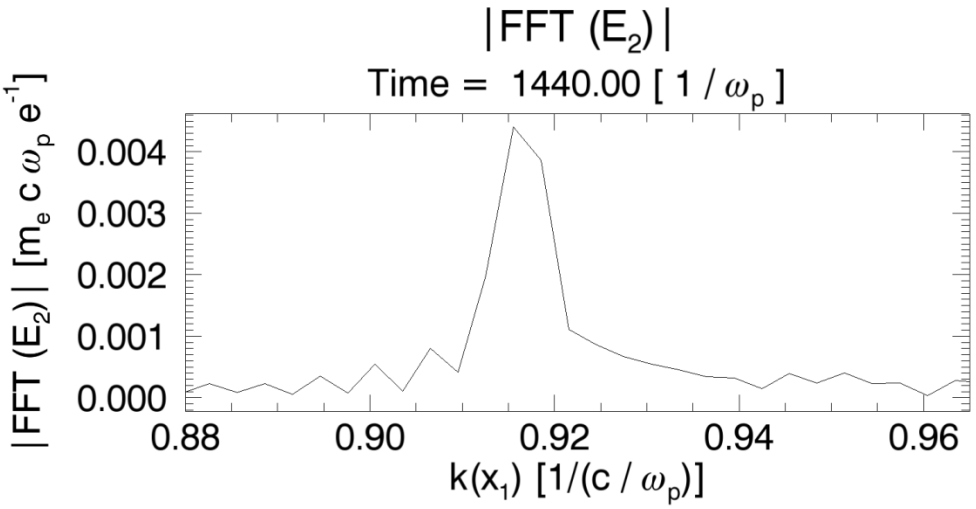

Figure 6.4.7 – Fourier spectra of the longitudinal electric field for simulation C

Analysis of the Fourier spectra of the longitudinal electric field for this data set reveals a number of spectral peaks attributed to the scattering observed in figure 6.4.7. In contrast to cases A and B the predominant mechanism for the laser scattering detected from this data set is not attributed to any Brillouin scattering process. This is seen upon analysis of figure 6.4.6 as the spectral peak observed which is commensurate with that of an ion acoustic wave (labelled 3), having

wavenumber of approximately $2k_0$, is only very weakly excited. There are, however, two other spectral peaks observed at wavenumbers corresponding to approximately $\frac{1}{2}\omega_0$ (labelled 1) and $\frac{3}{2}\omega_0$ (labelled 2) which are analogous to wavenumber excitations resulting from instabilities such as two-plasmon decay [Turner et al. 1984] [Meyer and Zhu 1993] and Raman scattering [Forslund, Kindel and Lindman 1975], one of which excitations having an amplitude much in excess of that seen for the ion acoustic wave from the SBS process. As the two-plasmon decay instability, which is characterised by the decay of an incident laser beam into two Langmuir waves, requires two-dimensions for its behaviour to be adequately described it is more likely that the scattering exhibited is as the result of the excitation of a Raman-like instability. Upon calculation of the expected wavenumbers for Raman scattering with a plasma configuration as detailed in this simulation it can be shown that the wavenumber excitations labelled 1 and 2 in figure 6.4.6 are attributed to Raman forward scattering, with an associated wavenumber of approximately 0.47, and Raman backscattering, with a wavenumber of 1.42, respectively. Comparison with the results obtained from case C with that of cases A and B details a regime change from a parameter set at very low density where higher levels of SBS than SRS are detected to a case where Raman scattering, in particular Raman backscattering, is clearly dominant, confirmed via the much higher detected levels of SRS than SBS. The presence of such phenomena and subsequent mode competition between Brillouin scattering, Raman scattering and the two-plasmon decay instability are typical for plasmas with densities just below the quarter critical level as SBS is dominated by the competition between the Raman and two-plasmon decay instabilities as the threshold for these instabilities due to inhomogeneity is relatively low near the quarter critical density. This therefore limits the exploitation of SBS as a means of laser amplification within low density plasmas, particularly for those below the $0.3n_c$ level. This fact is the primary reason why the majority of the numerical simulations presented throughout this thesis were conducted at plasma densities of $0.3n_c$.

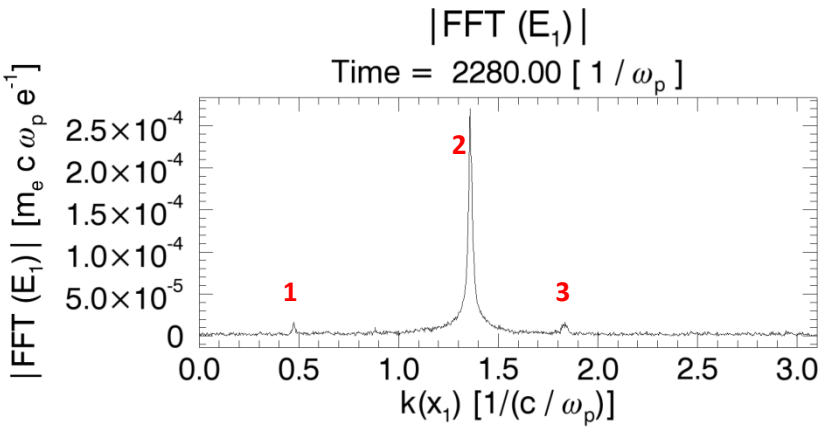

Figure 6.4.6 – Intensity plot of the seed pulse propagation for simulation C

6.5 Benchmarking PiC data with experimental observations

Upon comparison of the spectra illustrating the data from the laboratory experiments, presented in figures 6.2.2, 6.2.3 and 6.2.4, to the corresponding results obtained via the particle-in-cell simulations, seen in figures 6.4.1, 6.4.4 and 6.4.7, it can be seen that the results for all three cases are closely correlated. The small discrepancies in the wavenumbers presented in the numerical simulation data, compared to that presented in the experimental findings, are attributed to the use of different normalisation factors for the data sets; whereas the experimental data utilises the laser frequency in vacuum whereas the experimental data uses the laser frequency in plasma as a normalisation factor.

In each of the three cases examined numerically, however, it can be seen that the Fourier spectra obtained is slightly broader than that of the experimental results. This slight variation in the spectra is attributed to the fact that the simulations have no transverse dimensions as they were performed in 1D, hence putting numerical constraints on the solutions obtained as there can be no transverse variation of the laser intensity. Therefore the amplitude of any plasma wave driven by the laser will be overestimated which leads to an overestimation of spectral drifts and of the temperature recorded also. This is a common compromise made when studying such complex laser-plasma interactions due to the fact that performing parameter scan

calculations running 2D or full 3D versions of simulation code with large experimental dimensions is impractical as the run time would comprise very many hours on a very large number of CPU's, very many times! Taking this into account, however, it is noted that the same overall behaviours captured via the 1D numerical simulations are commensurate with that observed from each of the experimental results. This further highlights the accuracy of the calculations performed by OSIRIS for the diagnosis of scattering instabilities within underdense plasmas, without the need for additional degrees of freedom out with that computed in 1D calculations.

6.6 Optimised SBS with a single laser frequency

The effect of using a single laser frequency for a parameter set where efficient stimulated Brillouin scattering and subsequent amplification of a seed pulse is known to occur was investigated. Numerical simulations constructed as in section 6.3 were used to study this effect where the pump laser had an intensity of $1x10^{16}Wcm^{-2}$ and a duration of 0.75ps, the seed laser had an intensity of $1x10^{15}Wcm^{-2}$ and a duration of 100fs and the plasma parameters were $ZT_e/T_i = 50$ for a hydrogen plasma.

Figure 6.6.1 and 6.6.2 detail the laser intensities obtained when a seed frequency downshift has been performed and the case where a single laser frequency has been used for the pump and seed pulses, respectively.

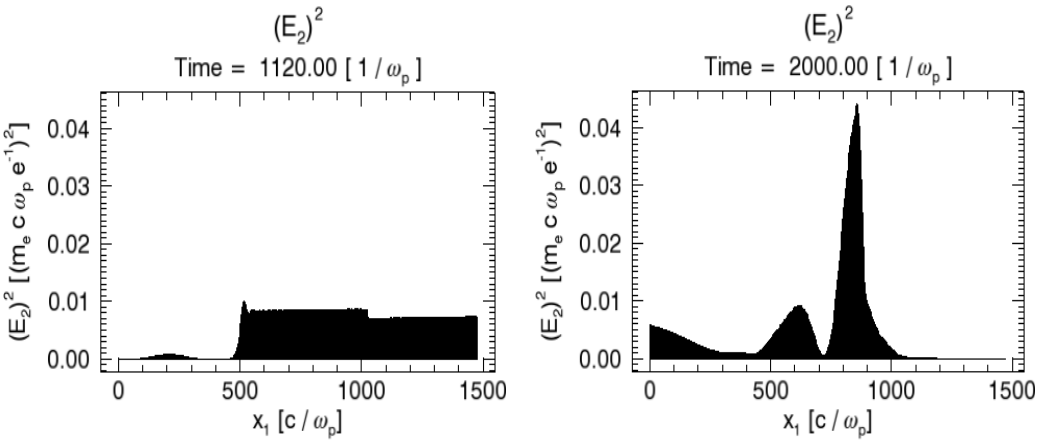

Figure 6.6.1 – Intensity spectra when a seed frequency downshift has been performed

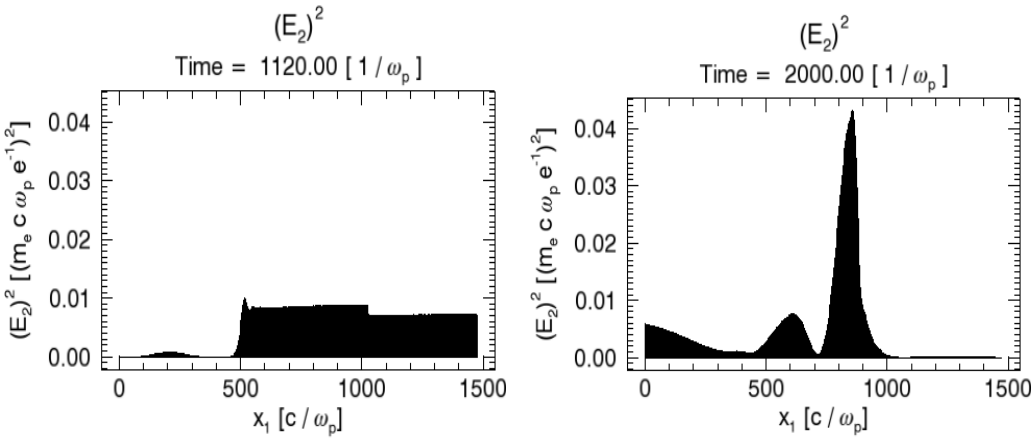

Figure 6.6.2 – Intensity spectra when a single laser frequency is used

Through examination of figures 6.6.1 and 6.6.2 it is seen that for the case where a single laser frequency is used the resultant seed intensity reaches an amplitude consistent with that obtained when the seed laser has been downshifted by an amount equal to the ion acoustic frequency. It can therefore be verified that efficient seed pulse amplification can be observed using the natural bandwidth of a sufficiently short pulse laser beam. This negates the requirement for a downshift in the seed laser frequency, typically by an amount equal to the ion acoustic frequency, to be performed prior to the pump/seed interaction within the plasma.

6.7 Summary and discussion

In summary, experimental observations of scattering mechanisms in plasmas using two beams at the same wavelength have been used to demonstrate that SBS can be achieved with a single frequency laser system. This is the case providing that a sufficiently short duration seed beam is used, such that its natural bandwidth contains the necessary frequency component for scattering to occur. In addition to this it has also been shown that the resultant amplified pulse closely resembles that from a scheme where a frequency downshift in the seed beam has been performed, concluding that, again only for short beams, there are no benefits to frequency downshifting. It is important to note, however, that if a long seed beam is required,

as they naturally have a narrow bandwidth, a frequency downshift is necessary to observe SBS.

Upon comparison of the processes of stimulated Brillouin scattering to stimulated Raman scattering it is clear that there are significant advantages to utilising SBS as opposed to SRS for laser beam amplification. This is due to the fact that it is mandatory to perform a seed frequency downshift to achieve amplification via Raman scattering as the scattered frequency is separated from the laser frequency by an amount equal to the plasma frequency, which is typically much larger than that of an ion acoustic wave. Therefore an extremely short seed pulse would be required in order to ensure the laser bandwidth contained the necessary scattering frequency for Raman scattering to be excited. Consequently, this adjustment to the seed frequency introduces an additional technical complexity to achieving amplified laser pulses in plasma via SRS.

Evaluation of the experimental results in this chapter highlights the plasma density considerations for SBS excitation. It was observed that for very low plasma densities as seen in cases A and B that SBS is detected, although upon verification of these results with the numerical simulation data it was seen that this scattering was very low level and did not result in significant seed laser amplification. When the plasma density was raised by approximately an order of magnitude such that it is much closer to the cut-off density for Raman scattering ($0.25n_c$) it was seen, from the numerical results in case C that other scattering processes such as two-photon decay and Raman scattering processes dominated the spectral behaviour observed. In the final case examined in section 6.6 seed laser amplification was observed for the case where both pump and seed lasers originated from the same source for a parameter set where amplification via SBS was already known to occur. It can therefore be concluded from this set of data that single frequency SBS, and indeed SBS with frequency downshifted beams, can most effectively be implemented for plasmas of density above the quarter critical level, thus preventing mode competition from Raman scattering processes.

Overall, from detailed analysis of both the experimental and numerical results obtained within this chapter, very good correlation was shown between both data sets

with the spectral behaviour seen in the experimental data accurately reproduced in the numerical output. Slight broadening of the spectra associated with the numerical results was observed, however, which is attributed to the simulation being conducted in 1D and having strict numerical constraints on solutions obtained. It can therefore be deduced that extension of the numerical work to 2 or 3 dimensions is likely to prevent this spectral augmentation from occurring.

The work contained within this chapter therefore provides a useful benchmarking exercise for SBS using the OSIRIS particle-in-cell code in addition to the theoretical benchmarking conducted previously in chapter 5 of this thesis. This provides additional evidence for the reliability of the numerical simulation results presented in chapters 4, 5 and 6.

References

Forslund, D. W., Kindel, J. M. and Lindman, E. L. *Theory of stimulated scattering processes in laser-irradiated plasmas.* Physics of Fluids 18, 1002 (1975)

Guillaume, E., Humphrey, K. A., Trines, R. M. G. M., Heathcote, R., Galimberti, M., Bingham, R., Amano, Y., Doria, D., Habara, H., Nakamura, H., Hicks, G., Higson, E., Kar, S., Najmudin, Z., Sarri, G., Borghesi, M., Skramic, M., Tanaka, K. A., Swain, J., Tang, K., Weston, J., Zak, P. and Norreys, P. A. *Efficient laser pulse amplification by stimulated Brillouin scattering.* Submitted: Nature Photonics (2013)

Meyer, J. and Zhu, Y. *Measurement of Two Plasmon Decay Instability Development in k Space of a Laser Produced Plasma and Its Relation to 2 -Harmonic Generation.* Physical Review Letters 71, 2915 (1993)

Turner, R. E., Phillion, D. W., Lasinski, B. F. and Campbell, E. M. *Half- and three-halves harmonic measurements from laser-produced plasmas.* Physics of Fluids **27**, 511 (1984)

Chapter 7

Conclusions and Future Work

7.1 Overview

The aim of this research project was to support the understanding and development of stimulated Brillouin scattering as an effective means of laser pulse amplification to ultrahigh intensities and develop this scheme in order to become a viable alternative to current CPA techniques utilising solid state technology. The primary objectives of this study were to identify a parameter regime under which this method of laser beam amplification can be effectively performed and to determine a number of scalability factors for the optimisation of the energy transfer process between pump and seed beams.

A number of techniques were employed to study the energy transfer process via SBS in plasma. These methods included an analytical model based on the self-similar theory of Brillouin scattering, numerical simulations using the OSIRIS particle-in-cell code with new integrated moving window feature and experimental data analysis from a recent experimental campaign on the Vulcan Nd:Glass laser facility at the Rutherford Appleton Laboratory. Concluding remarks based on the results presented within chapter 4, 5 and 6 are presented here in addition to the future outlook for this research program.

7.2 Conclusions

The results presented within this thesis provide evidence for significant progress towards the realisation of utilising stimulated Brillouin scattering as an amplification mechanism of laser beams in plasma. This is seen with the combination of the numerical, analytical and experimental data results presented in chapters 4, 5 and 6.

The foundations of this research program were presented in chapter 4 where the energy transfer process between counter-propagating seed and pump lasers was investigated via collisionless and collisional particle-in-cell simulations. From these simulations, the first of such collisional simulations of SBS, it was noted that the inclusion of collisional processes enables a more efficient energy transfer between beams and offers a significant decrease in the volume of seed pre-pulse present. This is of particular importance to future experimental studies and the eventual implementation of SBS for laser beam amplification as laser pre-pulse can significantly alter or even destroy the laser target before interaction with the main beam. In this chapter the effect of plasma ion and electron temperature on SBS was also assessed and it was found that Brillouin scattering can be completely damped by careful selection of both of these parameters. This result is particularly relevant to applications where the presence of Brillouin scattering is undesirable, such as in laser fusion devices.

The results in chapter 5 built upon the knowledge base assimilated in chapter 4 to develop and test scaling laws for optimisation of SBS in plasma via both analytical theory and particle-in-cell simulations. Formulary governing the optimum probe duration was developed and numerical simulations confirmed the importance of choosing the correct initial seed laser length for efficient amplification to be observed. It was also deduced that longer probes are favoured and longer initial probes are needed for efficient amplification via Brillouin scattering compared to that of Raman scattering and that extreme compression of the laser beams is not very efficient for Brillouin scattering. This result is of particular importance for applications requiring a longer duration final seed pulse and shows that Brillouin scattering can be a useful tool in scenarios where Raman scattering is not particularly

effective. Finally, the applicability of stimulated Brillouin scattering to a range of laser-plasma parameters was identified. It was found that for laser intensities of $1x10^{17}Wcm^{-2}$ and above the pump laser is significantly unstable rendering such high intensity beams unusable. The most efficient amplification was observed for pump and seed laser intensities between $1x10^{16}Wcm^{-2}$ and $1x10^{15}Wcm^{-2}$, respectively, and the application of SBS for amplification of low intensity beams was also noted, however the efficiency of such configurations was found to be significantly reduced in comparison to the high intensity cases.

Finally, chapter 6 utilised experimental data and particle-in-cell simulations to assess the suitability of utilising SBS with a single laser frequency. In each of the cases examined, in both the experimental and numerical data sets, the presence of Brillouin scattering was detected confirming that a downshift in the seed laser frequency is not required, provided that a suitably short laser pulse is used. This is of particular interest to the eventual implementation of Brillouin amplification techniques as performing a frequency downshift in the seed laser beam adds an additional technical complexity to the experimental infrastructure. In addition to this the observation of significant levels of Brillouin scattering in regions of parameter space at densities below quarter critical, where low levels of Raman scattering are present, was also noted. This is a significant result as this indicates that Brillouin scattering could potentially be used to achieve long pulses in a regime most commonly attributed to achieving ultra-short pulses via stimulated Raman scattering.

In conclusion, the reliability of the results from the numerical simulations collected and presented throughout this thesis is ensured by the very high level of corroboration by both the analytical and experimental studies also performed. In addition to this the benchmarking exercises performed in conjunction with the existing literature lead to a high confidence in the reliability of the results presented. It can therefore be said that the aims of this research program have been met and a solid body of work upon which to construct multi-dimensional simulations and design future experimental campaigns of laser beam amplification via stimulated Brillouin scattering in plasma has been assimilated.

7.3 Future work

Following directly from the results presented within this thesis there exists a number of potential avenues of interest for continuation of this work. The most immediate requirement is the incorporation of multi-dimensions into the OSIRIS numerical simulations. This would allow an investigation to be conducted on the effect of transverse degrees of freedom and the role of competing laser-plasma instabilities on the efficiency of the energy transfer between the pump and seed laser beams via stimulated Brillouin scattering in plasma. This study would also aid the design of future experimental campaigns by providing a more realistic laser-plasma configuration upon which to benchmark experimental data.

A similar study was conducted for Raman amplification by Trines et al. [Trines et al. 2011] which found that an initially wide parameter band for effective Raman amplification was narrowed by the inclusion of transverse effects by the extension from 1D to 2D and 3D particle-in-cell simulations. This was attributed to the detrimental effects of competing instabilities, such as laser beam filamentation and the modulational instability, resulting in a reduction in laser beam viability for efficient energy transfer from pump to seed pulse for laser-plasma parameters occurring within a specific range. It was also shown, however, that a narrow parameter band exists within which SRS is highly efficient, providing the laser plasma parameters are carefully chosen to mitigate the effect of deleterious laser-plasma instabilities, therefore demonstrating the viability of SRS as an alternative to more conventional amplification schemes such as chirped pulse amplification.

As the current OSIRIS SBS simulations only allow wave propagation in the longitudinal direction it is anticipated that the integrity of the pump and seed laser beams will be affected by the introduction of additional degrees of freedom. However, as the 1D SBS results look even more promising than that of the 1D SRS simulations, due to the fact that much higher laser intensities and longer pulse durations can be utilised, it is anticipated that a highly efficient regime of operation in 2D and 3D, similar to that found for stimulated Raman scattering, will also be realised.

Appendix – Publication record

As a result of the research undertaken throughout this PhD research program, the author has contributed work to five scientific papers:

i) “Effect of collisions on amplification of laser beams by Brillouin scattering in plasmas”, published by Physics of Plasmas.

ii) “Demonstration of laser pulse amplification by stimulated Brillouin scattering”, submitted to High Power Laser Science and Engineering.

iii) "The role of collisions on mode competition between the two-stream and Weibel instabilities", published by Journal of Plasma Physics.

iv) “A robust plasma-based laser amplifier via stimulated Brillouin scattering”, submitted to Physical Review Letters.

v) "Boosting the performance of Brillouin amplification at sub-quarter-critical densities via reduction of parasitic Raman scattering”, draft letter in progress.

Copies of these papers are included in this appendix for reference.